이학박사학위논문

$\sqrt{s}=510$ GeV 종편극 양성자 충돌에서 PHENIX 중앙 신속도 검출기를 이용한 π^0 생성의 이중 스핀 비대칭성 측정

Double Helicity Asymmetry in π^0 Production in Polarized Proton-Proton Collisions at $\sqrt{s}=510$ GeV with PHENIX Mid-Rapidity Spectrometer

2016년 2월

서울대학교 대학원

물리·천문학부

윤인석

$\sqrt{s} = 510$ GeV 종편극 양성자 충돌에서 PHENIX 중앙 신속도 검출기를 이용한 π^0 생성의 이중 스핀 비대칭성 측정

Double Helicity Asymmetry in π^0 Production in Polarized Proton-Proton Collisions at $\sqrt{s} = 510$ GeV with PHENIX Mid-Rapidity Spectrometer

지도교수 최선호

이 논문을 이학박사 학위논문으로 제출함

2016년 1월

서울대학교 대학원

물리·천문학부

윤인석

윤인석의 박사 학위논문을 인준함

2016년 2월

위 원 장	양 운 기	(인)
부위원장	최 선 호	(인)
위 원	Tanida Kiyoshi	(인)
위 원	김 형 도	(인)
위 원	방 형 찬	(인)

Double Helicity Asymmetry in π^0 Production in Polarized Proton-Proton Collisions at $\sqrt{s} = 510$ GeV with PHENIX Mid-Rapidity Spectrometer

Dissertation Advisor Tanida Kiyoshi

A Dissertation Presented

by

Inseok Yoon

to

The Graduate School

of the Requirement for the Degree of

Doctor of Philosophy

in

Physics

Seoul National University

Jan. 2015

We, the Dissertation committee for the above candidate for the Doctor of Philosophy degree, hereby recommend acceptance of the dissertation.

Feb. 2015

Chairperson	Unki	Yang	(signature)
Vice-chairperson	Seonho	Choi	(signature) Seonh
Commitee member	Tanida	Kiyoshi	(signature)
Commitee member	Hyungdo	Kim	(signature)
Commitee member	Hyoungchan	Bhang	(signature)

Abstract

Double Helicity Asymmetry in π^0 Production in Polarized Proton-Proton Collisions at $\sqrt{s} = 510$ GeV with PHENIX Mid-Rapidity Spectrometer

Inseok Yoon
Department of Physics & Astronomy
The Graduate School
Seoul National University

PHENIX measurement of longitudinally double helicity asymmetry (A_{LL}) in inclusive π^0 production at mid-rapidity from $p+p$ collsions at $\sqrt{s} = 510$ GeV from the 2012/2013 RHIC runs is presented. Since the EMC experiment revealed that spin constribution of quarks is surprisingly small, many experimental and theoeretical endeavers have been carried out to understand proton spin structure. The spin contribution of gluon (ΔG) might explain the missing part of the proton spin and measuring ΔG is the ultimate goal of the dissertation. To measure ΔG, accessing the helicity gluon distribution ($\Delta g(x, Q^2)$) is necessary. The longitudinal polarized $p+p$ collsions and A_{LL} measurementss are best tool for it. A_{LL} measurements of π^0 ($A_{LL}^{\pi^0}$) at $\sqrt{s} = 62.4$ and 200 GeV and A_{LL} of jet at $\sqrt{s} = 200$ GeV constrain $\Delta g(x, Q^2)$ significantly. As a result, positive polarization of gluon is discovered within sensed momemtum fraction (x) range, $0.05 \leq x \leq 0.2$. However large uncertainty remains outside of the x region, especially lower x region. Thus expanding experimental sensitivity to lower x region is a crucial step to understand the $\Delta g(x, Q^2)$ and the spin structure. To access the lower x region, new measurement of $A_{LL}^{\pi^0}$ at higher $\sqrt{s} = 510$ GeV is carried out and presented in the disseration. The new measurement covers x region, $0.01 \leq x \leq 0.1$. The measurement is superior to the previous measurements

from the point of not only the unique covered x range but also statistical precision. The sophisticated luminosity corrections are also presented in the dissertation to reduce the effects of the multiple collisions in single bunch crossing and the vertex$_z$ resolution of detectors. As a result, the world first positive asymmetry in hadron production is measured. The perturbative Quantum Chromodynamics theoretical predition which including the previous measurements is in excellent agreement with the presented $A_{LL}^{\pi^0}$. With the positive asymmetry and unique x coverage, the presented $A_{LL}^{\pi^0}$ will contribute to constrain the uncertainty of $\Delta g(x, Q^2)$ significantly.

Keywords : proton spin, gluon, A_{LL} of π^0, PHENIX

Student Number : 2011-20412

Contents

List of Figures

List of Tables

Chapter 1

Introduction

1.1 Proton Structure and Parton Model

Since the measurement of proton's magnetic moment gives the first hint that proton is not a point-like Dirac particle, the substructure of proton has been explored intensively. Many experimental endeavors such as deep inelastic scattering (DIS) and semi-inclusive DIS (SIDIS) have been carried out. Meanwhile, many theoretical exertions have led the formulation of quantum chromodynamics (QCD) and quarks-gluon model. To explain the DIS results, the parton model is proposed. In the parton model, the proton is composed of point-like Dirac particles called partons. The partons was recognized as guarks and gluon in soon. In the model, the proton is in a frame where it has infinity momentum which is valid at high energy. Each parton carries a fraction (x) of the parent proton's momentum and energy.

1.1.1 Parton Distribution Function

The probability distribution called parton distribution function (PDF, $f(x,Q^2)$) describes the probability of finding a parton with x at resolution scale (Q^2). The PDFs contain the crucial information of proton structure.

With uud valence quark model, the following constraints on PDFs are required.

$$\begin{aligned}
&\int_0^1 dx\{u(x,Q^2)-\bar{u}(x,Q^2)\} = \int_0^1 dx u_v(x,Q^2) = 2 \\
&\int_0^1 dx\{d(x,Q^2)-\bar{d}(x,Q^2)\} = \int_0^1 dx d_v(x,Q^2) = 1 \\
&\int_0^1 dx\{q(x,Q^2)-\bar{q}(x,Q^2)\} = \int_0^1 dx q_v(x,Q^2) = 0 \text{ for } q = c,s,t,b \text{ or } g
\end{aligned} \tag{1.1}$$

where u, d, c, s, t, b and g is up, down, charm, strange, top, bottom and gluon distribution function, respectively. Subscript v mean valence distribution.

Evolution of PDF

The dependence of PDFs on Q^2 is explained as the followings. As Q^2 becomes larger, the resolution becomes better. Single parton becomes seen as parton cloud of emitted gluon and pair created $q\bar{q}$ as the resolution becomes better. The dependence of PDFs on Q^2 is described by QCD evolution function, called DGLAP evolution function. Eq. 1.2 is the evolution function.

$$\begin{aligned}\frac{dq_i(x,Q^2)}{dlogQ^2} &= \frac{\alpha_s}{2\pi}\int_x^1 \frac{dy}{y}\Big(q_i(y,Q^2)P_{qq}(\frac{x}{y}) + g(y,Q^2)P_{qg}(\frac{x}{y})\Big) \\ \frac{dg(x,Q^2)}{dlogQ^2} &= \frac{\alpha_s}{2\pi}\int_x^1 \frac{dy}{y}\Big(\sum_i q_i(y,Q^2)P_{gq}(\frac{x}{y}) + g(y,Q^2)P_{gg}(\frac{x}{y})\Big)\end{aligned} \tag{1.2}$$

where x is momentum fraction of resulting parton by $q\bar{q}$ pair creation or gluon emission and y is momemtum fraction of parent parton ($y > x$) and P_{ab} is the probability that parton a is created by parton b called spliting function.

1.1.2 Fragmentation Function

If final state hadrons are considered as in SIDIS, the probability functions which govern the other soft processes are needed and called fragmentation function (FF, $D_q^h(z,Q^2)$). FF describes the probability that quarks materialize into hadron with energy fraction z of hadrons energy to quarks energy.

Because the sum of the energies of all hadrons is the energy of the parent quark,

$$\sum_h \int_0^1 dzzD_q^h(z,Q^2) = 1 \tag{1.3}$$

is hold. The other constrain on FF is hold.

$$\sum_q \int_{z_{min}}^1 dz\{D_q^h(z,Q^2) + D_{\bar{q}}^h(z,Q^2)\} = n_h \tag{1.4}$$

where z_{min} is threshold energy fraction for producing a hadron and n_h is average multiplicity of hadron.

1.1.3 Factorization

The parton model describes the cross section as the convolution of the soft parts such as PDFs and FFs and the hard elastic scatterings which are calculatable with perturbative QCD (pQCD). The scheme is called factorization.

DIS cross section (σ_{lP}^{DIS}), for example, can be written as convolution of PDFs and the elastic scattering cross sections ($\hat{\sigma}^{el}_{lf}$) of a lepton off the parton.

$$\sigma^{DIS}_{lP} = \sum_{f=q,\bar{q},g} \int_0^1 dx f(x,Q^2) \hat{\sigma}^{lf}_{elastic}(xP,q) \tag{1.5}$$

The summation should be over all partons that interacting with virtual photon from probing lepton. The PDFs should be obtained by experiments because those are in soft region. However the elastic scattering cross section can be obtained by pQCD calculation if high momentum transfer is guaranteed and QCD coupling constant (α_s) becomes small enough to be perturbative.

SIDIS cross section (σ^{SIDIS}_{lP}), for another example, can be written as convolution of PDFs, the elastic scattering cross sections of a lepton off the parton then quark c emerged, and FFs.

$$\sigma^{SIDIS}_{lP} = \sum_{f=q,\bar{q},g} \int_0^1 dx \int_0^1 dz f(x,Q^2) \hat{\sigma}^{lf\to cX}_{elastic}(xP,q) D^h_c(z,Q^2) \tag{1.6}$$

Like DIS, the PDFs should be obtained by experiments and elastic scattering cross sections can be obtained by pQCD calculation. Because fragmentations are soft processes, FFs should be obtained by experiments.

By the factorization, measured σ^{DIS}_{lN} can be interpreted as PDFs and the structure of nucleon is revealed.

1.1.4 Universality

Although PDFs and FFs are obtained by many experiments, those should be process independent, i.e., universal to describe true structure of proton. If the universality is not assured, the measured proton structure depends on the process and is not applicable to other processes. Although the universality is assumption, experimental data support the universality because PDFs and FFs obtained by different processes are known to be consistent.

1.1.5 Current Knowledge of Proton Structure

With DIS and SIDIS results and theoretical backgounds discussed above, PDFs have been measuring. Fig. 1.1 shows proton structure fuction, $F_2^P(x,Q^2)$ and Fig. 1.2 shows MSTW 2008 NLO PDFs at $Q^2 = 10$ GeV^2 and $Q^2 = 10^4$ GeV^2. We can see coverage of experimental data is large and PDFs are reasonablly well constrained.

Properties of proton should be explained by the sum of PDFs. Electric charge of proton is easiest subject. With Eq. 1.1 from uud valence quark model, proton charge is

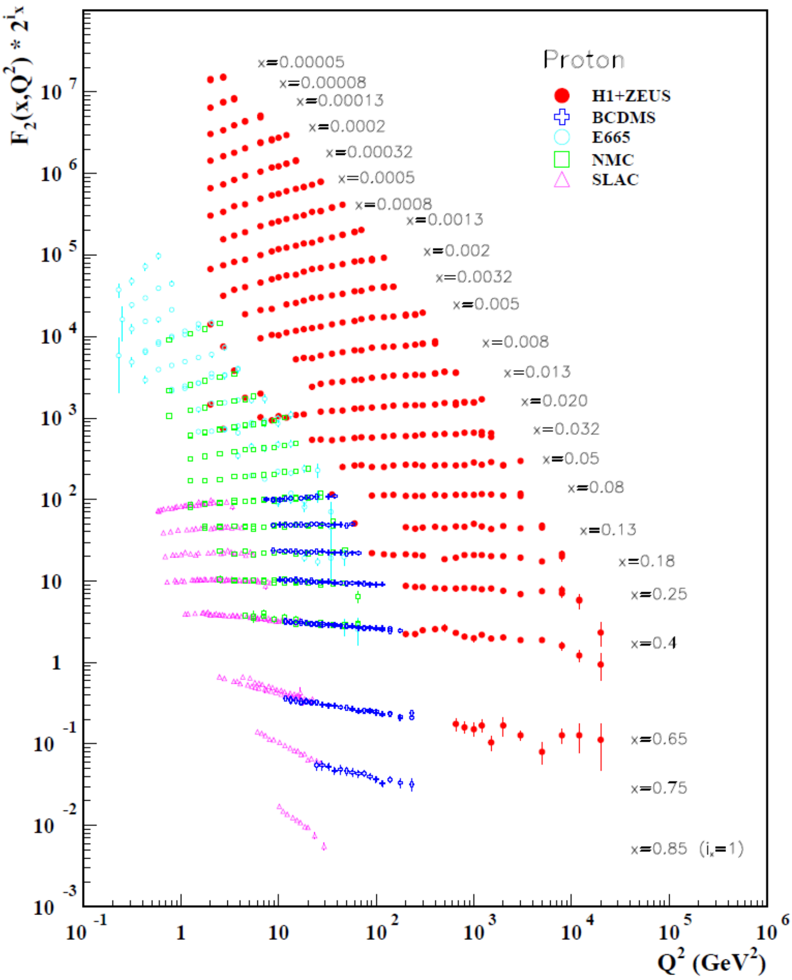

Figure 1.1: $F_2^P(x,Q^2)$ measured by DIS. [1] We can check covered Q^2 and x range by experimental data are large.

the sum of each parton's charge.

$$
\begin{aligned}
1 &= \sum_q e_q \int_0^1 dx\{q(x) - \bar{q}(x)\} \\
&= \frac{2}{3}\int_0^1 dx\{u(x) - \bar{u}(x)\} - \frac{1}{3}\{d(x) - \bar{d}(x)\} + \sum_{s,g} e_q \int_0^1 dx\{q(x) - \bar{q}(x)\} \\
&= \frac{2}{3} \times 2 - \frac{1}{3} \times 1 + 0
\end{aligned}
\tag{1.7}
$$

Here no electric charge of gluon is used.

For the momentum, similar attempt is also possible. The sum rule for proton momen-

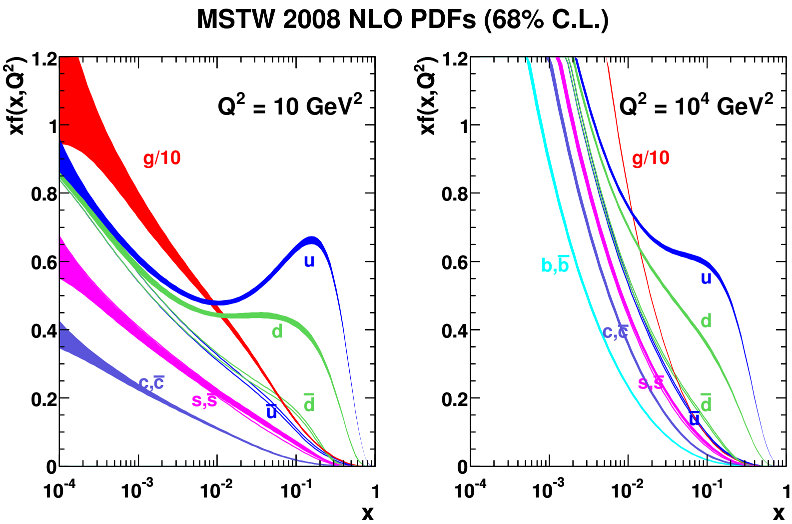

Figure 1.2: MSTW 2008 NLO PDFs. [2] Unpolarized PDFs are reasonablly well constrainted.

tum is

$$1 = \sum_q \int_0^1 dxx\{q(x) - \bar{q}(x)\} \tag{1.8}$$

F_2^P and F_2^N[1] measurements reveal that about 50% of proton momentum is carried by gluon and contributions of other quarks except up and down quarks are limited.

1.2 Spin Structure of Proton

Next fundamental property of proton should be understood its spin. Proton spin should be explained by the sum of each parton's spin and PDF. However understanding proton spin structure is challenging because polarized PDFs ($\Delta f(x,Q^2)$) are needed in here and experimental difficulties are added. The definition of $\Delta f(x,Q^2)$ is

$$\Delta f(x,Q^2) \equiv f_+(x,Q^2) - f_-(x,Q^2) \tag{1.9}$$

where $f_{+(-)}(x,Q^2)$ is the probability of finding a parton f with momentum fraction x and helicity (anti)aligned to the proton helicity at given Q^2.

1.2.1 Ellis-Jaffe Sum Rule

The first proposed spin sum rule is Ellis-Jaffe sum rule [3], [4] which considered spin constributions from valence quarks spin and those angular momentum assuming no spin

[1] Structure function of neutron

contribution of strange quark.

$$S_z^P = \frac{1}{2} = \frac{1}{2}\Delta\Sigma + L_z^q \tag{1.10}$$

The sum rule predicted that $\int_0^1 dx g_1^P(x,Q^2) = 0.189 \pm 0.005$ where $g_1^P(x,Q^2)$ is polarized structure function of proton.

1.2.2 EMC Result and Spin Crisis

The Ellis-Jaffe sum rule was tested by polarized experiments and $g_1^P(x,Q^2)$ measurements. The striking result was obtained by polarized DIS experiment by European Muon Collaboration (EMC) at CERN.[2] In the experiment, longitudinally polarized muon and proton scatterings were carried out. In the experiment, the asymmetry of cross section was measured.

$$A_1^P = \frac{\sigma_{+-} - \sigma_{++}}{\sigma_{+-} + \sigma_{++}} \tag{1.11}$$

where "+-" means helicities of muon and proton are opposite and "++" means helcities of muon and proton are same. The asymmetry can be converted into $g_1^P(x,Q^2)$ by

$$A_1^P = \frac{g_1^P(x,Q^2)}{F_1^P(x,Q^2)} \tag{1.12}$$

The EMC measurement covered $0.01 < x < 0.7$.

The EMC measurement reveals that $\int_0^1 dx g_1^P(x,Q^2) = 0.126 \pm 0.010(stat.) \pm 0.015$-$(syst.)$ as Fig. 1.3. The result showed that the Ellis-Jaffe sum rule is wrong clearly. The result implied that

$$\begin{aligned}
S_z^u &= \frac{1}{2}(\Delta u + \Delta\bar{u}) = +0.391 \pm 0.016(stat.) \pm 0.023(syst.) \\
S_z^d &= \frac{1}{2}(\Delta d + \Delta\bar{d}) = -0.236 \pm 0.016(stat.) \pm 0.023(syst.) \\
S_z^s &= \frac{1}{2}(\Delta s + \Delta\bar{s}) = -0.095 \pm 0.016(stat.) \pm 0.023(syst.) \\
\Delta\Sigma &= \Delta u + \Delta\bar{u} + \Delta d + \Delta\bar{d} + \Delta s + \Delta\bar{s} \\
&= +0.120 \pm 0.094(stat.) \pm 0.138(syst.)
\end{aligned} \tag{1.13}$$

It is clear that we can not explain proton spin by spin sum of quarks.

The implication of the EMC result has intrigued "spin crisis" and triggered world-wide endeavors to understand proton spin structure.

[2]The first polarized DIS experiments were carried out at Standford Linear Accelerator (SLAC) with polarized electrons and polarized protons. [5], [6], and [7] However, the results of the exeriments were consistent with the Ellis-Jaffe's prediction with limited x range. See Fig. 1.3.

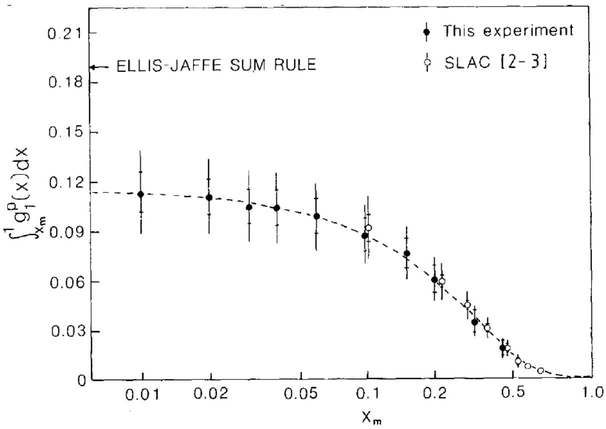

Figure 1.3: EMC Result of $g_1^P(x,Q^2)$. [8] It is clear that the prediction of the Ellis-Jaffe sum rule is wrong.

1.2.3 Jaffe-Monohar Sum Rule

The Ellis-Jaffe sum rule was replaced by the Jeffe-Monohar sum rule. [9]

$$S_z^P = \frac{1}{2} = \frac{1}{2}\Delta\Sigma + L_z^q + \Delta G + L_z^g \tag{1.14}$$

where ΔG and L_z^g means spin contribution of gluon spin and its angular momentum. Thus ΔG becomes key of understanding proton spin structure and measuring $\Delta g(x,Q^2)$ becomes very important. Contraining $\Delta g(x,Q^2)$ is the goal of the dissertation.

1.2.4 Current Knowledge of Proton Spin Structure

After the shocking result of EMC, many polarized DIS, SIDIS, and $p+p$ scatterings have been carried out. With the experimental data, QCD global analyses have been done and $g_1^P(x,Q^2)$ and $\Delta f(x,Q^2)$ are measured. Fig. 1.4 shows world data of $g_1^P(x,Q^2)$. Fig. 1.5 and Fig. 1.6 show $\Delta f(x,Q^2)$ by global analyses DSSV group.

The $\Delta f(x,Q^2)$ results of Fig. 1.5 has been published in 2009 and polarized DIS and SIDIS results are the main sources of the containts. We can check the uncertainties are large for $\Delta\bar{u}(x,Q^2)$, $\Delta\bar{d}(x,Q^2)$ and $\Delta g(x,Q^2)$.

As the goal of the dissertation is constraining ΔG, let's focus on $\Delta g(x,Q^2)$. The reason of the poorly constrained $\Delta g(x,Q^2)$ is gluon has no electric charge and the effect of gluon is suppressed in DIS and SIDIS. Thus polarized $p+p$ scattering is best tool to constraining $\Delta g(x,Q^2)$ because $p+p$ scattering can sense gluon at leading order.

With the results of polarized $p+p$ scatterings at $\sqrt{s} = 62.4$ GeV and $\sqrt{s} = 200$ GeV at RHIC PHENIX [13], [14][3] and STAR [15][4], significant constraint on $\Delta g(x,Q^2)$ was

[3] pseudorapidity coverage, $|\eta| < 0.35$

[4] pseudorapidity coverage, $|\eta| < 0.5$ and $0.5 < |\eta| < 1.0$

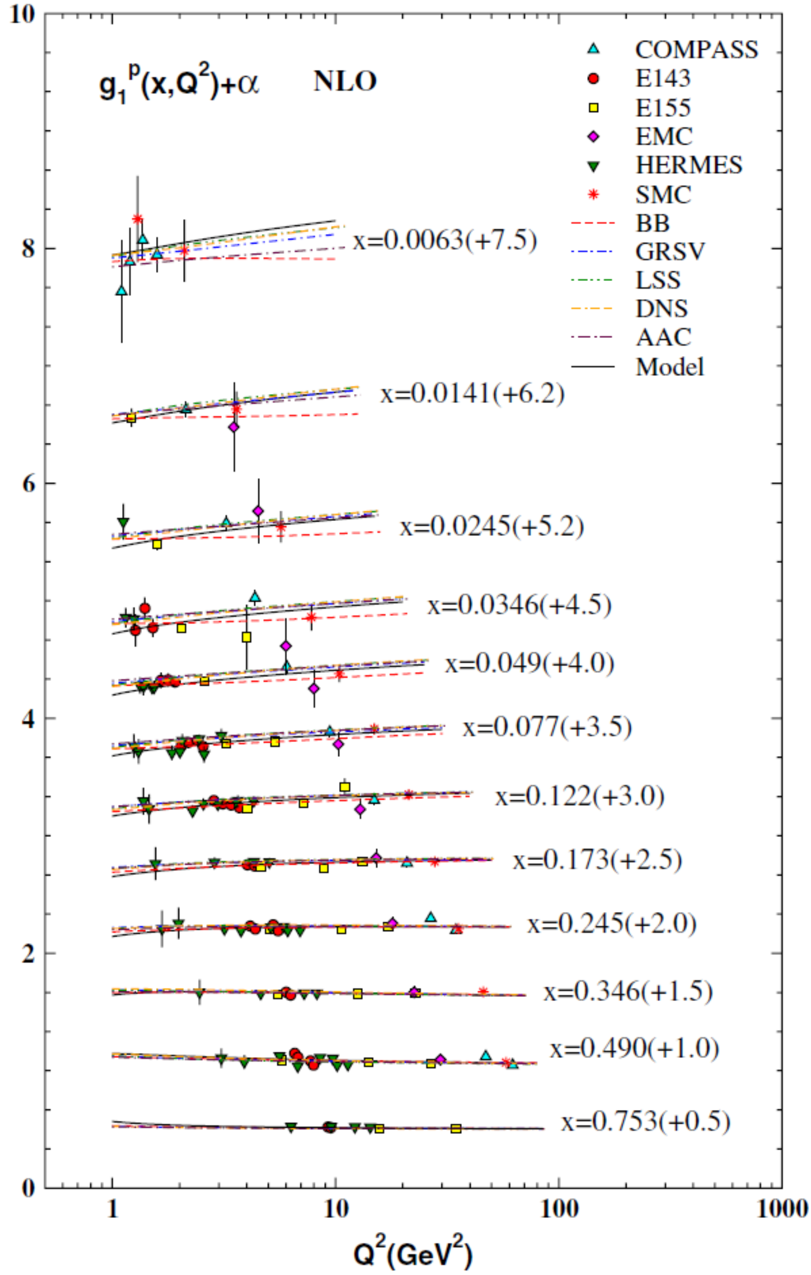

Figure 1.4: $g_1^P(x,Q^2)$. [10] Compared with Fig. 1.1, the number of data points, and kinematic coverage are limited.

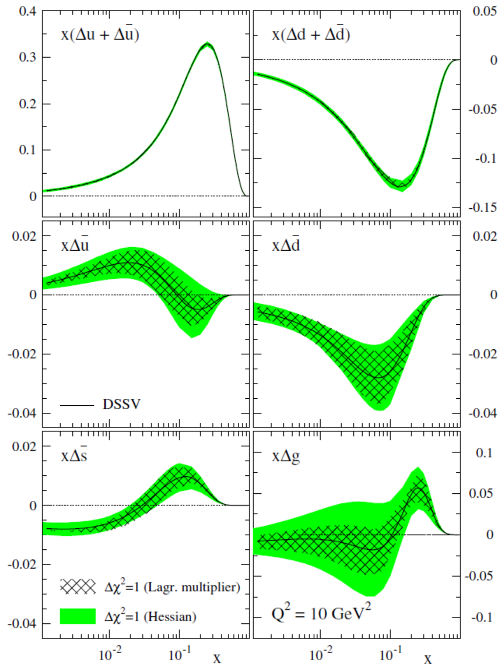

Figure 1.5: 2009 $\Delta f(x,Q^2)$ by DSSV. [11] Shaded regions by grid and green band are uncertainty regions by Lagrange multiplier and Hessian methods, respectively.

achieved. Fig. 1.6 shows the result. By comparing 2014 new fit result (red solid line) and the fit result without the PHENIX and STAR result (blue dashed and dotted line), we can check the main source of constraint on $\Delta g(x,Q^2)$ is the polarized $p+p$ scatterings data. Within the two vertical dashed lines, the fits are reasonablly converged. However, the fits diverge in outside of the RHIC $\sqrt{s}=200$ GeV region, especially in lower x region. Fig. 1.7 shows the truncated moments of $\Delta g(x,Q^2)$. With current $\Delta g(x,Q^2)$, positive ΔG is supported but uncertainty is large due to remained large uncertainty in lower x region. By comparing the green and blue bands, we can check the polarized $p+p$ scatterings experiment is sensitive to $\Delta g(x,Q^2)$, again.

Thus, it is very important to expand the experimental sensitivity to lower x region to constrain $\Delta g(x,Q^2)$. To lower x region, one possible way is doing similar experiment at increasing $\sqrt{s}$ and the other way is doing the experiment at forward pseudorapidity region. The accessing to lower x region by increased $\sqrt{s}=510$ GeV is discussed in the dissertation.

1.3 Proton-Proton Scattering

As data of polarized $p+p$ scattering are analyzed in the dissertation, let's summarize how the process that $p+p$ are scattered and hadron h is materialized is explained in terms of factorization.

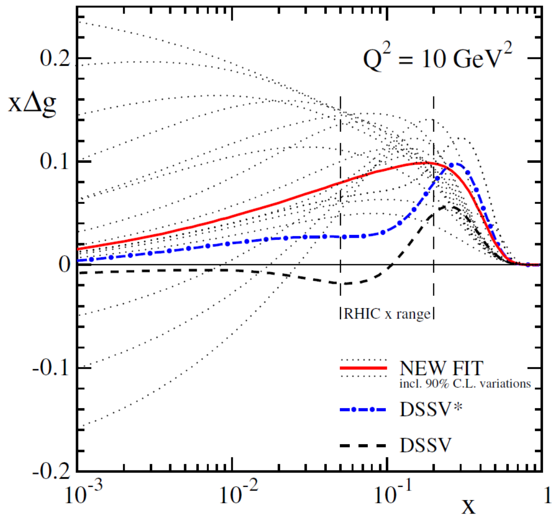

Figure 1.6: 2014 $\Delta g(x,Q^2)$ at $Q^2 = 10$ GeV^2 by DSSV. [12] Two vertical dashed lines represent the constrained region by RHIC $\sqrt{s} = 200$ GeV Runs. Black dashed line represents 2009 result of Fig. 1.5. Blue dashed and dotted line represents 2014 result without the updates of PHENIX and STAR. Red solide line represents $\Delta g(x,Q^2)$ including all the experimental data. Dashed lines represents 90% confident level regions of the alternative fits. For the discussion, see text.

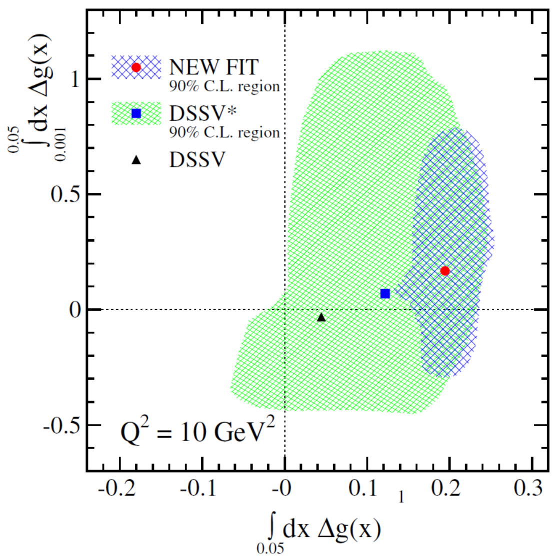

Figure 1.7: Truncated moments of $\Delta g(x,Q^2)$ at $Q^2 = 10$ GeV^2 computed for $0.05 \leq x \leq 1$ and $0.001 \leq x \leq 0.05$ with 90% confident levels bands by DSSV. [12] The green band is obtained with blue dashed and dotted line and blue band is obtained with red solid line in Fig. 1.6.

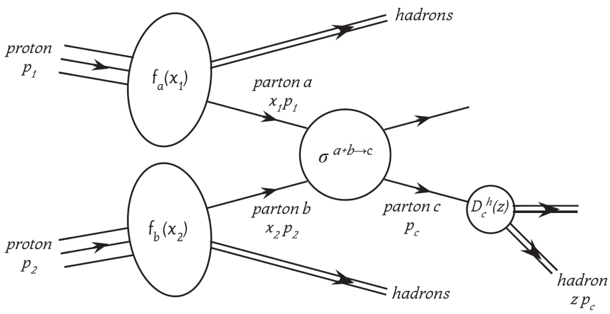

Figure 1.8: pQCD fractorization of $p+p$ scattered and resulting hadron h is materialzied. [14]

Fig. 1.8 shows pQCD factrization of $p+p$ scattered and resulting hadron h is materialzed. The probability of finding parton in each proton is governed by $f(x,Q^2)$ of parton a and b. The process that parton $a+b$ is scattered and resulting parton c emerged is governed by partonic elastic scattering $\hat{\sigma}^{a+b\to c+X}$ which is calculatable by pQCD. The probability that parton c materialized into h is governed by $D_c^h(z,Q^2)$.

$$\begin{aligned}\sigma^{p+p\to h+X} = &\sum_{f_{a,b}=q,\bar{q},g} \int_0^1 dx_1 \int_0^1 dx_2 \int_0^1 dz f_a(x_1,Q^2)\times f_b(x_2,Q^2) \\ &\times \hat{\sigma}_{elastic}^{a+b\to c+X}(x_1P_1,x_1P_2,zP_c)\times D_c^h(z,Q^2)\end{aligned} \tag{1.15}$$

In $p+p$ scattering, gluon participate the reaction in the first order. Thus $p+p$ scattering is sensitive to extracting information of gluon. However neither x nor Q^2 are directly measured in $p+p$ scattering and that is demerit of it.

1.4 Accessing the $\Delta g(x,Q^2)$ through Longitudinally Polarized $p+p$ Scatterings at $\sqrt{s}=510$ GeV and A_{LL} of π^0 Production

In the dissertation, $\Delta g(x,Q^2)$ is accessed by measuring the double helicity asymmetry of π^0 production in longitudinally polarized $p+p$ scatterings ($A_{LL}^{\pi^0}$) at $\sqrt{s}=510$ GeV.

The definition of A_{LL}^h is

$$A_{LL}^h = \frac{\Delta\sigma^{p+p\to h+X}}{\sigma^{p+p\to h+X}} \tag{1.16}$$

Here, the $\Delta\sigma$ is

$$\Delta\sigma = \sigma_{++}+\sigma_{--}-\sigma_{+-}-\sigma_{-+} \tag{1.17}$$

where the "+" and "-" represent helicity of longitudinally polarized proton is positive or negative. The two signs indicate the helicities of the two protons, in sequence. The σ is

$$\sigma = \sigma_{++} + \sigma_{--} + \sigma_{+-} + \sigma_{-+} \tag{1.18}$$

Thus A^h_{LL} can be written as

$$A^h_{LL} = \frac{\sigma_{++} + \sigma_{--} - \sigma_{+-} - \sigma_{-+}}{\sigma_{++} + \sigma_{--} + \sigma_{+-} + \sigma_{-+}} \tag{1.19}$$

Because the strong interaction is invariant on parity operation, the A^h_{LL} can be written as

$$A^h_{LL} = \frac{\sigma_{++} - \sigma_{+-}}{\sigma_{++} + \sigma_{+-}} \tag{1.20}$$

for a shorthand where ++ (+-) is written for both ++ and -- (+- and -+).

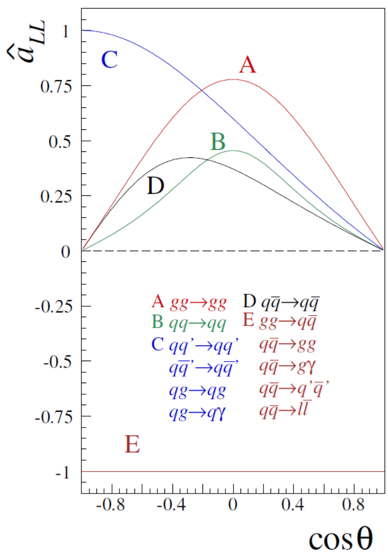

Figure 1.9: $\hat{a}_{LL}$ by leading-order pQCD calculation. [16] The measurement in the dissertation covers mid rapidity, corresponding $\cos\theta \sim 0$.

As discussed in Sec. 1.3, the cross section can be written as $f(x, Q^2)$, $\hat{\sigma}_{elastic}$ and $D^h_q(z, Q^2)$. Thus A^h_{LL} can be written in the three ingredients also.

$$\begin{aligned} A^h_{LL} &= \frac{\sigma_{++} - \sigma_{+-}}{\sigma_{++} + \sigma_{+-}} \\ &= \frac{\sum_{f_{a,b}=q,\bar{q},g} \Delta f_a \otimes \Delta f_b \otimes \Delta\hat{\sigma}^{a+b\to c+X}_{elastic} \otimes D^h_c}{\sum_{f_{a,b}=q,\bar{q},g} f_a \otimes f_b \otimes \hat{\sigma}^{a+b\to c+X}_{elastic} \otimes D^h_c} \\ &= \frac{\sum_{f_{a,b}=q,\bar{q},g} \Delta f_a \otimes \Delta f_b \otimes \hat{\sigma}^{a+b\to c+X}_{elastic} \times \hat{a}^{a+b\to c+X}_{LL} \otimes D^h_c}{\sum_{f_{a,b}=q,\bar{q},g} f_a \otimes f_b \otimes \hat{\sigma}^{a+b\to c+X}_{elastic} \otimes D^h_c} \end{aligned} \tag{1.21}$$

where, $\hat{a}_{LL}^{a+b\to c+X} = \Delta\hat{\sigma}_{elastic}^{a+b\to c+X} / \hat{\sigma}_{elastic}^{a+b\to c+X}$. Fig. 1.9 shows $\hat{a}_{LL}$ of various channels. It is clear that $\Delta f(x, Q^2)$ is accessible by measuring A_{LL}^{h} by Eq. 1.21.

In the dissertation, A_{LL} of π^0 ($A_{LL}^{\pi^0}$) is measured to access $\Delta g(x, Q^2)$ $\sqrt{s} = 510$ GeV. The advantages of π^0 channel are

- Large fraction of π^0 is made by gluon-gluon and gluon-quark scattering.
- The FFs for π^0 are reasonally well constrained and cross section of π^0 is nicely understood.
- π^0 peak is clearly identifiable.
- π^0 statistics is very rich.

Fig. 1.10 the relative constributions of partonic subprocesses to include π^0 production. We can check that large fraction of π^0 is made by gluon-gluon and gluon-quark scattering. Thus $A_{LL}^{\pi^0}$ is sensitive to $\Delta g(x, Q^2)$.

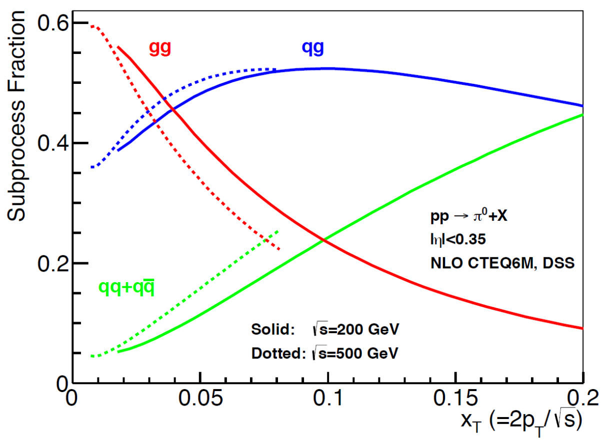

Figure 1.10: Relative contributions of partonic subprocesses to inclusive π^0 production. [17]

Fig. 1.11 shows the FFs for π^+ by DSS group. The FFs for π^- are obtained by charge conjugation and those for π^0 by assuming $D_i^{\pi^0} = (D_i^{\pi^+} + D_i^{\pi^-})/2$. The $e^- + e^+$ annihilation data, the SIDIS multiplicites data and the $p+p$ scattering data was used to constrain the FFs. Fig. 1.12 shows measured π^0 cross section from $p+p$ scattering at $\sqrt{s} = 510$ GeV and corresponding theoretical curve by pQCD calculation. We can check the theoretical curve agrees with the experimental data. Thus the factorization and the universality is well supported and we can use the schemes can be applied to interpret A_{LL} result without any harm.

Fig. 4.1 shows di-photon invariant mass distribution. π^0 peak is clear and it enables pariticle identification. Any false asymmetry from wrong particle identification can be suppressed.

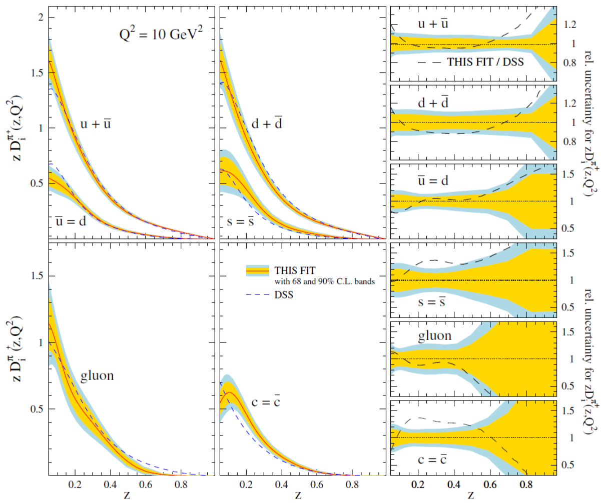

Figure 1.11: 2015 π^+ fragmentation functions at $Q^2 = 10$ GeV^2 by DSS group. [18] Uncertainties estimated at 68% and 90% confident level are indicated by inner and outer shaded bands, respectively. The right-hand side panels show the corresponding relative uncertainties. 2007 DSS FFs is shown by the dashed line.

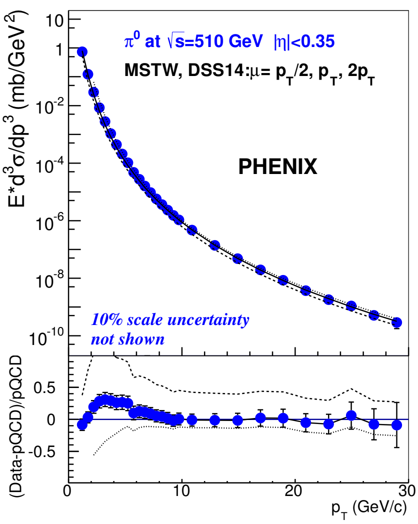

Figure 1.12: π^0 cross section from $p+p$ at $\sqrt{s} = 510$ GeV. MSTW PDFs (Fig. 1.2) and DSS14 FFs (Fig. 1.11) are used to calculate the theoretical curve. Bottom pannel is comparison plots of the experimental data and the theoretical curve.

PHENIX is very well suited for measuring π^0 and the statistic of π^0 is very rich. Tab. 5.3, Tab. 5.4, Tab. 5.5 and Tab. 5.6 are summary table of π^0 statistics. With the rich statistics, A_{LL} can be measured precisely.

With the increased $\sqrt{s} = 510$ GeV, this measurement can cover $0.01 \leq x \leq 0.1$[5], where large uncertainty remain (See. Fig. 1.6 and Fig. 1.7), while the previous measurements [14], [15] of RHIC at $\sqrt{s} = 200$ GeV Run covered $0.05 \leq x \leq 0.2$ region[6].

---

[5] $x_T = \frac{2P_T}{\sqrt{s}}$, the approximated version of x. The measurement covers $2\ \mathrm{GeV}/c \leq P_T \leq 20\ \mathrm{GeV}/c$

[6] The region is obtained by the STAR result mainly because the PHENIX result failed to measure non-zero asymmetry out of statistical unceratinty while the STAR result oberved positive asymmetry. Thus the PHENIX result could not contrain $\Delta g(x, Q^2)$ much.

Chapter 2

RHIC

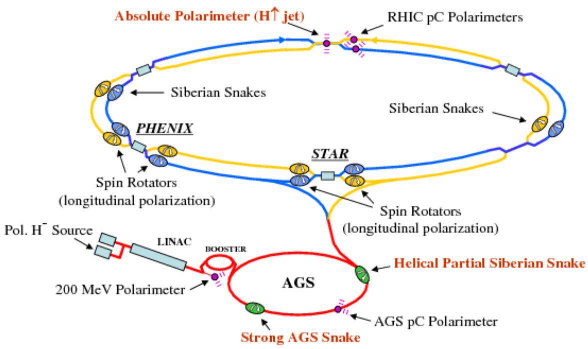

Figure 2.1: Cartoon of Relativistic Heavy Ion Collider. Only spin related devices are drawn. [19]

2.1 RHIC General

The Relativistic Heavy Ion Collider (RHIC) [20], [19] at Brookhaven National Laboratory (BNL) is very complex facility to study the proton spin structure and quark-gluon plasma. As the measurement is focusing on proton spin structure, especially ΔG, spin related elements of RHIC will be introduced in this chapter. Fig. 2.1 shows layout of RHIC.

RHIC can accelerate polarized protons up to at energy 255 GeV. Polarized protons injected by the polarized proton source (See. Subsec. 2.2.1 for detail.) are accelerated by Linac at energy up to 200 MeV. The protons are injected to Alternating Gradient Synchrotron (AGS) via Booster, where the protons are accelerated at energy 1.5 GeV, and accelerated at energy 23.4 GeV. The protons are finally injected to RHIC. The processes are repeated until every bunches of two RHIC rings are filled except last nine bunches for abort kicker insert. The last nine empty bunches are called the abort gap. Once the bunches are filled, the store or fill lasts 8 hours usually. Each fill is identified its number so called “fillnumber”. After the fill, the protons are accelerated at energy up to 255 GeV. Since each bunch are filled and accelerated independently, the option of direction of polarization is independently for each bunch.

The two accelerating and store RHIC rings are so called the beam and yellow rings. Each RHIC ring can support 120 bunches. The protons in blue ring rotates clockwise while the protons in yellow ring rotates counter clockwise. RHIC has six possible interaction regions but collision occurred only at 6 o’clock, where STAR Detector is and at 8 o’clock, where PHENIX detector is, during the 2012 Run (Run12) and 2013 Run (Run13).

2.2 RHIC Spin Related Components

2.2.1 Optically-Pumped Polarized H^- Ion Source

The polarized beam is produced in the Optically-Pumped Polarized H^- Ion Source (OPPIS). [21] Hydrogen atoms are injected by atomic hydrogen source and the atoms are ionized (H^+) in pulse He-gaseous ionizer. The ions are converted to electron-spin polarized H atom by electron pick-up in an optically pumped Rb-vapor cell. Then the polarization is transferred to the nucleus via Sona-transition. The polarized H atoms are negatively ionized in Na-jet ionizer and the H^- beam is injected to radio-frequency quadrupole.

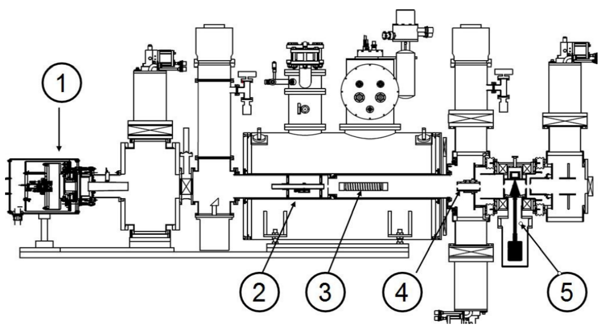

Figure 2.2: Structure of polarized proton source. 1. atomic hydrogen source; 2. pulse He-gaseous ionizer cell; 3. optically pumped Rb-vapor cell; 4. Sona-transition; 5. Na-jet ionizer[21]

Before Run13, there was OPPIS upgrade. It is main reason of luminosity upgrade of Run13.

2.2.2 Siberian Snake

To avoid depolarization resonance, RHIC has two Siberian Snakes for each RHIC beam. [19] The Siberian Snake consists of four superconducting helical dipole magnet and generates 180° spin rotation about a horizontal axis.

The evolution of spin in homogeneous magnetic field such as particle accelerator is governed by Thomas-BMT equation [22]

$$\frac{d\vec{s}}{dt} = -\frac{e}{\gamma m}[(1+G\gamma)\vec{B}_{\perp} + (1+G)\vec{B}_{\parallel}] \times \vec{s} \tag{2.1}$$

where G is the anomalous magnetic moment of proton 1.7928, $\vec{s}$ is spin vector at particle rest frame and $\vec{B}_{\perp(\parallel)}$ is magnetic field perpendicular(parallel) to the particle's motion. At high energy i.e., at large γ, Gγ becomes overwhelming factor. At top RHIC energy Gγ reaches 487. Thus $\vec{B}_{\perp}$ become dominant and the equation means spin $\vec{s}$ precesses about perpendicular holding field. The factor Gγ is called the spin tune, ν_{sp}.

The acceleration of polarized beams is complicated by the depolarizing resonances. There are two types of main depolarizing resonances. The one is imperfection resonances due to the magnet errors. The other is intrinsic resonances due to the focusing fields. Close to the resonances, the precession axis is perturbed away from vertical direction.

To avoid the depolarizing resonances, the Siberian Snake rotate the precession axis by 180°. Then the perturbation is canceled and the beam polarization is preserved.

2.2.3 RHIC Polarimeters

To measure polarization of beams, RHIC has two polarimeters. The polarimeters measure the polarization by measuring the asymmetry (A_N) of in proton-carbon elastic scattering or proton-proton elastic scattering.

Proton-Carbon Polarimeter

The Proton-Carbon Polarimeter (pC) [19] bases on the asymmetry in proton-carbon elastic scattering in the Coulomb-Nuclear Interaction (CNI) region. Beam is incidented on very thin carbon filament (25nm) and scattered carbon is detected silicon strip detectors. With the measurement, the asymmetry of recoiled carbon obtained.

$$P = \frac{\varepsilon_{N,pC}}{A_{N,pC}} \tag{2.2}$$

Then, the beam polarization is obtained by dividing the observed asymmetry ($\varepsilon_{N,pC}$) by the analyzing power ($A_{N,pC}$). Fig. 2.4 show model predicted A_N of $p+C$ and $p+p$.

The collision rate of pC polarimeter is very high $\sim 2\times10^6 events/s$. Thus pC polarimeter can measure fill-by-fill polarizations and even polarization decay within single fill. Usually, pC polarimeter measurement is done three times within single fill; after new fill, middle of fill and right before fill dump.

However pC polarimeter measures only relative polarization because of uncertainty from A_N. For normalization, second polarimeter which can measure absolute polarization is necessary. The second polarimeter is H-jet polarimeter.

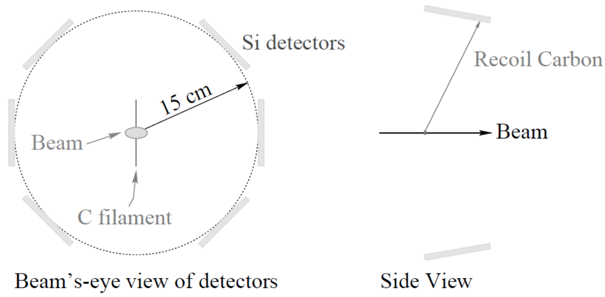

Figure 2.3: Structure of pC polarimeter. Recoiled carbon is detected by silicon strip detectors.

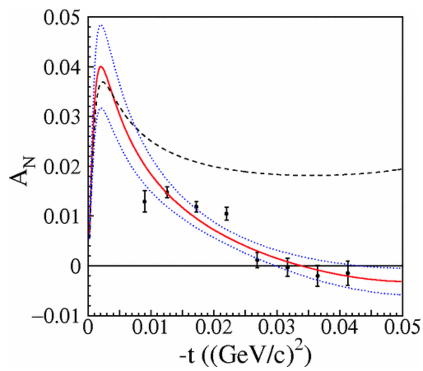

Figure 2.4: Analyzing power of $p+C$. [23] for experimental points and [24] for theory curve.

H-Jet Polarimeter

The second polarimeter is H-Jet Polarimeter. [25] In the H-Jet polarimeter, beam is incidented on polarized H-Jet and recoiled protons are detected by silicon detectors. Because both of beam and H-Jet are polarized, ε_N of beam and H-Jet are measured simultaneously. By measuring the two ε_N, the beam polarization is measured without the contamination from A_N,

$$P_{beam} = P_{H-Jet}\frac{\varepsilon_{Beam}}{\varepsilon_{H-Jet}} \tag{2.3}$$

where, polarization of H-Jet, P_{H-Jet} is measured by Breit-Rabi polarimeter. Thus, H-Jet polarimeter can measure an absolute polarization of beam.

However collision rate is too low for H-Jet, fill-by-fill measurement is impossible for H-Jet polarimeter and is used for normalizing pC polarimeter with whole Run statistics.

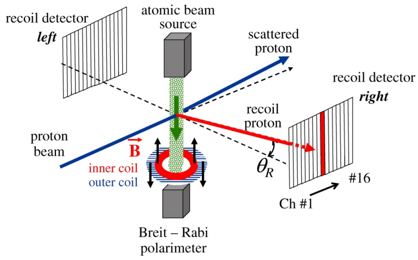

Figure 2.5: Structure of H-Jet polarimeter. [25]

2.2.4 Spin Rotators

As discussed in Subsec. 2.2.2, the stable direction of polarization is vertical. However longitudinal polarization is necessary for A_{LL} measurement. The Spin Rotators, which sit at right before and after of the interaction region, rotate the direction spin to longitudinal direction and facilitate A_{LL}measurement. The result of the Spin rotators and the direction of polarization in PHENIX interaction region is discussed in Sec 3.5.

2.3 Run12 and Run13 Longitudinal $p+p$ Collision at $\sqrt{s} = 510$ GeV

There was 5 weeks of longitudinal $p+p$ collision at $\sqrt{s} = 510$ GeV out of 18 weeks of Run12. [26]. Whole 13 weeks running period was dedicated for longitudinal $p+p$ collision at $\sqrt{s} = 510$ GeV for Run13. [27] Fig. 2.6 shows the integrated luminosity as function of running weeks of RHIC polarized proton Runs.

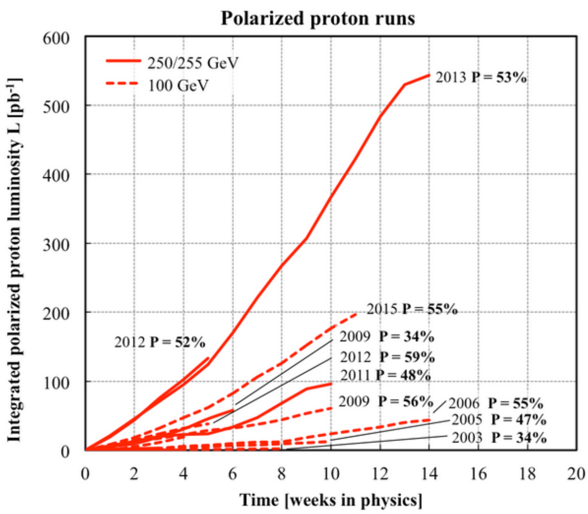

Figure 2.6: RHIC polarized proton Runs history.

2.3.1 Polarization

Fill-by-fill polarization values and those uncertainties can be found in [28] and [29]. For Run13, instead of using average polarization, run-by-run polarization values are calculated with initial polarization value and polarization decay rate. [30] The polarization values are summarized in Fig. 2.7 and Fig. 2.8.

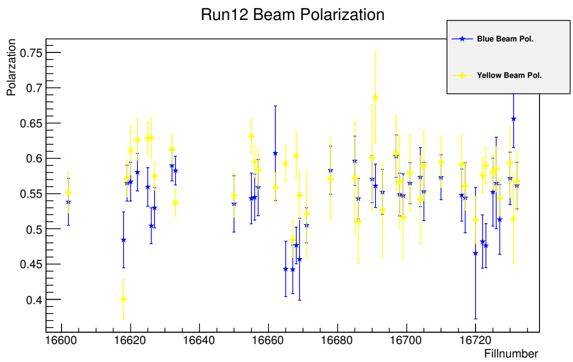

Figure 2.7: Run12 polarizations

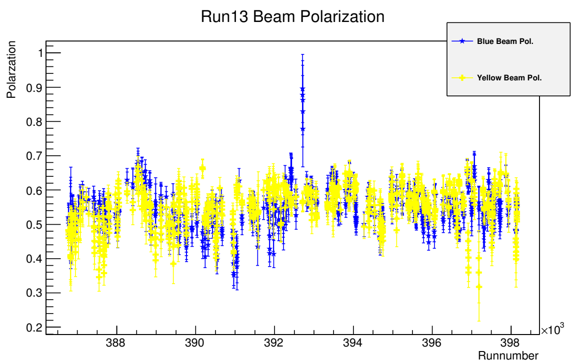

Figure 2.8: Run13 polarizations

The polarimeter group advises to use Run12 value for global systematic uncertainty on $P_B P_Y$ of 6.5% for Run13 as well.

2.3.2 Spin Patterns

As discussed in Sec. 2.1, polarization of each bunch is independently selected. The polarizations are selected to cover all four combinations of "++", "+-", "-+", and "–" collisions and to assure that any systematic effects from detector or trigger efficiency fluctuations is not arise. The filling scheme of polarizations of bunches is called Spin Pattern. To assure any systematic effects of the filling scheme is not arise, several spin patterns were used.

Run12 Spin Patterns

During Run12, 8 spin patterns were used. The configurations of each spin pattern are summarized in Tab. 2.1.

P1 B	+	-	+	-	-	+	-	+
Y	+	+	-	-	+	+	-	-
P2 B	-	+	-	+	+	-	+	-
Y	+	+	-	-	+	+	-	-
P3 B	+	-	+	-	-	+	-	+
Y	-	-	+	+	-	-	+	+
P4 B	-	+	-	+	+	-	+	-
Y	-	-	+	+	-	-	+	+
P5 B	+	+	-	-	+	+	-	-
Y	+	-	+	-	-	+	-	+
P6 B	+	+	-	-	+	+	-	-
Y	-	+	-	+	+	-	+	-
P7 B	-	-	+	+	-	-	+	+
Y	+	-	+	-	-	+	-	+
P8 B	-	-	+	+	-	-	+	+
Y	-	+	-	+	+	-	+	-

Table 2.1: Spin patterns used in Run12. “+” means positive helicity and “-” means negative helicity.

The 8 spin patterns can be sorted into 2 patterns. For example, P1, P4, P5 and P8 belong to equivalent pattern “SOOS” because P1 and P5 are equivalent under beam exchange and P1 and P4 are equivalent under parity inversion. The spin pattern grouping is summarized in Tab. 2.2. As discussed in Subsec. 7.2.1, spin patterns are separated for calculating $A_{LL}^{\pi^0}$.

SOOS	P1	P4	P5	P8
OSSO	P2	P3	P6	P7

Table 2.2: Run12 Sort of spinpattern.

Run13 Spin Patterns

During Run13, 16 spin patterns were used. Old spin pattern, P1 - P8 were used in the initial weeks two of Run13. For remaining period of Run13, new spin pattern, P21 - P28 were used. The configurations of each spin pattern are summarized in Tab. 2.3 and Tab. 2.4.

With same discussion in Subsec 2.3.2, 16 spin patterns can be sorted into 4 patterns. The spin pattern grouping is summarized in Tab. 2.5.

P1 B	+	+	-	-	+	+	-	-	+	+	-	-		
Y	+	+	+	+	-	-	-	-	+	+	+	+	-	-
P2 B	-	-	+	+	-	-	+	+	-	-	+	+		
Y	+	+	+	+	-	-	-	-	+	+	+	+	-	-
P3 B	+	+	-	-	+	+	-	-	+	+	-	-		
Y	-	-	-	-	+	+	+	+	-	-	-	-	+	+
P4 B	-	-	+	+	-	-	+	+	-	-	+	+		
Y	-	-	-	-	+	+	+	+	-	-	-	-	+	+
P5 B	+	+	+	+	-	-	-	-	+	+	+	+	-	-
Y	+	+	-	-	+	+	-	-	+	+	-	-		
P6 B	+	+	+	+	-	-	-	-	+	+	+	+	-	-
Y	-	-	+	+	-	-	+	+	-	-	+	+		
P7 B	-	-	-	-	+	+	+	+	-	-	-	-	+	+
Y	+	+	-	-	+	+	-	-	+	+	-	-		
P8 B	-	-	-	-	+	+	+	+	-	-	-	-	+	+
Y	-	-	+	+	-	-	+	+	-	-	+	+		

Table 2.3: Spin patterns used in the initial part of Run13.

Middle of the Run13, bunch filling scheme had been changed. Before the change, bunch ID 29, 30 in Yellow beam and bunch ID 69, 70 in Blue beam were unfilled. To increase statistics the bunches were filled after fillnumber 17408.

P21 B	+	+	-	-	+	+	-	-
Y	+	+	+	+	-	-	-	-
P22 B	-	-	+	+	-	-	+	+
Y	+	+	+	+	-	-	-	-
P23 B	+	+	-	-	+	+	-	-
Y	-	-	-	-	+	+	+	+
P24 B	-	-	+	+	-	-	+	+
Y	-	-	-	-	+	+	+	+
P25 B	+	+	+	+	-	-	-	-
Y	+	+	-	-	+	+	-	-
P26 B	+	+	+	+	-	-	-	-
Y	-	-	+	+	-	-	+	+
P27 B	-	-	-	-	+	+	+	+
Y	+	+	-	-	+	+	-	-
P28 B	-	-	-	-	+	+	+	+
Y	-	-	+	+	-	-	+	+

Table 2.4: Spin patterns used for remaining period of Run13.

SOOSSOO	P1	P4	P5	P8
OSSOOSS	P2	P3	P6	P7
SSOO	P21	P24	P25	P28
OOSS	P22	P23	P26	P27

Table 2.5: Run13 Sort of spinpattern.

Chapter 3

PHENIX

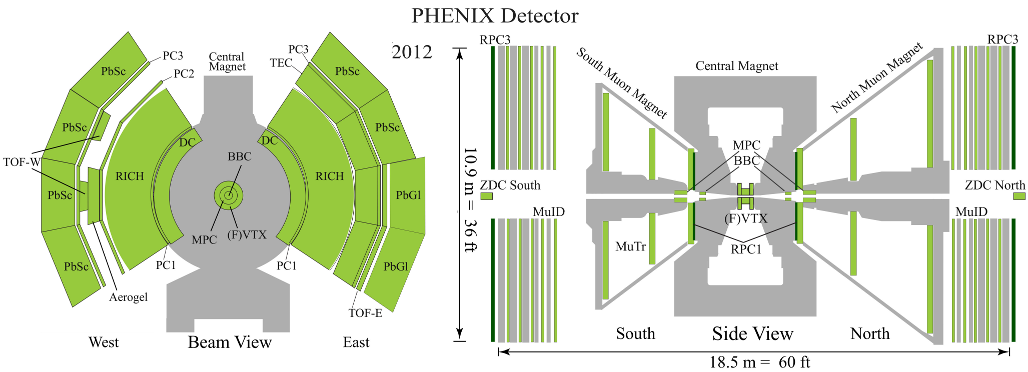

Figure 3.1: PHENIX configuration

3.1 Luminosity Detectors

As discussed in Sec. 4.1, luminosity is one of the main ingredient of this analysis. Thus Beam Beam Counters and Zero Degree Calorimeters are important detectors since the detectors are main luminosity detectors for the analysis.

3.1.1 Beam Beam Counters

The Beam Beam Counters (BBC) [31] are two arrays of 64 quartz Cherenkov radiator with PMTs, which sit at $\pm$1.44m in the z-direction from the center of PHENIX detector and cover $3.1 < |\eta| < 3.9$ in rapidity and full azimuth. The timing resolution of the BBCs is 52$\pm$4 ps for a single PMT. The BBCs have four main purposes.

- Trigger for collisions.
- Primary Luminosity scaler.

- Vertex_z determination for collisions.

- Define T_0 for time of flight (ToF).

BBC reconstructs vertex_z and T_0 by the following manner.

$$\begin{aligned} \text{Vertex}_z &= c(t_N - t_S)/2 \\ T_0 &= (t_N + t_S)/2 \end{aligned} \tag{3.1}$$

, where c is the velocity of light and t_N (t_S) is the average time of prompt particles detected by the BBC North (South). With the timing resolution, the vertex_z resolution of BBC is 5cm in online and 2cm in offline.

As ToF of central arm clusters is used for photon identification as discussed in Subsubsec. 5.3.2, T_0 determination by BBC is important key of the analysis.

One limitation of Eq. 3.1 is the calculation assumes only one collision in a given bunch crossing. In case of a multiple collision, the reconstructed vertex_z will be middle of real vertexes_z. The effect on luminosity is discussed in Sec. 6.4.

3.1.2 Zero Degree Calorimeters

The zero degree calorimeters (ZDC) [32] consist of W-Cu absorber and polymethyl methacrylate optical fiber Cherenkov radiator with PMTs which sit at ±18m in direction from center of PHENIX detector and cover $|\eta| > 6$ in rapidity and full azimuth. ZDCs are primarily used to detect neutron. As Fig. 3.2 shows, charged particles is bent away and only neutron are incident on the ZDC.

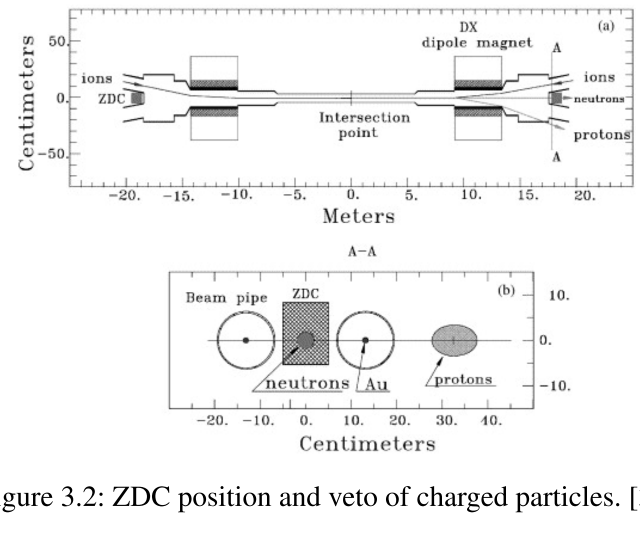

Figure 3.2: ZDC position and veto of charged particles. [32]

The main purpose of ZDC in the analysis is scaling luminosity as secondary scaler. As kinematic coverage and detecting scheme are completely different between BBC and ZDC, BBC and ZDC as luminosity scaler are mutual complementary. However the time resolution of the ZDCs is ∼200 ps and the resolution of vertex_z is ∼30 cm in online and

$\sim$10 cm in offline. The poor resolution of ZDC vertex$_z$ needs correction on scaler counts as discussed in Sec. 6.5 and Sec. 6.6.

3.2 Tracking

Since main probes of the analysis photon pairs from π^0 decay, tracking detectors are not main detectors for the analysis. However tracking and momentum reconstruction are used to reject hadronic and charged particles in the analysis.

3.2.1 Magnet

The PHENIX magnet [33] consists of four parts, inner and outer part of Central Magnets (CM) and north and south forward muon magnets as Fig. 3.3. Only CM is discussed in here. CM is designed to have reasonably uniform magnet field in $R < 2m$ region and minimum field in $R > 2m$ where Drift Chamber and Ring-Imaging Cherenkov detectors are. The other important requirement is no mass in the apertures of central spectrometer arms to avoid interactions of magnets and particles produced from the collisions. Fig. 3.3 is the result of compromise. The resulting field integral is $\int \vec{B} \cdot d\vec{r} = 1.15Tm$ while $\int_{2.4}^{4.0} \vec{B} \cdot d\vec{r} < 0.01Tm$

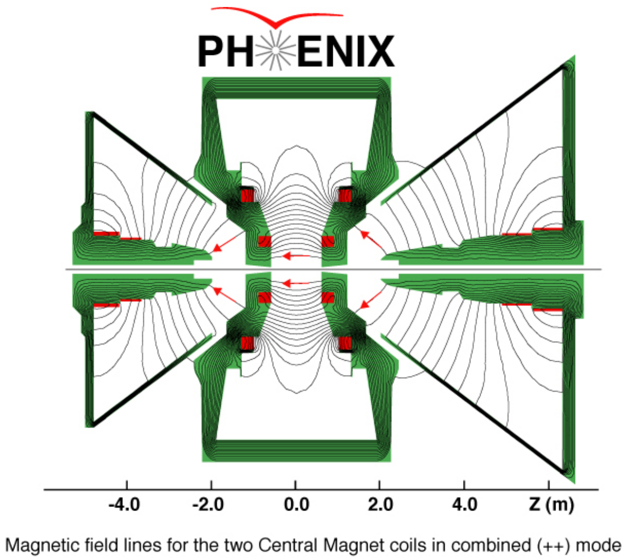

Figure 3.3: PHENIX magnet system. The inner and outer CM at $z = \pm 40cm$ are shown in red marks. [33]

3.2.2 Drift Chambers

PHENIX Drift Chambers (DC) [34] consist of multiwire chamber, filled with 50%/50% mixture of argon and ethane gas. DCs cover $|\eta| < 0.35$ in rapidity and $2 \times \frac{\pi}{2}$ in azimuth.

DCs are located at $2.02 < r < 2.46$ in radially where magnetic field is almost zero. DCs are the primary detector for tracking and P_T reconstruction.

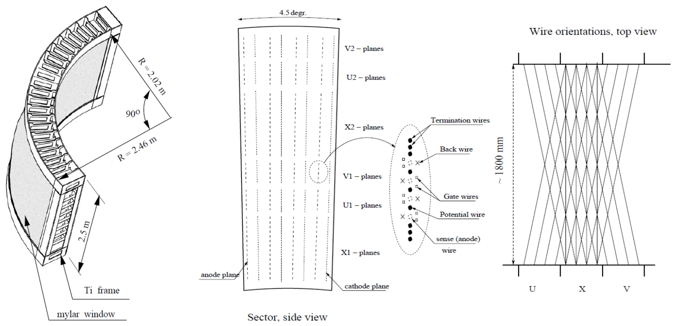

(a) (b)

Figure 3.4: PHENIX DC structure. [34]

Fig. 3.5 shows how P_T is reconstructed by DC. Tracks of charged particles will be bent by magnetic field of CM. Once the particle escapes the magnetic field, the track passing DC is straight. To reconstruct P_T, the angle α is defined. The α is the angle between two vectors, the one is the straight part of track reconstructed by DC and the other is from vertex point to midpoint of DC as Fig. 3.5. By measuring α, P_T can be reconstructed because P_T is proportional $1/\alpha$.

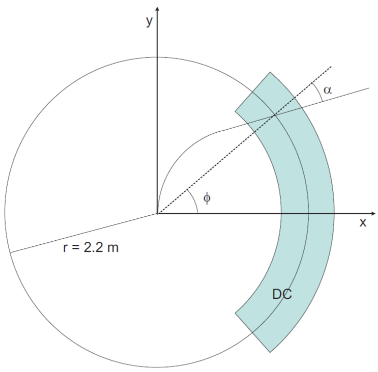

Figure 3.5: P_T reconstruction by DC.

3.2.3 Pad Chambers

The PHENIX Pad Chambers (PC) [34] are the multiwire proportional chambers which cover same acceptance of DC. As Fig. 3.1 shows, there are three layers of PCs in west arm and two layers of PCs in east arm. PCs are highly segmented and specialized in spatial resolution. With the excellent spatial resolution, P_z is reconstructed by PC1.

In the analysis, PC3s, which is about 20 cm (40 cm) closer radially to the z-axis than the Lead Scintillator (Lead Glass), are important because PC3s are used to reject charged particle as discussed in Subsubsec. 5.3.2.

3.3 Ring-Imaging Cherenkov Detector

Ring-Imaging Cherenkov Detector (RICH) [35] is filled with CO_2 gas and sit between PC1 and PC3. RICH is used for particle ID. However the only consideration about RICH in the analysis is e^+e^- conversion of photon. About 2% of photons are converted in e^+e^- pairs in RICH. As discussed in Subsubsec. 5.3.2, special care is needed to handle the converted e^+e^- pairs.

3.4 Electromagnetic Calorimeters

The electromagnetic calorimeters (EMCal) [36] consist of six Lead Scintillators (PbSc) sectors two Lead glasses (PbGl) sectors, which cover $|\eta| < 0.35$ in rapidity and $2 \times \frac{\pi}{2}$ in azimuth. It is primarily designed to measure energy, hit position, and ToF of photons or electrons. PbSc is sampling calorimeter and PbGl is Cherenkov calorimeter. The EMCal is main detector to measure photons from π^0 decay.

3.4.1 PbSc

Six sectors (four sectors in the west arm and two sectors in the east arm) are comprised of PbSc. Each sector contains 36×72 towers covers $|\eta| < 0.35$ in rapidity and $\phi = 22.5°$. The sectors are located at $r = 5m$ radially. Each tower covers 5.5×5.5 cm^2 and consists of 66 sampling cells, composed of 1.5 mm lead slabs in front of 4 mm of scintillating plastic. This corresponds to 18 radiation length ($L_{rad} = 2cm$) or 0.85 nuclear interaction length ($\lambda_I = 44cm$). Fig. 3.6 shows structure of PbSc tower.

PbSc was calibrated using test beam, minimum ionization particles and π^0 mass peak. From the test beam result, the energy resolution of PbSc is

$$\frac{\sigma_E}{E} = \frac{8.1\%}{\sqrt{E(GeV)}} \oplus 2.1\% \tag{3.2}$$

as Fig. 3.7. The position resolution of PbSc is

$$\begin{aligned} \sigma_x(E,\theta) &= \sigma_0(E) \oplus L_{rad} \times sin(\theta) \\ \text{where, } \sigma_0(E) &= 1.55 \oplus \frac{5.7}{\sqrt{E(GeV)}}(mm) \end{aligned} \tag{3.3}$$

Energy corrections for fiber attenuation, long energy leakage and incident angle are applied.

PbSc has another important feature, which is very helpful in the measurement, that distinguishes electromagnetic clusters from hadronic clusters by comparing those shower

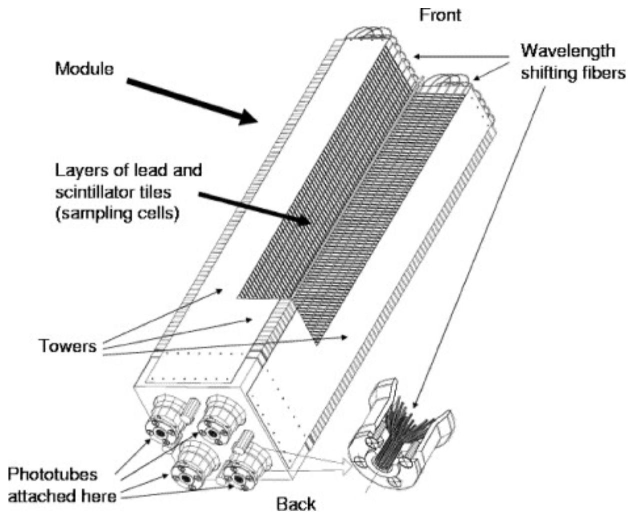

Figure 3.6: Structure of PbSc tower. [36]

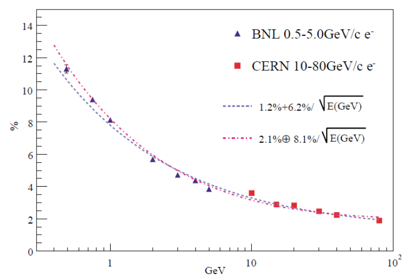

Figure 3.7: Energy resolution of PbSc obtained by beam tests at BNL and CERN. [36]

shapes. To do this, $\chi^2 = \sum_i (E_i^{pred} - E_i^{meas})^2/\sigma_i^2$ is defined to characterize how "electromagnetic" a particular shower is where E_i^{meas} is the energy measured in tower i, and E_i^{pred} is the predicted energy measured in tower i by identified electron beam. Because the interaction mechanisms between electromagnetic clusters and hadronic clusters are so different that the χ^2 distributions of the clusters are different. Fig. 3.8 shows the distributions. By the distribution, hadronic clusters can be distinguished.

3.4.2 PbGl

Two sectors (in the east arm) are comprised of PbGl. Each sector contains 48×96 towers and covers $|\eta| < 0.35$ in rapidity and $\phi = 22.5°$. The sectors are located $r = 5.2m$ radially. Each tower covers 4×4 cm^2 and consists of homogeneous 40 cm lead glass Cherenkov radiator. This corresponds 14.4 $L_{rad}(= 2.8cm)$ or 1.1 $\lambda_I(= 38cm)$. Fig. 3.9 shows structure of PbGl tower.

PbSc was calibrated using test beam. From the test beam result, the energy resolution

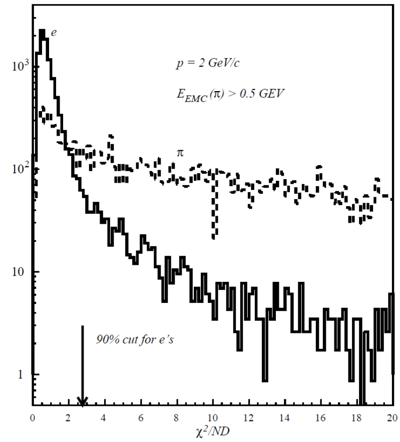

Figure 3.8: χ^2 distribution for showers induced by 2 GeV/c electrons and pions in PbSc. [36]

of PbSc is

$$\frac{\sigma_E}{E} = \frac{5.9\%}{\sqrt{E(GeV)}} \oplus 0.8\% \tag{3.4}$$

as Fig. 3.10. The position of PbGl is

$$\sigma_x(E) = \frac{8.4mm}{\sqrt{E(GeV)}} \oplus 2mm \tag{3.5}$$

Energy corrections for incident angle and non linearity are applied.

Like PbSc, PbGl can distinguish electromagnetic clusters from hadronic clusters by comparing momentum and deposited energy of the clusters. Photons or electrons deposit most of their energy on PbGl. However hadrons deposit only small fraction of their energy as left panel of Fig. 3.11. Thus hadronic clusters can be rejected by comparing momentum and deposited energy. Momentum is reconstructed by DC and PC as discussed in Subsec. 3.2.2 and Subsec. 3.2.3. The right panel of Fig. 3.11 shows rejection factor of charged pion.

3.4.3 Tower-by-Tower Global Energy Calibration

With whole data taken in Run, EMCal tower-by-tower calibration was done using π^0 mass peak. [37], [38] The towers which fail to be calibrated are excluded in the analysis. The failed towers are list in Subsubsec. 5.3.2

3.4.4 Run-by-Run and Sector-by-Sector Energy Calibration

Since the calibration described in Subsec. 3.4.3 covered the entire Run12 and Run13 for each tower in order to have enough statistics, run-by-run gain shift of EMCal is observed

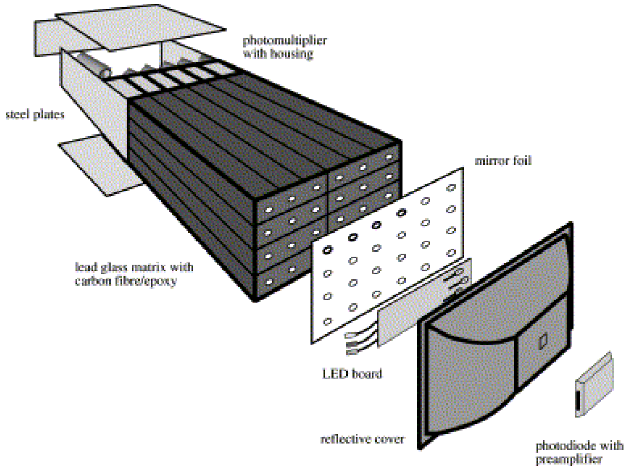

Figure 3.9: Structure of PbGl tower. [36]

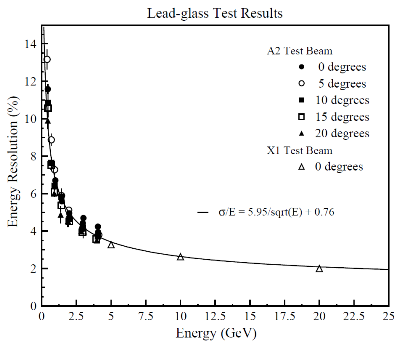

Figure 3.10: Energy resolution of PbGl obtained by beam tests at BNL and CERN. [36]

as Fig. 3.13 and Fig. 3.14 show it. Thus an additional run-by-run calibration is done for each EMCal sector for this analysis.

Cluster energies from a given sector are multiplied by "137 MeV divided by the π^0 measured peak position". To obtain the measured π^0 peak position, Voigt function + third order polynomial function are fit on run-by-run and sector-by-sector diphoton invariant mass spectrum. Fig. 3.12 shows the fitting result of example run.

The other motivation of the calibration is EMCal QA. If diphoton invariant mass spectrum of any run and any sector is abnormal and the fitting is failed, the run and sector is excluded in the analysis. If $\chi^2/NDF > 3$, the corresponding sector is marked as abnormal.

3.4.5 EMCal Tower-by-Tower ToF Calibration

ToF of the EMCal tower is calibrated to move the ToF peak of photons to $t = 0$. Before calibration, ToF measured by each tower was not aligned. The misalignment depends on

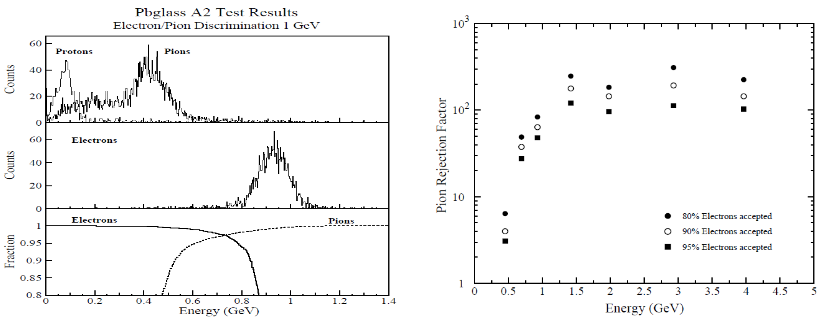

(a) Deposited Energy Fraction on PbGl (b) Charged Pion Rejection Factor

Figure 3.11: Energy resolution of PbGl obtained by beam tests at BNL and CERN. [36]

time also. Fill-by-fill calibration has been done to get enough statistics.

ToF of EMCal cluster is

$$\mathrm{ToF}^{\mathrm{uncalibrated}}_{\mathrm{EMCal\ cluster}} = \mathrm{ToF\ measured\ by\ EMCal} - \mathrm{BBC\ T_0}. \tag{3.6}$$

Because ToF measured by each EMCal tower was not aligned, we need to give tower-by-tower calibration constant to move the ToF peak of photons to $t = 0$.

$$\begin{aligned}\mathrm{ToF}^{\mathrm{calibrated}}_{\mathrm{EMCal\ cluster}} =& \mathrm{ToF\ measured\ by\ EMCal} - \mathrm{BBC\ T_0} \\ & - \mathrm{Calibration\ Constant\ of\ each\ EMCal\ Tower}\end{aligned} \tag{3.7}$$

To find the calibration constant, ToF distribution is drawn and offsets of photon peak is obtained for each tower. Fig. 3.15 is ToF distribution of single tower before calibration. The peak is shifted. The peak is fit with Gaussian and the offset is obtained. Then by subtracting the offset, the peak is moved to $t = 0$. The procedure has been done for all EMCal towers.

The procedure has been done fill-by-fill also because the tower-by-tower offsets of ToF depends on time also as Fig. 3.17. To get enough statistics, the procedure has been done fill-by-fill not run-by-run. The result of the calibration is shown in Fig. 3.16

3.5 Local Polarimeters

Local Polarimeter (Local Pol) consists of ZDCs and Shower Max Detectors. As discussed in Sec. 2.2.4, transverse component of polarization may remain after Spin Rotator. Local Pol measures and monitors the remaining component of the incident proton beam by measuring the "observed" transverse single asymmetry (ε_N) of neutrons. [39]

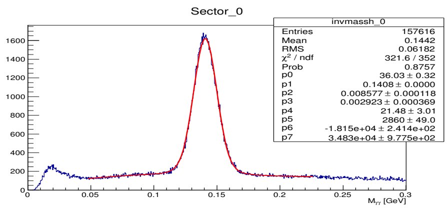

(a) Sector 0

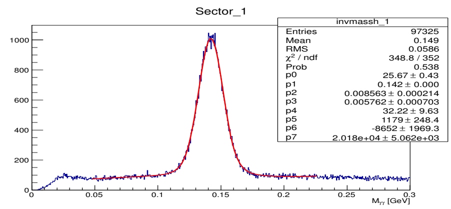

(b) Sector 1

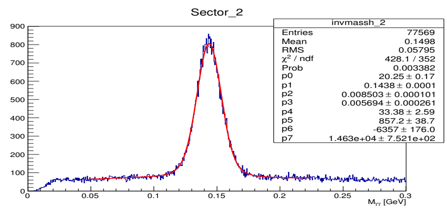

(c) Sector 2

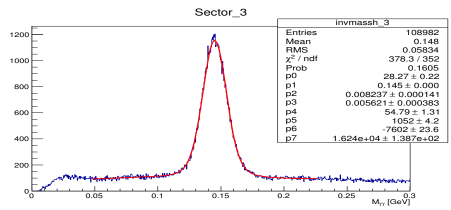

(d) Sector 3

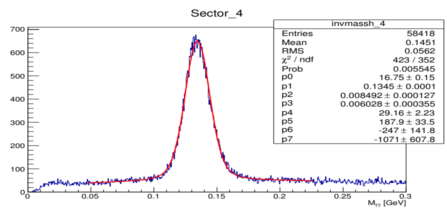

(e) Sector 4

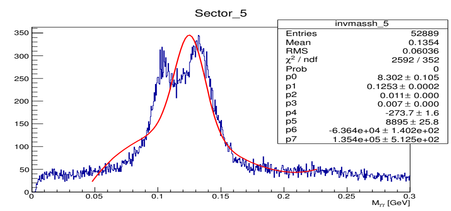

(f) Sector 5

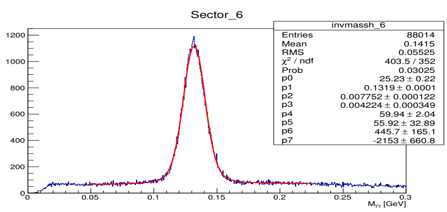

(g) Sector 6

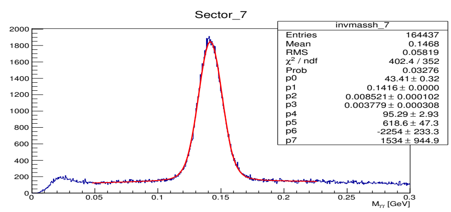

(h) Sector 7

Figure 3.12: Fitting result of runnumber 396767 for energy calibration. Parameter P1 is the measured π^0 peak position. For sector 5, the spectrum is abnormal and fitting was failed. The sector 5 of the run 396767 is excluded in the analysis.

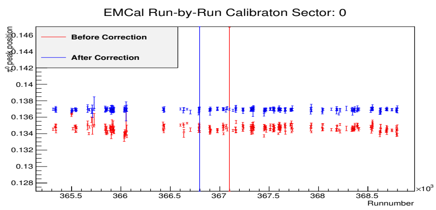

(a) Sector 0

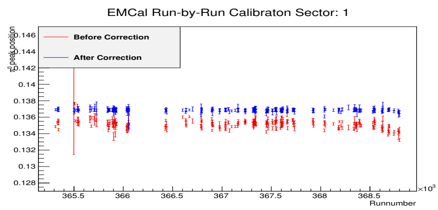

(b) Sector 1

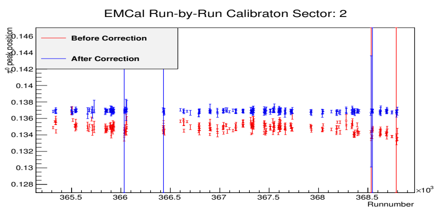

(c) Sector 2

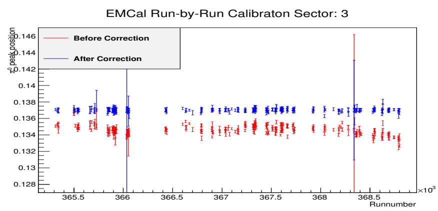

(d) Sector 3

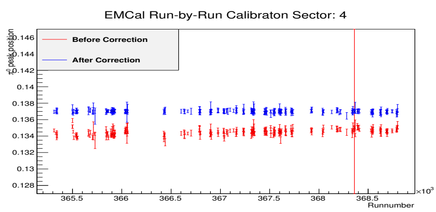

(e) Sector 4

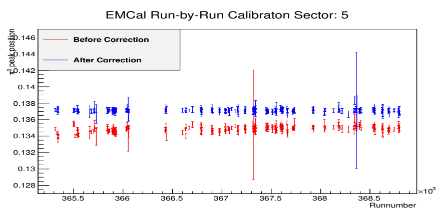

(f) Sector 5

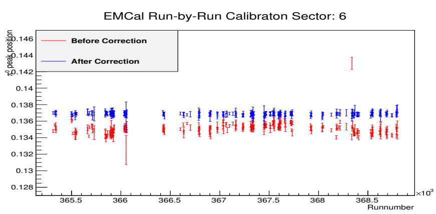

(g) Sector 6

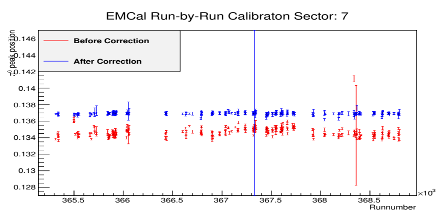

(h) Sector 7

Figure 3.13: Run12 Run-by-Run Energy Calibration. Red Points are π^0 peak position before the correction and the blue points are the position after the correction.

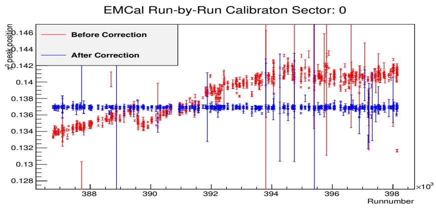

(a) Sector 0

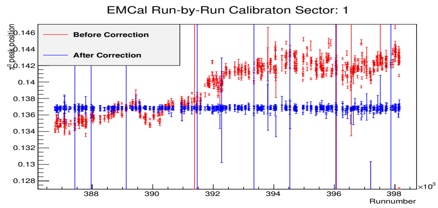

(b) Sector 1

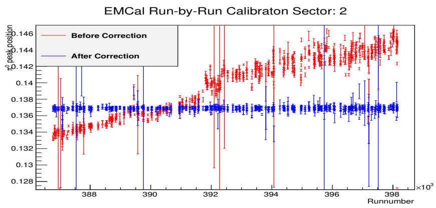

(c) Sector 2

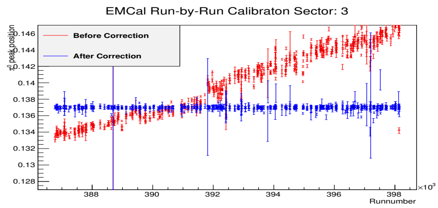

(d) Sector 3

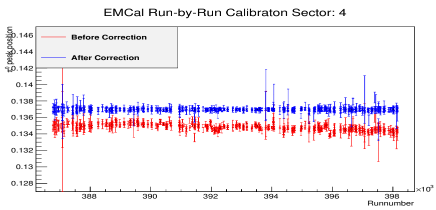

(e) Sector 4

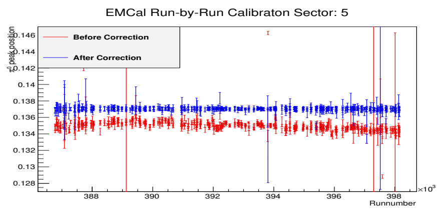

(f) Sector 5

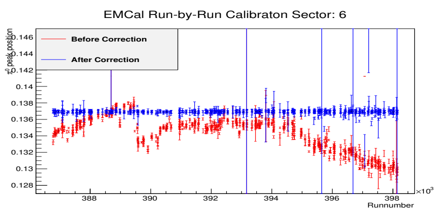

(g) Sector 6

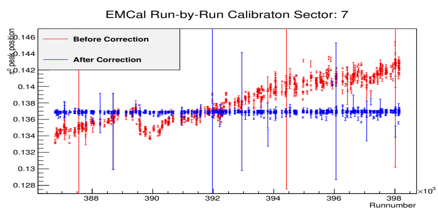

(h) Sector 7

Figure 3.14: Run13 Run-by-Run Energy Calibration. Red Points are π^0 peak position before the correction and the blue points are the position after the correction.

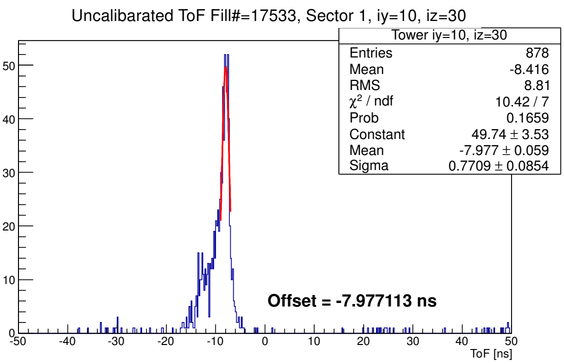

Figure 3.15: ToF distribution of single tower before calibration. The peak isn't on $t = 0$. The distribution is fit with Gaussian function and the offset of ToF is obtained.

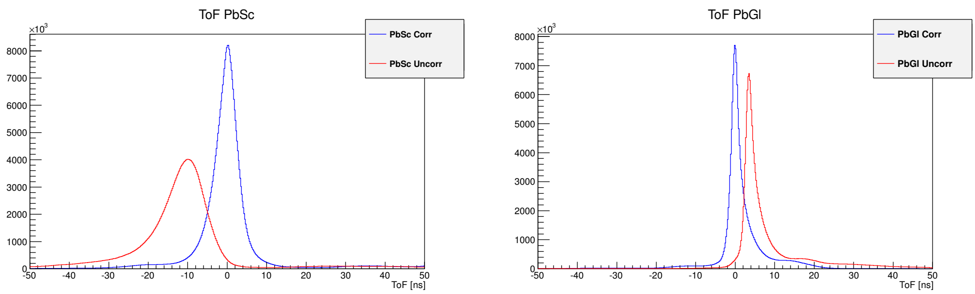

(a) PbSc

(b) PbGl

Figure 3.16: Result of ToF calibration. ToF of photon candidate before and after ToF calibration.

3.5.1 Shower Max Detectors

Shower Max Detectors (SMD) are position sensitive x-y scintillator strip hodoscopes insert between first and second ZDC modules where the hadronic shower is maximized approximately. SMD is segmented as 7 strips with 15mm width in horizontally and 8 strips 20mm width in vertically. SMD is tilted by 45° and active area of SMD is 105mm×110mm (horizontal×vertical). SMD measures position of shower from neutron. With the position information, ε_N is measured.

3.5.2 Beam direction Result

PHENIX runs with the spin rotator magnet off (transverse running) for some time to measure A_N. Then, when the rotators are turned on for longitudinal running, the remaining

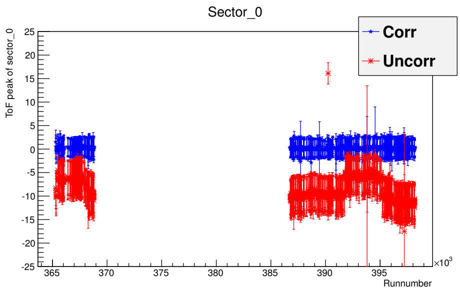

(a) Sector 0

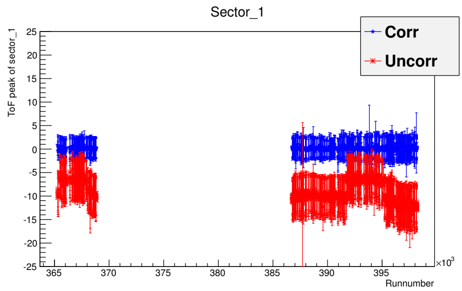

(b) Sector 1

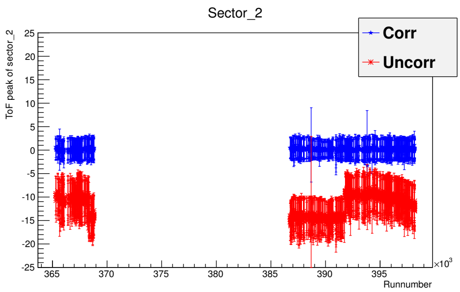

(c) Sector 2

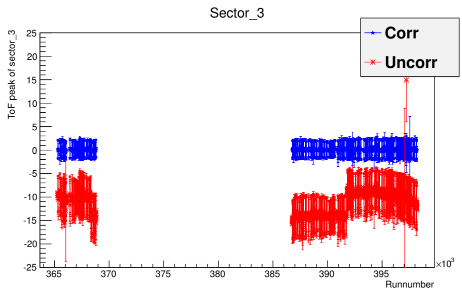

(d) Sector 3

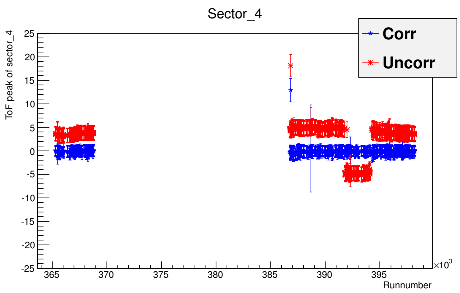

(e) Sector 4

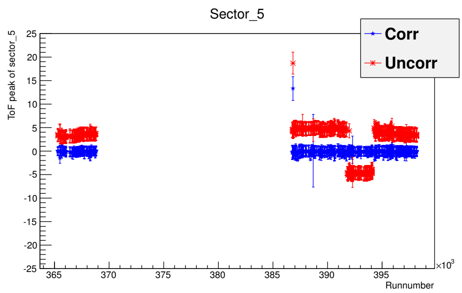

(f) Sector 5

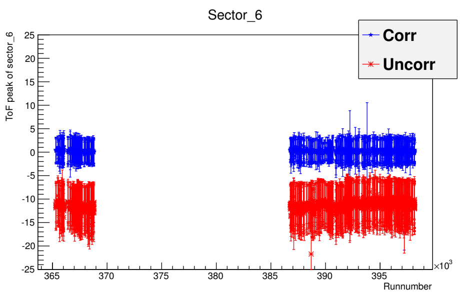

(g) Sector 6

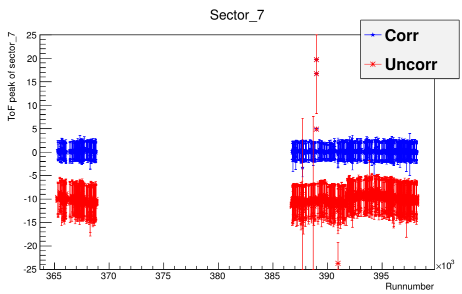

(h) Sector 7

Figure 3.17: Peak and width of ToF distribution vs runnumber for sectors before and after calibration. Error bar means FWHM of ToF distribution. Before correction, peaks are shifted from $t = 0$ and the shift depend on time also. After calibration, the shift are vanished and FWHMs become narrower.

component ratio, f_T of each beam can be measured as

$$f_T \equiv \frac{P_T}{P} = \frac{\varepsilon_{N,\text{ rotators on}}}{\varepsilon_{N,\text{ rotators off}}} \tag{3.8}$$

and the corresponding longitudinal component ratio, f_L is given by

$$f_L \equiv \frac{P_L}{P} = \sqrt{1-(\frac{P_T}{P})^2}. \tag{3.9}$$

For Run12, no offline result is available yet. However online result is available and similar result is expected in offline analysis.

- $f_L^B = 0.998$ for the blue beam
- $f_L^Y = 0.997$ for the yellow beam

Given these numbers, scale factor on final Run12 $A_{LL}^{\pi^0}$ is 1.005.

For Run13, the measurements came out to

- $f_L^B = 0.9999^{+0.0001}_{-0.0001}(stat.)^{+0.0000}_{-0.0001}(syst.)$ for the blue beam
- $f_L^Y = 0.9989^{+0.0004}_{-0.0005}(stat.)^{+0.0003}_{-0.0001}(syst.)$ for the yellow beam [40]

Given these numbers, scale factor on our Run13 $A_{LL}^{\pi^0}$ is 1.001. An additional global scaling uncertainty should be

$$\sqrt{\left(\frac{\delta f_L^B}{f_L^B}\right)^2 + \left(\frac{\delta f_L^Y}{f_L^Y}\right)^2} = \sqrt{\left(\frac{{}^{+0.0001}_{-0.001}}{0.9999}\right)^2 + \left(\frac{{}^{+0.0004}_{-0.0005}}{0.9989}\right)^2} = \frac{+0.004\%}{-0.5\%} \tag{3.10}$$

where combining of the asymmetric errors has been done by treating the + and - errors separately and assuming the systematic error is uncorrelated between the blue and yellow beam. Both values are negligibly small compared to overall polarization uncertainty.

3.6 Triggers

3.6.1 BBC Level 1 Trigger

BBC Level 1 trigger (BBCLL1) is one of main trigger of the analysis. The basic requirement of BBCLL1 is a coincidence between two BBCs. BBCLL1 has three trigger modes. The first is BBCLL1(novtx) which requires just the coincidence. The second is BBCLL1(30cm) or just BBCLL1 for simplicity which requires the coincidence and reconstructed vertex$_z$ should be in $|30cm|$ from the center of PHENIX. The third is BBCLL1(narrow) which requires the coincidence and reconstructed vertex$_z$ should be in $|15cm|$ from the center. For BBCLL1 and BBCLL1(narrow), vertex$_z$ is reconstructed by Eq. 3.1 with online resolution $\sim 5cm$.

3.6.2 ZDC Level 1 Trigger

Although ZDC Level 1 trigger (ZDCLL1) is not main trigger of the analysis, the trigger is used to estimate helicity dependence of BBCLL1. Scheme of ZDCLL1 is similar to BBCLL1. However vertex$_z$ is reconstructed by ZDC with resolution $\sim 30cm$. ZDCLL1 has two mode. The one is ZDCLL1(narrow) requires a coincidence and vertex$_z$ should be in $|30cm|$ from the center of PHENIX. The other is ZDCLL1(wide) requires a coincidence and vertex$_z$ should be in $|150cm|$ from the center.

3.6.3 EMCal RICH Trigger

EMCal RICH trigger (ERT) [41] is the other main trigger of the analysis. In order to collect rare events, such as high transverse momentum (P_T) particle creates, ERT is used. The ERT triggers on events in which large energy deposit in EMCal. If the sum of deposited energy on 2×2 or 4×4 EMCal towers is larger than the threshold, ERT triggers on the events. The EMCal towers are grouped in sets of 2×2 towers which make up a basic trigger tile. Then overlapping trigger tiles are set up to make 4×4 trigger towers with 2×2 neighboring the basic tiles. Fig. 3.18 explains it. Sets of 12×12 towers are grouped into supermodules, which are used in the trigger logic for event triggering. Supermodules are the smallest triggering unit written in output data.

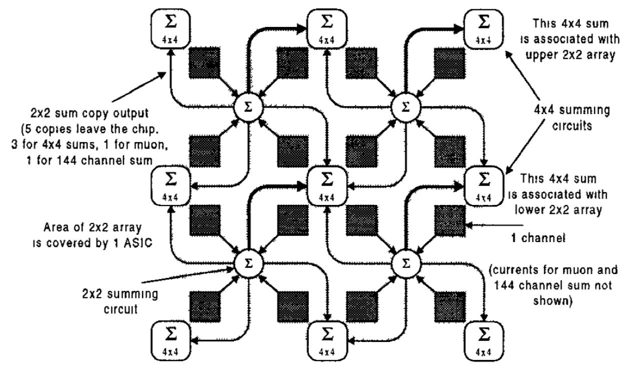

Figure 3.18: ERT scheme. If the sum of deposited energy on 4×4 EMCal towers is larger than the threshold, ERT triggers on the event. [41]

ERT has four trigger modes; triggering with 2×2 towers or 4×4 towers with three different threshold. Those are called ERT_2x2, ERT_4x4A, ERT_4x4B, and ERT_4x4C. Thresholds are roughly 0.8 GeV for ERT_2x2, 4.7 GeV for ERT_4x4A, 5.6 GeV for ERT_4x4B and 3.7 GeV for ERT_4x4C.

Crossing Dependence of ERT

ERT has two identical and alternating circuits for odd and even crossings as Fig. 3.19. ERT circuit needs 140 ns to be reset but bunch space of RHIC is 106 ns. In order to ERT can support all the bunchs, ERT has the two alternating circuits. However it causes slight difference of trigger efficiency. Thus data from even and odd crossings are analyzed separately.

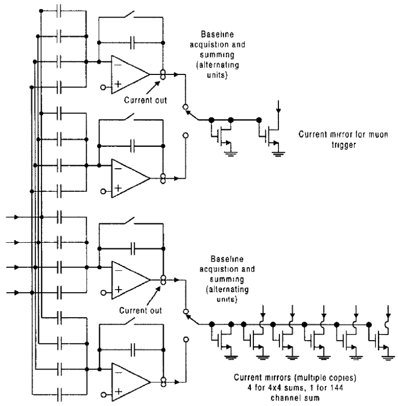

Figure 3.19: Part of ERT Circuit. There are identical and alternating summing amplifiers works for even and odd crossing, respectively. [41]

3.7 PHENIX Data Acquisition System and Prescale

For $p+p$ collision, maximum record rate of PHENIX Data Acquisition System (DAQ) [42] is 7 kHz. However as RHIC luminosity has been upgraded, trigger rate of BBCLL1 is over 2 MHz at beginning of new fill. Thus most triggers were prescaled, i.e., only every ith events are recorded. By adjusting prescale of each trigger, bandwidth of DAQ is allocated for each trigger. Each operated DAQ period is identified by so called “runnumber”. Usually each run lasts 1-1.5 hours. As luminosity decays as the fill lasts, the prescales are adjusted for each run.

3.8 Scaler Boards

To measure luminosity as precise as possible, large statistics are needed. However triggers for luminosity detectors i.e., BBCLL1 and ZDCLL1 are heavily prescaled and statistics are degraded. In order to avoid the prescale problem, PHENIX has two scaler boards. The scaler boards record total number triggers counts per crossings while DAQ is live. The one scaler board is GL1p scaler and the other is Star star.

3.8.1 GL1p Scaler

GL1p [42] has four input slots. For Run12 and Run13, the slots were assigned to BBCLL1(narrow), BBCLL1, ZDCLL1(narrow), and ZDCLL1(wide).

3.8.2 Star Scaler

The role of Star scaler is similar to GL1p. However Star scaler has 17 input slots and various combination of scaler counts can be recorded. With the combinations of scaler, Star scaler facilitates applying corrections on scaler counts can be applied as discussed in Sec. 6.4, 6.5, and 6.6.

Chapter 4

Overview of the Measurement

4.1 Measuring the A_{LL}

A cross section can be written as

$$\sigma = \frac{N^{corr}}{L} \tag{4.1}$$

where N_{corr} is the measured yield (N) corrected for efficiencies such as reconstruction (ε^{reco}), trigger bias (ε^{trig}) and detector acceptance (ε^{accep})

$$N^{corr} = \frac{N}{\varepsilon^{reco}\varepsilon^{trig}\varepsilon^{accep}} \tag{4.2}$$

and L is luminosity. Thus Eq. 1.20 can be written as

$$A_{LL} = \frac{\frac{\frac{N_{++}}{\varepsilon^{reco}_{++}\varepsilon^{trig}_{++}\varepsilon^{accep}_{++}}}{L_{++}} - \frac{\frac{N_{+-}}{\varepsilon^{reco}_{+-}\varepsilon^{trig}_{+-}\varepsilon^{accep}_{+-}}}{L_{+-}}}{\frac{\frac{N_{++}}{\varepsilon^{reco}_{++}\varepsilon^{trig}_{++}\varepsilon^{accep}_{++}}}{L_{++}} + \frac{\frac{N_{+-}}{\varepsilon^{reco}_{+-}\varepsilon^{trig}_{+-}\varepsilon^{accep}_{+-}}}{L_{+-}}} \tag{4.3}$$

True virtue of RHIC and A_{LL} measurement is we can safely assume that the efficiencies are same for proton helicity configurations. As discussed in Sec. 2.1, RHIC can accelerate bunchs of protons with different helicity with very short time spacing ($106ns$). Further more, no systematic differences such as collision vertex distribution between proton helicity configurations have been observed. Thus the efficiencies are assumed to be independent for proton helicity configurations safely and are canceled.

Polarization of both beams P_B and P_Y should be considered also. Raw asymmetry should be normalized by P_B and P_Y. Then Eq. 4.3 can be written as

$$\begin{aligned} A_{LL} &= \frac{1}{P_B P_Y} \frac{\frac{N_{++}}{L_{++}} - \frac{N_{+-}}{L_{+-}}}{\frac{N_{++}}{L_{++}} + \frac{N_{+-}}{L_{+-}}} \\ &= \frac{1}{P_B P_Y} \frac{N_{++} - RN_{+-}}{N_{++} - RN_{+-}} \end{aligned} \tag{4.4}$$

by introducing relative luminosity $R = \frac{L_{++}}{L_{+-}}$.

Thus we need to measure the helicity dependent particle yields, the relative luminosity and the beam polarizations to measure A_{LL}. In this measurement, the helicity dependent particle yields are the di-photon yields from a fixed range in the di-photon invariant mass spectrum and are discussed in Chap. 5. The relative luminosity is discussed in Chap. 6. The beam polarization is discussed in 2.2.3.

4.2 Background Subtraction

To measure $A_{LL}^{\pi^0}$, the yield in three different regions are used. The "peak" or "signal" region is defined as 137 MeV $\pm$ 25 MeV (112-162 MeV), which is roughly the mass peak $\pm \sim 2\sigma$. (shown in red in Fig. 4.1) The "side" or "background" region is defined as 47 MeV/$c^2 < M_{\gamma\gamma} <$ 97 MeV/c^2 and 177 MeV/$c^2 < M_{\gamma\gamma} <$ 227 MeV/c^2. (shown blue in Fig. 4.1) The "peak" region yield contains not only π^0 (N_{π^0}) but also background ($N_{BG.}$) counts, since the two can not be distinguished. Thus from the signal region, $A_{LL}^{\pi^0+BG}$ is measured. To remove the background contribution, A_{LL}^{BG} is needed to be measured, also. Then we can correct to $A_{LL}^{\pi^0}$ by realizing that

$$A_{LL}^{\pi^0+BG} = (1-r)A_{LL}^{\pi^0} + rA_{LL}^{BG}. \tag{4.5}$$

Eq. 4.5 can be solved for $A_{LL}^{\pi^0}$.

$$A_{LL}^{\pi^0} = \frac{A_{LL}^{\pi^0+BG} - rA_{LL}^{BG}}{1-r}, \qquad \sigma_{A_{LL}^{\pi^0}} = \frac{\sqrt{\sigma^2_{A_{LL}^{\pi^0+BG}} + r^2\sigma^2_{A_{LL}^{BG}}}}{1-r} \tag{4.6}$$

where the quantity r is the background fraction in "peak" region. It is estimated by Gaussian process for regression on the mass spectrum. Detail of the estimation is discussed in Subsec. 7.1.5

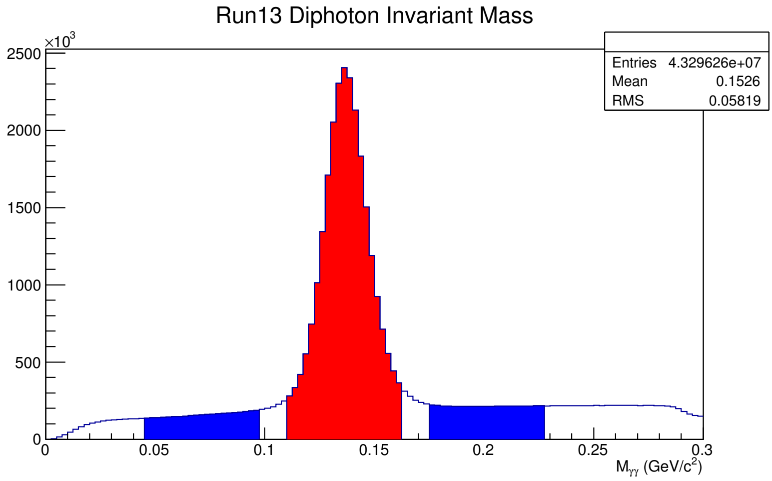

Figure 4.1: Di-photon invariant mass distribution. Red area, 112 MeV/c^2 $< M_{\gamma\gamma} <$ 162 MeV/c^2, is used for π^0 plus background asymmetry measurements ($A_{LL}^{\pi^0+BG}$). Blue area, 47 MeV/c^2 $< M_{\gamma\gamma} <$ 97 MeV/c^2 and 177 MeV/c^2 $< M_{\gamma\gamma} <$ 227 MeV/c^2, is used for background asymmetry measurements (A_{LL}^{BG}).

Chapter 5

Data Selection, π^0 Reconstruction and Background Reduction

5.1 Run QA

The data sample analyzed covers $\sqrt{s} = 510$ GeV longitudinal $p + p$ running from run 364822 (2012, Mar., 20) through run 368798 (2012, Apr., 18) (Run12) and run 386773 (2013, Mar., 10) through 398149 (2013, Jun., 10) (Run13). 311 (Run12) and 1008 (Run13) physics runs are available. To assure quality of data, intensive QA is applied. 227 runs (Run12) and 780 runs (Run13) have passed the QA and been analyzed. It corresponds to 19.93 pb^{-1} for Run12 and 108.1 pb^{-1} for Run13. The followings are conditions for the QA.

5.1.1 DAQ Condition

Two conditions for DAQ are required for "good" runs. First condition is DAQ time. Runs shorter than 10 mins are rejected because short run might mean something strange on DAQ happened and the run was terminated early. Second condition is livetime of BBCLL1, ERT_4x4A, ERT_4x4B, and ERT_4x4C should be larger than 0.5. If livetime of any trigger is lower than 0.5, the run is rejected.

5.1.2 Spin Database

When DAQ is operated, spin pattern and beam polarization are automatically recorded in PHENIX database. After Run12 and Run13 ends, intensive quality assurance has been done to check spin pattern and beam polarization are properly recorded. [43], [44] Runs which pass the QA are analyzed.

5.1.3 Polarization

Minimum 10% polarization on both of beams are applied.

5.1.4 GL1p Scaler and Star Scaler Agreement

In this analysis Star scaler is used basically. However to assure reliability of Star scaler, GL1p scaler is used also to compare with Star Scaler. To compare Star scaler and GL1p scaler, crossing-by-crossing ratio of GL1p scaler counts to Star scaler counts is drawn and constant fitting is done on the ratios. If value of fitted constant is larger than 1.002 or smaller than 0.998 or χ^2_{re} of the fitting is larger than 2.5×10^3, the runs are rejected.

5.1.5 EMCal Condition

QA on EMCal is covered by run-by-run and sector-by-sector EMCal energy calibration as discussed in Subsec. 3.4.4.

5.2 Event Selection

5.2.1 Trigger Requirement

To maximize statistics, ERT "OR" trigger is used. ERT "OR" trigger is logical combination of ERT_4x4A, ERT_4x4B, and ERT_4x4C. To be more specific, any events which fired ERT_4x4a&BBCLL1, ERT_4x4b, or E RT_4x4c&BBCLL1(narrow) are analyzed for Run12. For Run13, any events which fired ERT_4x4a&BBCLL1(novtx), ERT_4x4b, or ERT_4x4c&BBCLL1(novtx) are analyzed.

From now on, let's denote ERT_4x4a&BBCLL1 and ERT_4x4a&BBCLL1(novtx) as ERT_4x4A and ERT_4x4c&BBCLL1(narrow) and ERT_4x4c&BBCLL1(novtx) as ERT_-4x4C for simplicity.

5.2.2 Vertex$_\mathrm{z}$ Requirement

Events which vertex$_\mathrm{z}$ within 30cm from the center of PHENIX are analyzed. As discussed in Subsec. 3.2.1, frame of magnet sits at $\pm 40cm$ and events which vertex$_\mathrm{z}$ are out of $\pm 30cm$ are hindered by the frame.

5.3 π^0 Reconstruction

5.3.1 Trigger Requirement

As triggered data is being analyzed, it is necessary to assure every π^0 has same trigger bias. In other words, it is necessary to reject π^0s in $p+p\to\pi^0+C+X$ events where C is some other particle and C fires the trigger. Unless inclusive $C+\pi^0$ production has the same asymmetry as inclusive π^0 production, counting such events would pollute the asymmetry measurement. We should require that the π^0 itself triggered the events, but in practice the weaker requirement is applied; the ERT supermodule containing the central tower of the higher energy cluster in each pair should have the ERT "OR" trigger bit set. Thus the higher energy cluster is called as "triggered" cluster and the other cluster is called as "paired" cluster.

5.3.2 Photon Identification

The numerous cuts are applied to photon identification. The final uncertainty on $A_{LL}^{\pi^0}$ depends on the percentage of background under the π^0 peak (r in Eq. 4.6). To reduce statistical uncertainty in final result, background contamination is necessary. Since π^0s are reconstructed by γ pairs, the photon identification is done.

Rejecting Noise Hits: Minimum Energy Cut

A minimum energy cut is applied to all clusters to reduce combinatorial background from low energy clusters which are heavily contaminated with noise hits. In previous measurements such as π^0 cross section and A_{LL} at lower collision energy, clusters with energy below 0.1 (0.2) GeV in PbSc (PbGl) were rejected. However, clusters with energy below 0.3 GeV in both detector are discarded due to increased collision energy in the measurement.

Rejecting Noise Hits: Warn Map

Noisy and dead towers, as well as towers with failed energy calibration (see Subsubsec. 3.4.3), are excluded from this analysis. Towers which are neighboring the excluded tower are also excluded, in order to prevent a cluster centered on a good tower but extending into a bad tower from being analyzed. Because a typical photon shower is not more than three towers in diameter, only direct neighbor towers are excluded. Procedures for determining noisy and dead tower are described in App. A. Tab. 5.1 and Tab. 5.2 are summary table of rejected towers. Fig. 5.1 and 5.2 are summary plots for warnmap.

sector	masked non-edge towers	masked edge towers	total towers
W0	15 (1%)	416 (16%)	2592
W1	42 (2%)	416 (16%)	2592
W2	55 (2%)	416 (16%)	2592
W3	61 (2%)	416 (16%)	2592
E0	57 (1%)	560 (12%)	4608
E1	43 (1%)	560 (12%)	4608
E2	84 (3%)	416 (16%)	2592
E3	28 (1%)	416 (16%)	2592
PbSc	285 (2%)	2496 (16%)	15552
PbGl	100 (1%)	1120 (12%)	9216
Total	385 (2%)	3616 (15%)	24768

Table 5.1: Summary table of Run12 EMCal Warnmap. Number of nod-edge (hot, dead and uncalibrated) and edge masked towers of Run12 warnmap. The number of in parenthesis is the percentage of the total.

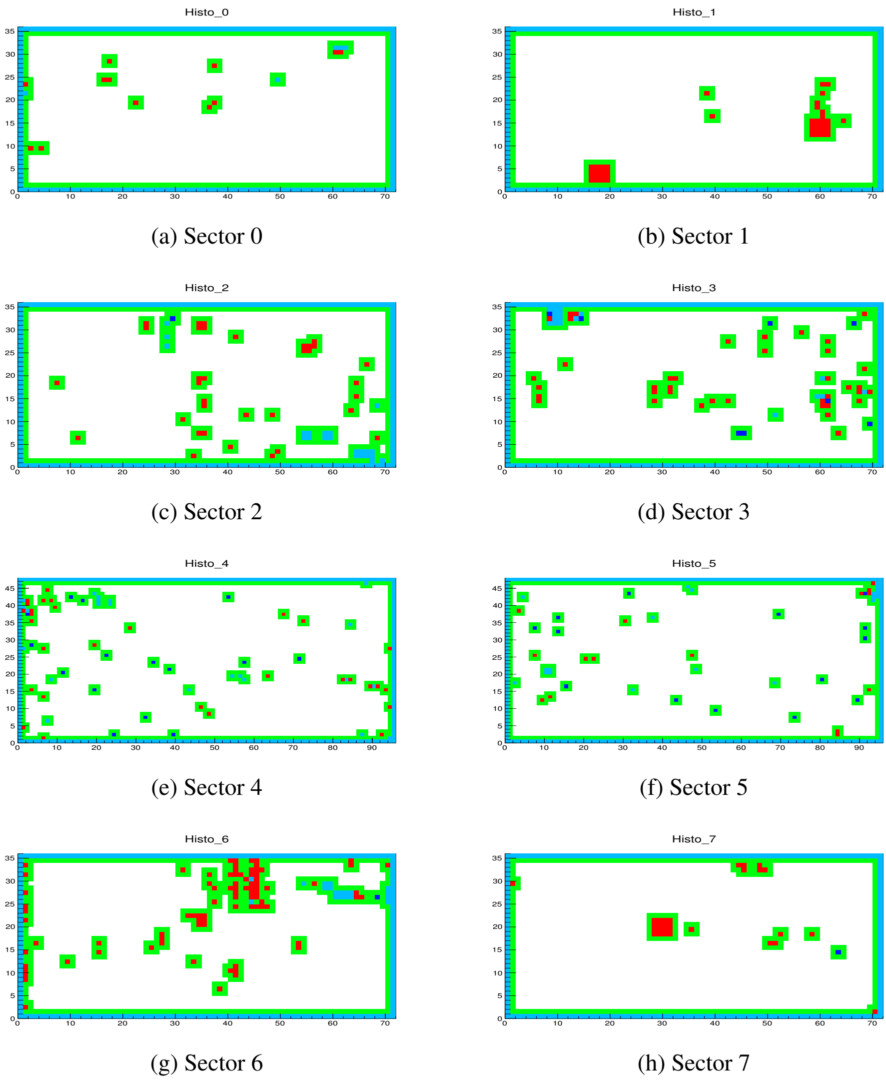

(a) Sector 0
(b) Sector 1
(c) Sector 2
(d) Sector 3
(e) Sector 4
(f) Sector 5
(g) Sector 6
(h) Sector 7

Figure 5.1: Run12 EMCal Warnmaps. Red means noisy tower, blue means dead tower, light blue means uncalibrated tower and green mean neighbor towers.

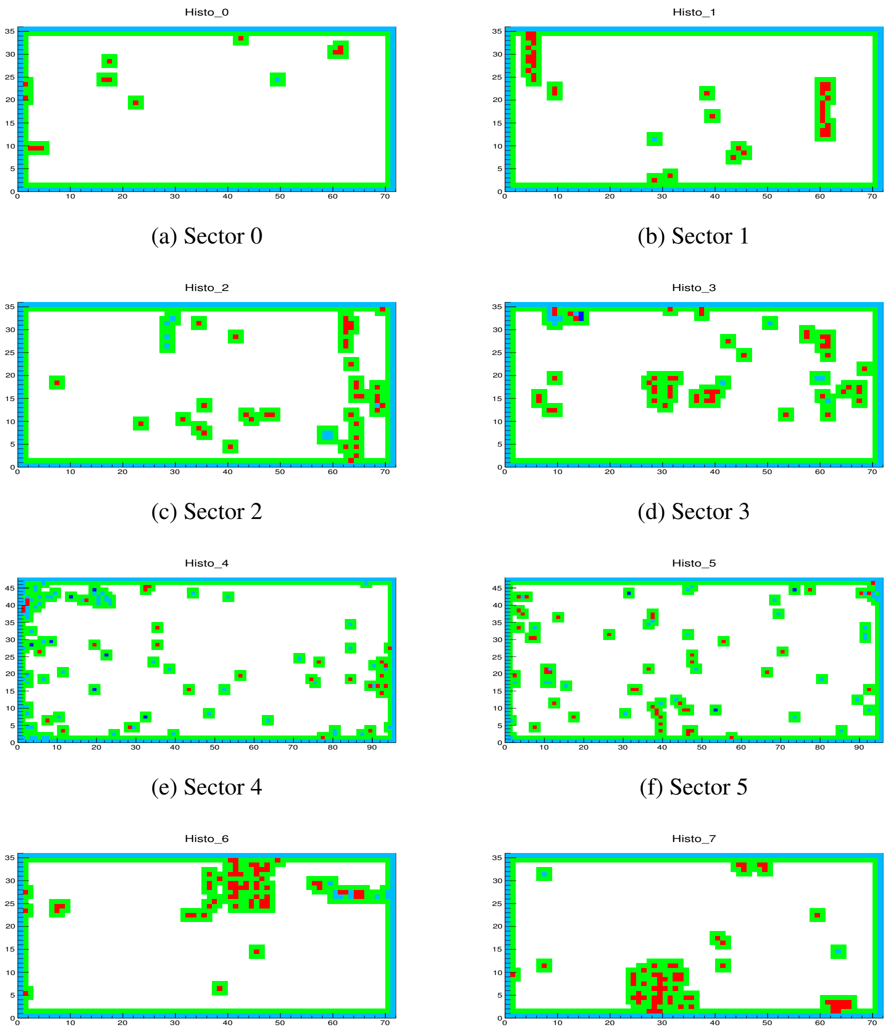

(a) Sector 0

(b) Sector 1

(c) Sector 2

(d) Sector 3

(e) Sector 4

(f) Sector 5

(g) Sector 6

(h) Sector 7

Figure 5.2: Run13 EMCal Warnmaps. Red means noisy tower, blue means dead tower, light blue means uncalibrated tower and green mean neighbor towers.

sector	masked non-edge towers	masked edge towers	total towers
W0	2 (0%)	416 (16%)	2592
W1	39 (2%)	416 (16%)	2592
W2	46 (2%)	416 (16%)	2592
W3	60 (2%)	416 (16%)	2592
E0	88 (2%)	560 (12%)	4608
E1	74 (2%)	560 (12%)	4608
E2	65 (3%)	416 (16%)	2592
E3	60 (2%)	416 (16%)	2592
PbSc	272 (2%)	2496 (16%)	15552
PbGl	162 (2%)	1120 (12%)	9216
Total	434 (2%)	3616 (15%)	24768

Table 5.2: Summary table of Run13 EMCal Warnmap. Number of nod-edge (hot, dead and uncalibrated) and edge masked towers of Run13 warnmap. The number of in parenthesis is the percentage of the total.

Rejecting Hadron: Shower Profile Cut

As discussed in Sec. 3.4, PHENIX EMCal has the ability to distinguish hadron by shower profile. For PbSc, by comparing the distribution of deposited energies on towers to the distribution obtained from electron beam, hadron can be rejected as discussed in Subsec. 3.4.1. For PbGl, by comparing measured energy and momentum, hadron can be rejected as discussed in Subsec. 3.4.2. With the ability, the confident levels to be photon are calculated for the clusters. The confident level is so called "prob_ photon". In the measurement, clusters with "prob_photon" < 0.02 are cut for both of PbSc and PbGl. That means 2% of real photons are rejected by the cut. The 2% cut is conventional value and applied in previous π^0 cross section and A_{LL} analyses also.

Rejecting Charged Particle: Charge Veto Cut

The method of reducing charged particle contamination is to apply a veto on clusters associated with charged tracks. For this, hits in the PC3 are used. Two vectors are defined. The first from the vertex$_z$ (0, 0, z_{BBC}) to the cluster position in the EMCal, and the second from the vertex$_z$ to the nearest hit in the PC3. The angle between these two vectors is defined as θ_{CV}. Fig. 5.3 shows distribution of θ_{CV}. The values of charge veto angle θ_{CV} is divided into three regions ("small", "medium", and "large"), which can be explained in following ways.

- Small θ_{CV}: e^+e^- pairs from photon conversions outside of the magnetic field region, especially in RICH, can still form a single cluster if their opening angle is small relative to the conversion's distance from the EMCal. In this case, an associated PC3 hit will be found directly in front of the cluster. The original photon can be reconstructed accurately still from the energy deposited. Thus the clusters

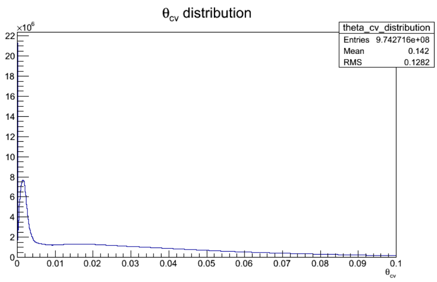

Figure 5.3: θ_{CV} distribution. For track which has no associated PC3 hit, $\theta_{CV} = 0$ is assigned.

should be retained.

- Medium θ_{CV}: For charged particles that travel through the inner magnetic field region, it is not possible to draw a straight line connecting the EMCal cluster, PC3 hit and collision vertex. Thus there will be some finite θ_{CV} associated with these particles. Such particles should be rejected.

- Large θ_{CV}: For large θ_{CV} region, accidentally associated PC3 hits are dominant.

The above situations are graphically explained again by Fig. 5.4. The validation of the scenarios by data is shown Fig. 5.6.

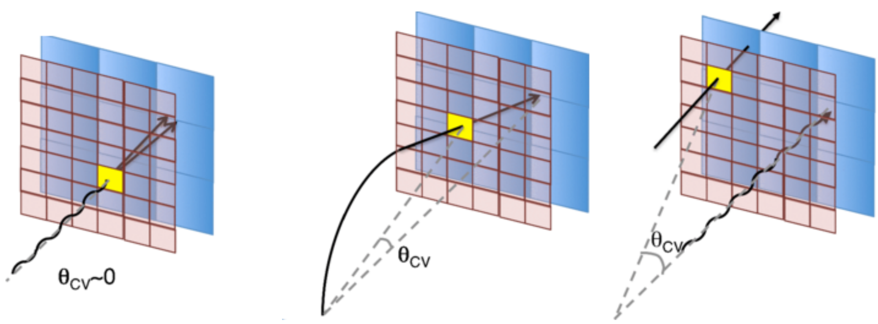

(a) "Small" θ_{CV} (b) "Medium" θ_{CV} (c) "Large" θ_{CV}

Figure 5.4: Three scenarios of behavior of θ_{CV}. [14]

By optimizing statistical uncertainty of final $A_{LL}^{\pi^0}$, rejecting regions are obtained. The following formula is used for PbSc.

$$\begin{aligned} &4.22\times10^{-4} - 1.16\times10^{-2}E_\gamma - 4.53\times10^{-3}E_\gamma^2 < \theta_{CV} \\ &\theta_{CV} < 1.01\times10^{-1} - 2.02\times10^{-1}E_\gamma + 1.51\times10^{-1}E_\gamma^2 - 3.66\times10^{-2}E_\gamma^3 \end{aligned} \tag{5.1}$$

Similarly, the following formula is used for PbGl

$$
\begin{aligned}
&1.27\times10^{-2}-2.14\times10^{-2}E_\gamma+2.26\times10^{-2}E_\gamma^2<\theta_{CV}\\
&\theta_{CV}<1.64\times10^{-2}-7.38\times10^{-3}E_\gamma+1.45\times10^{-1}e^{-4.00\times10^{0}E_\gamma}
\end{aligned}
\tag{5.2}
$$

The regions between two formulas are rejected. The following Fig. 5.5 shows rejecting region by charge veto cut for PbSc and PbGl.

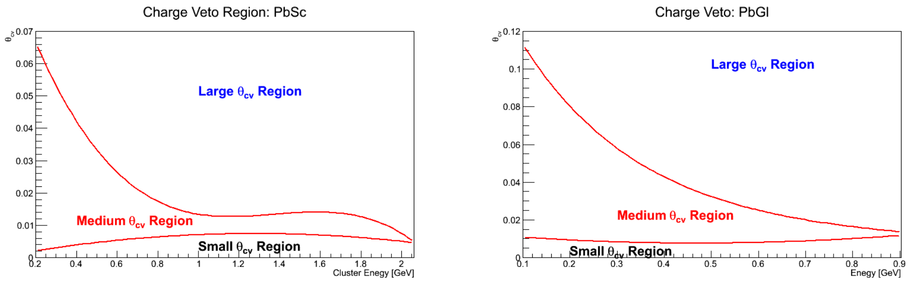

(a) Charge Veto Region: PbSc (b) Charge Veto Region: PbGl

Figure 5.5: Charge veto region for PbSc and PbGl.

Fig. 5.6 shows di-photon invariant mass distributions drawn with the three regions. As discussed above, it is clear that small θ_{CV} and large θ_{CV} regions contain π^0 decay photons. It is also obvious that medium θ_{CV} region does not contain π^0 decay photons.

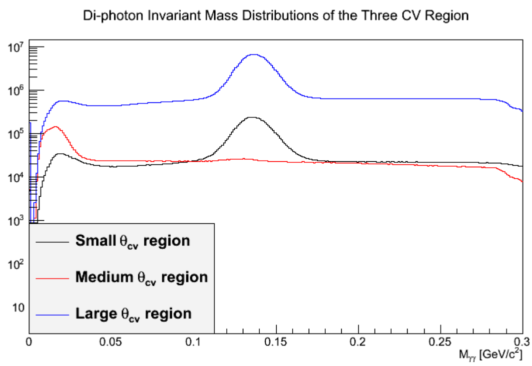

Figure 5.6: Charge veto region for PbSc and PbGl.

Rejecting Ghost Cluster: ToF Cut

Since decay time of EMCal is long, hits from previous crossing up to three crossings can remains. It is called "ghost" clusters and the ghost clusters are one of the source of combinatorial background. As discussed in Subsec. 7.2.1, the background from ghost

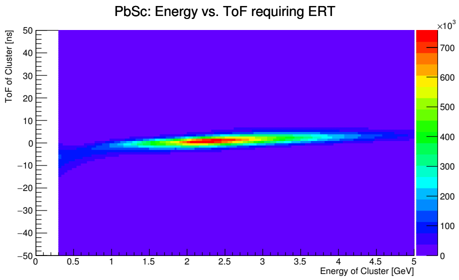

(a) PbSc, ERT on cluster is required

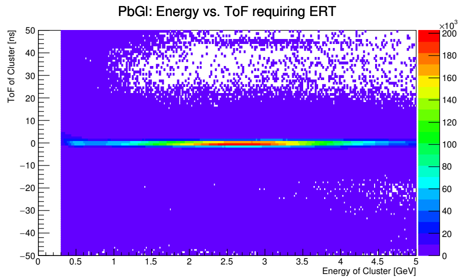

(b) PbGl, ERT on cluster is required

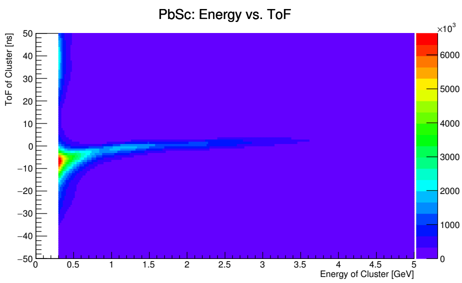

(c) PbSc, ERT on cluster is not required

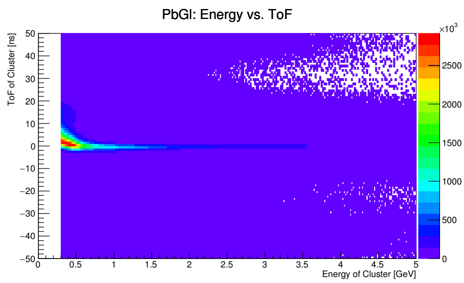

(d) PbGl, ERT on cluster is not required

Figure 5.7: Energy vs. ToF: 2D Histogram. If ERT on cluster is not required (=paired clusters), there are plenty off-ToF and low energy events.

clusters can have spin pattern dependency and make false asymmetry in low P_T. Thus the ghost clusters are rejected as much as possible.

By requiring condition on ToF of clusters, the ghost clusters can be rejected because clusters from previous crossings can not be associated with the current event's t_0 and thus they will have a wider ToF distribution. Thus by rejecting clusters which have wide ToF, the ghost clusters can be rejected.

To apply the ToF cut, EMCal Tower-by-Tower ToF Calibration is done as discussed in Subsec. 3.4.5. Clusters which have $15ns < |ToF|$ are rejected. As Fig. 5.7 shows, low energy and off-ToF clusters are plenty for paired clusters. It is highly probable that the low energy and off-ToF region is contaminated by ghost clusters. Thus ToF cut is important for the paired cluster and the condition is required for not only triggered cluster but also paired clusters.

Another importance of this cut is reducing clusters from heavy and slow hadrons.

5.3.3 π^0 Reconstruction

π^0 decays to γ pair with branching ratio 98.823% and mean life $8.52 \times 10^{-17} s$. [1] Because γ pair is most probable decay channel and γ can be measured well by PHENIX EMCal, π^0 is reconstructed by γ pair.

To reconstruct four momentum of γ, energy and hit position of γ is measured by

EMCal and vertex$_z$ is measured by BBC. With vertex$_z$ and hit position, direction cosine, $(cos\theta_x, cos\theta_y, cos\theta_z)$ is obtained. Then four momentum of γ, $P_{\gamma,\mu}$ is

$$P_{\gamma,\mu} = (E, Ecos\theta_x, Ecos\theta_y, Ecos\theta_z) \tag{5.3}$$

obtained.

By conservation of momentum, four momentum of π^0, $P_{\pi^0,\mu}$ is

$$P_{\pi^0,\mu} = P_{\gamma_1,\mu} + P_{\gamma_2,\mu} \tag{5.4}$$

The invariant mass of π^0, $m_{\gamma\gamma}$ is

$$M_{\gamma\gamma} = \sqrt{P_{\pi^0,\mu} P^{\mu}_{\pi^0}} \tag{5.5}$$

If $M_{\gamma\gamma}$ is within 112 MeV/c^2 $< M_{\gamma\gamma} <$ 162 MeV/c^2, the γ pair is considered as π^0 decay γ pair.

5.4 π^0 Final Statistics

Di-photon invariant mass spectra with cut combinations are plotted for Fig. 5.8, Fig. 5.9, Fig. 5.10 and Fig. 5.11 for P_T bins. Yields for peak and regions as regions as well as background fractions are summarized in Tab. 5.3, Tab. 5.4, Tab. 5.5 and Tab. 5.6. See Subsec. 7.1.5 how the background fractions are obtained.

$P_T(GeV)$	Spin Pat.	Peak Yield	SB Yield	Back. Frac.(%)
2.0-2.5	SOOS OSSO	691520 475156	354788 248263	28.0926
2.5-3.0	SOOS OSSO	1009330 693700	403942 285008	22.006
3.0-3.5	SOOS OSSO	1125106 785229	384658 272558	18.2168
3.5-4.0	SOOS OSSO	1053252 749469	323801 235867	15.5129
4.0-4.5	SOOS OSSO	876826 635326	250040 186375	13.9763
4.5-5.0	SOOS OSSO	668473 495464	179915 135925	13.1365
5.0-6.0	SOOS OSSO	830027 629254	205428 159129	12.8261
6.0-7.0	SOOS OSSO	410034 321225	90516 72294	12.2633
7.0-8.0	SOOS OSSO	201092 160422	40705 32760	12.1753

8.0-9.0	SOOS OSSO	99504 80076	18874 15501	11.9546
9.0-10.	SOOS OSSO	51788 41811	9540 7590	12.4493
10.-12.	SOOS OSSO	44395 36011	7611 6178	11.6355
12.-15.	SOOS OSSO	17866 14645	3037 2547	9.52434
15.-20.	SOOS OSSO	4871 3902	961 793	11.8313

Table 5.3: Run12 di-photon yields and background fractions for even crossings.

$P_T(GeV)$	Spin Pat.	Peak Yield	SB Yield	Back. Frac.(%)
2.0-2.5	SOOS OSSO	652311 442440	334507 231835	28.1292
2.5-3.0	SOOS OSSO	958882 651792	384683 266935	21.8851
3.0-3.5	SOOS OSSO	1068992 737391	364187 256758	18.2319
3.5-4.0	SOOS OSSO	1001293 707359	308431 222651	15.9431
4.0-4.5	SOOS OSSO	832907 601423	237191 176280	14.0891
4.5-5.0	SOOS OSSO	637240 468475	170978 128833	13.5786
5.0-6.0	SOOS OSSO	788563 595210	195103 150608	13.0711
6.0-7.0	SOOS OSSO	390266 303053	85762 67670	12.0512
7.0-8.0	SOOS OSSO	191375 151572	38380 30729	12.3685
8.0-9.0	SOOS OSSO	94847 75368	17881 14662	12.0212
9.0-10.	SOOS OSSO	49478 39827	9091 7162	12.4807
10.-12.	SOOS OSSO	42282 33596	7351 5889	13.1098
12.-15.	SOOS OSSO	17020 13838	2785 2464	11.7742

15.-20.	SOOS	4552	924	8.38888
	OSSO	3732	716	

Table 5.4: Run12 di-photon yields and background fractions for odd crossings.

$P_T(GeV)$	Spin Pat.	Peak Yield	SB Yield	Back. Frac.(%)
2.0-2.5	SOOSSOO	296431	133454	27.6256
	OSSOOSS	357018	159785	
	SSOO	3561801	1795840	
	OOSS	3707908	1888111	
2.5-3.0	SOOSSOO	414846	147320	20.5448
	OSSOOSS	502605	176948	
	SSOO	5546694	2115502	
	OOSS	5809845	2229894	
3.0-3.5	SOOSSOO	447018	132899	16.5302
	OSSOOSS	539953	160380	
	SSOO	6215045	1968842	
	OOSS	6544653	2086957	
3.5-4.0	SOOSSOO	388404	102092	13.9259
	OSSOOSS	462936	121591	
	SSOO	5659189	1579614	
	OOSS	5982479	1679693	
4.0-4.5	SOOSSOO	301362	72856	12.513
	OSSOOSS	356470	85530	
	SSOO	4560569	1167810	
	OOSS	4842545	1241876	
4.5-5.0	SOOSSOO	220049	50829	11.714
	OSSOOSS	258047	58877	
	SSOO	3429552	818916	
	OOSS	3637003	873264	
5.0-6.0	SOOSSOO	268595	57276	11.1675
	OSSOOSS	312192	66378	
	SSOO	4214987	927075	
	OOSS	4468989	981733	
6.0-7.0	SOOSSOO	133421	25700	10.4709
	OSSOOSS	153476	29196	
	SSOO	2097162	407445	
	OOSS	2208305	429549	
7.0-8.0	SOOSSOO	66517	11586	9.74797
	OSSOOSS	76196	13272	

	SSOO	1041814	182992	
	OOSS	1093378	190831	
8.0-9.0	SOOSSOO	33694	5529	10.3129
	OSSOOSS	37978	6084	
	SSOO	522942	85532	
	OOSS	545742	89294	
9.0-10.	SOOSSOO	17936	2708	9.62632
	OSSOOSS	20167	3049	
	SSOO	273048	42258	
	OOSS	284529	44208	
10.-12.	SOOSSOO	15383	2238	10.3288
	OSSOOSS	17282	2509	
	SSOO	234195	34620	
	OOSS	243792	35884	
12.-15.	SOOSSOO	6291	866	10.4234
	OSSOOSS	7013	1000	
	SSOO	95870	13796	
	OOSS	100091	14480	
15.-20.	SOOSSOO	1645	271	12.6666
	OSSOOSS	1865	322	
	SSOO	25539	4373	
	OOSS	26451	4638	

Table 5.5: Run13 di-photon yields and background fractions for even crossings.

$P_T(GeV)$	Spin Pat.	Peak Yield	SB Yield	Back. Frac.(%)
2.0-2.5	SOOSSOO	301911	133408	27.4186
	OSSOOSS	370996	163971	
	SSOO	3442239	1738964	
	OOSS	3616037	1836657	
2.5-3.0	SOOSSOO	411715	144410	20.6221
	OSSOOSS	505786	177585	
	SSOO	5351868	2043877	
	OOSS	5637522	2164618	
3.0-3.5	SOOSSOO	434889	128776	16.5753
	OSSOOSS	529470	157140	
	SSOO	6003952	1902906	
	OOSS	6348560	2025332	
3.5-4.0	SOOSSOO	373161	97903	13.976
	OSSOOSS	448432	118101	
	SSOO	5464919	1527769	

	OOSS	5799947	1626045	
4.0-4.5	SOOSSOO OSSOOSS SSOO OOSS	288837 344501 4405739 4690574	70142 82581 1128086 1201452	12.4801
4.5-5.0	SOOSSOO OSSOOSS SSOO OOSS	212388 249511 3312566 3525032	48757 56109 792768 844286	11.8294
5.0-6.0	SOOSSOO OSSOOSS SSOO OOSS	258098 300589 4078000 4324431	55250 63308 895940 951008	10.6497
6.0-7.0	SOOSSOO OSSOOSS SSOO OOSS	128446 146662 2024522 2137035	24911 28141 394326 416102	10.0335
7.0-8.0	SOOSSOO OSSOOSS SSOO OOSS	64316 73090 1009074 1054626	10937 12578 176731 184662	10.2934
8.0-9.0	SOOSSOO OSSOOSS SSOO OOSS	32384 36725 506375 526337	5353 5845 83229 86903	8.94846
9.0-10.	SOOSSOO OSSOOSS SSOO OOSS	17058 19158 264092 275975	2622 3028 41119 43096	10.4054
10.-12.	SOOSSOO OSSOOSS SSOO OOSS	14739 16808 226323 235332	2035 2416 33696 35158	9.44823
12.-15.	SOOSSOO OSSOOSS SSOO OOSS	6035 6778 91991 96361	839 1035 13512 13838	10.3048
15.-20.	SOOSSOO OSSOOSS SSOO OOSS	1577 1849 24749 25666	262 335 4276 4330	11.3489

Table 5.6: Run13 di-photon yields and background fractions for odd crossings.

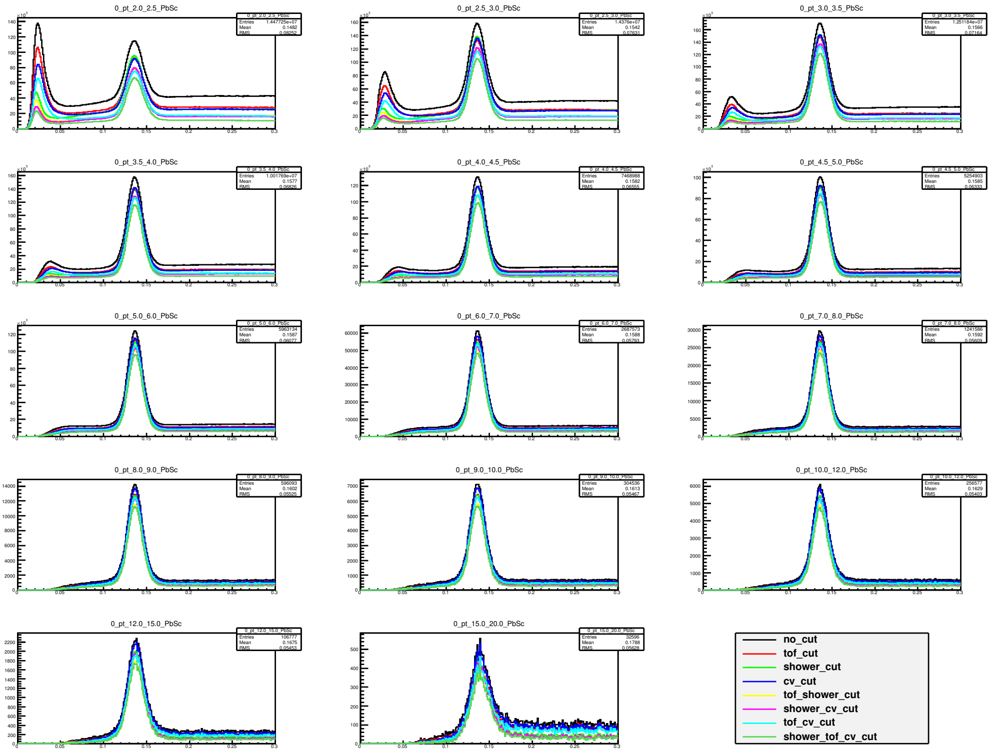

Figure 5.8: Run12 di-photon invariant mass spectra with cut combinations for PbSc for P_T bins.

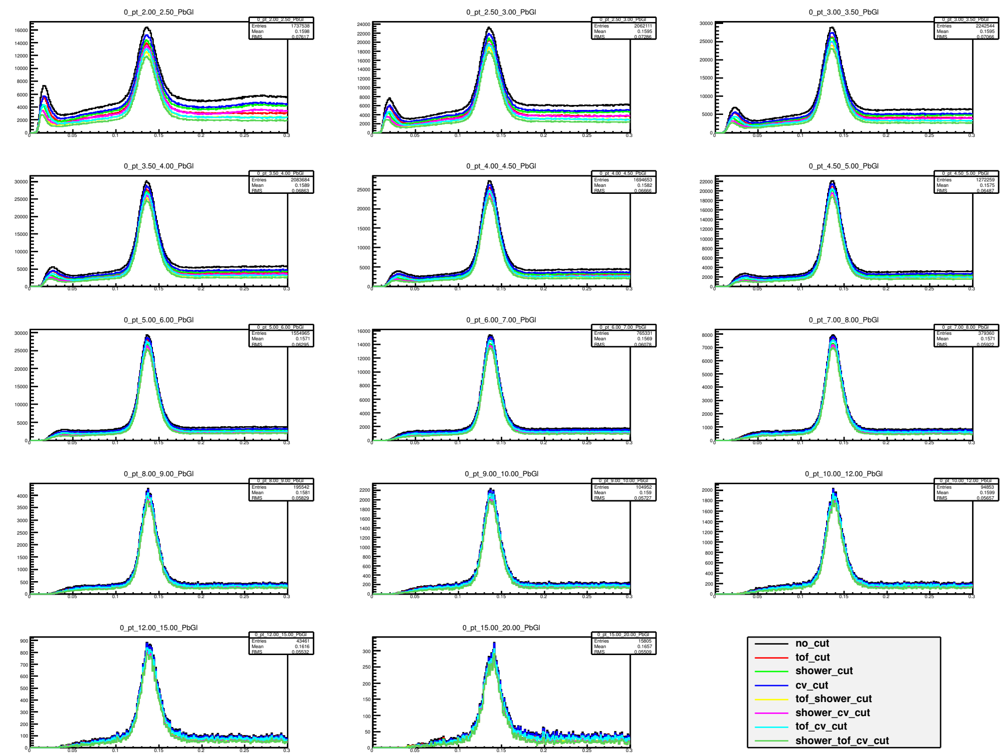

Figure 5.9: Run12 di-photon invariant mass spectra with cut combinations for PbGl for P_T bins.

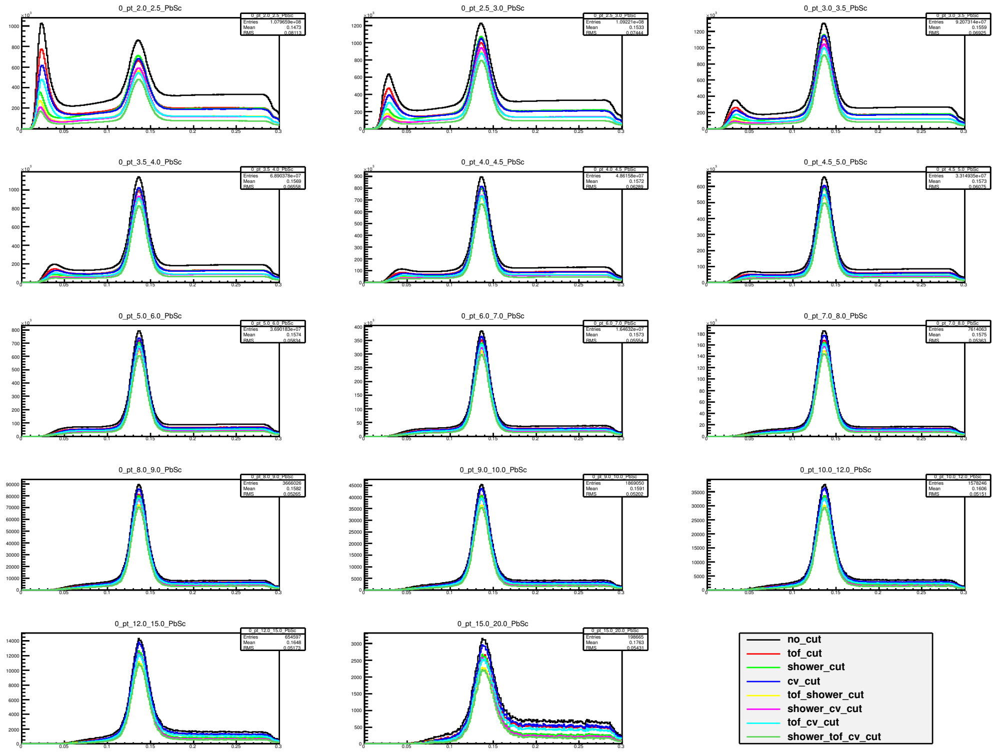

Figure 5.10: Run13 di-photon invariant mass spectra with cut combinations for PbSc for P_T bins.

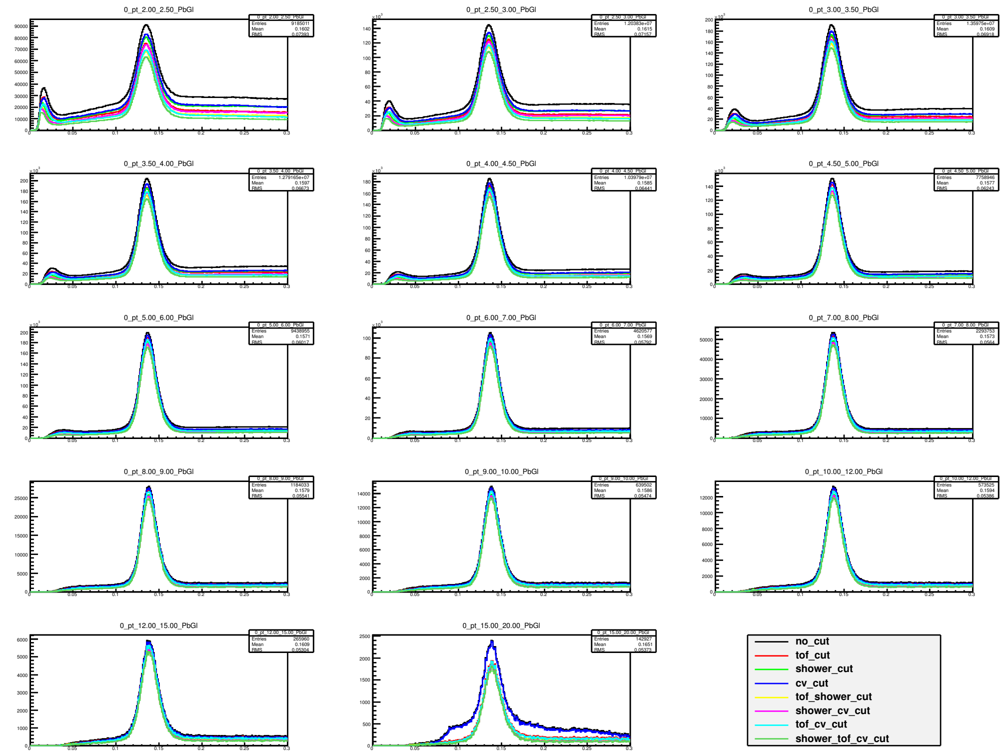

Figure 5.11: Run13 di-photon invariant mass spectra with cut combinations for PbGl for P_T bins.

Chapter 6

Relative Luminosity

6.1 Relative Luminosity

Relative luminosity (R) is ratio of luminosity of same helicity crossings to luminosity of opposite helicity crossings.

$$R = \frac{L_{++}}{L_{+-}} \tag{6.1}$$

As discussed in 4.1, relative luminosity is one of the key piece of A_{LL}. Relative luminosity and its uncertainties are underlying source of systematic uncertainty of all A_{LL} measurements. Thus it is very important to measure relative luminosity as precise as possible.

As $128 pb^{-1}$ data are taken and analyzed, statistical uncertainty becomes comparable to systematic uncertainty from the relative luminosity. Thus it is very important to reduce systematic uncertainty from the relative luminosity to conserve physics message of the A_{LL} measurements.

Relative luminosity of Run12 and Run13 are summarized in Fig. 6.1 and Fig. 6.2. Relative luminosity is calculated run-by-run way and GL1p and Starscaler are used to calculate it.

For precise measurement of relative luminosity, conditions required for luminosity detector are

- Low background from noise or beam gas events
- High statistics
- Same acceptance i.e. $|\mathrm{vertex_z}| < 30$ as channel we are interested in
- No spin dependence, i.e. should have a small A_{LL}.

That's why BBCLL1 is used for main luminosity detector. It's known that BBC has low background and high statistics. Acceptance is same because $|\mathrm{vertex_z}| < 30$ is used in this analysis. However A_{LL}^{BBC} problem isn't trivial. Remaining part of the chapter is dedicated to measure A_{LL}^{BBC} and its uncertainties.

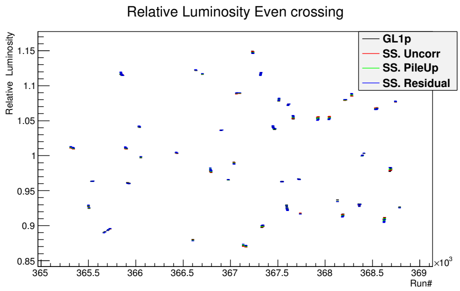

(a) Even Crossing

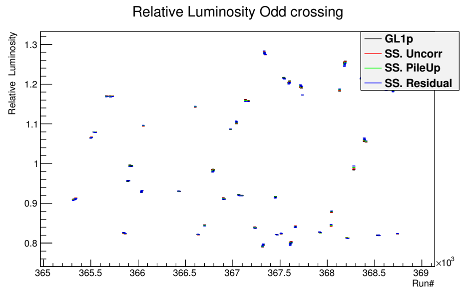

(b) Odd Crossing

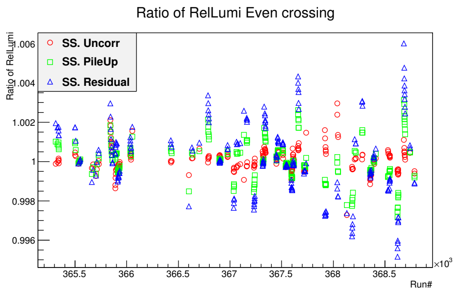

(c) Even Crossing

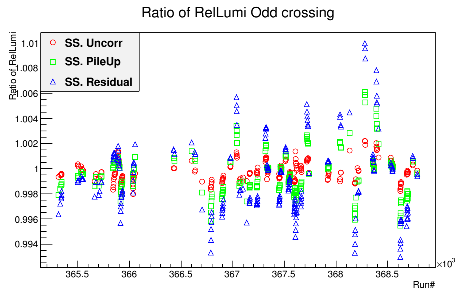

(d) Odd Crossing

Figure 6.1: (Top) Run12 relative luminosity vs. runnumber. Black points are relative luminosity calculated with GL1p scaler and red points are relative luminosity calculated with Starscaler without pileup correction. Star Scaler with pileup correction. Green points are relative luminosity calculated with Starscaler with pileup corrected scaler counts. (Bottom) Ratio of relative luminosity with correction to relative luminosity without correction. Effect of scaler correction on relative luminosity is not significant.

6.2 $A_{LL}^{ZDC/BBC}$

We need to measure A_{LL}^{BBC} carefully to check the fourth condition is satisfied or not. Definition of A_{LL}^{BBC} is following.

$$A_{LL}^{BBC} = \frac{1}{P_B P_Y} \frac{\frac{N_{BBC}^{++}}{L_{++}} - \frac{N_{BBC}^{+-}}{L_{+-}}}{\frac{N_{BBC}^{++}}{L_{++}} + \frac{N_{BBC}^{+-}}{L_{+-}}} \tag{6.2}$$

In Eq. 6.2, we can see we need another luminosity counter for L_{++} and L_{+-}. Second detector for luminosity counter is ZDC because it's known that ZDC has low background

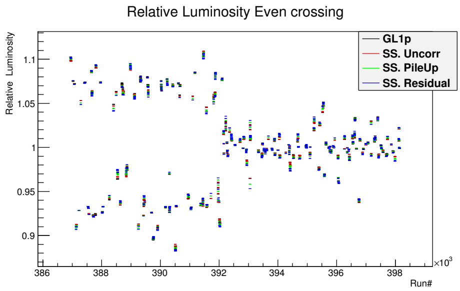

(a) Even Crossing

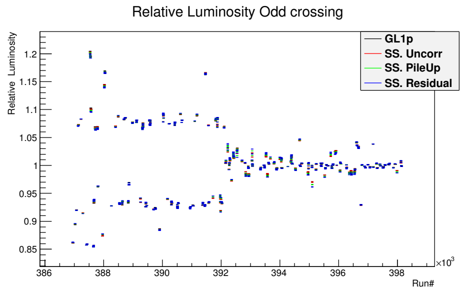

(b) Odd Crossing

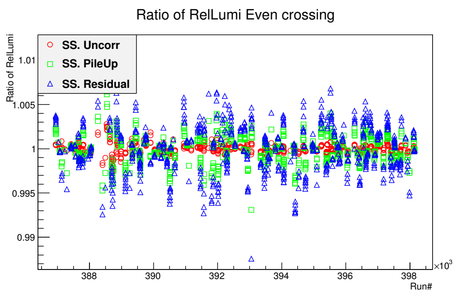

(c) Even Crossing

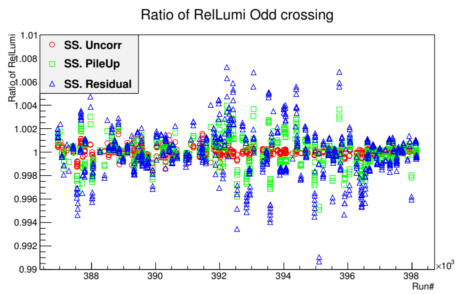

(d) Odd Crossing

Figure 6.2: (Top) Run13 relative luminosity vs. runnumber. From middle of Run13, unfilled four bunches had been filled. That's why there is sudden change in relative luminosity. (Bottom) Ratio of relative luminosity with correction to relative luminosity without correction. See Fig. 6.1 for detail meaning of points.

and enough statistics. Thus what we measure in practically is

$$A_{LL}^{ZDC/BBC} = \frac{1}{P_B P_Y} \frac{\frac{N_{ZDC}^{++}}{N_{BBC}^{++}} - \frac{N_{ZDC}^{+-}}{N_{BBC}^{+-}}}{\frac{N_{ZDC}^{++}}{N_{BBC}^{++}} + \frac{N_{BBC}^{+-}}{N_{BBC}^{+-}}}. \tag{6.3}$$

Because kinematic range and detecting scheme of BBC and ZDC are completely different, it's hard that $A_{LL}^{ZDC/BBC} = 0$ although $A_{LL}^{BBC} = A_{LL}^{ZDC} = A \neq 0$. Thus it's OK to measure $A_{LL}^{ZDC/BBC} = 0$ for estimation of A_{LL}^{BBC}.

6.3 Measuring $A_{LL}^{ZDC/BBC}$

$A_{LL}^{ZDC/BBC}$ is measured by following procedures. First ZDC/BBC ratio is drawn as function of bunch ID. Each scaler counts are from Star Scaler and $|\text{vertex}_z| < 30cm$ is required. Then the ratio is fit by the Eq. 6.4 and raw asymmetry, ε_{LL} is obtained. Let's call this fitting “bunch fitting”.

$$r(i) = C \times (1 + \varepsilon_{LL} \times \text{Helicity Index}_{\text{Blue}} \times \text{Helicity Index}_{\text{Yellow}}) \tag{6.4}$$

where helicity index is 1 for positive helicity bunches and -1 for negative helicity bunches. Fig. 6.3 is example of “bunch fitting” for single run, Runnumber 386946.

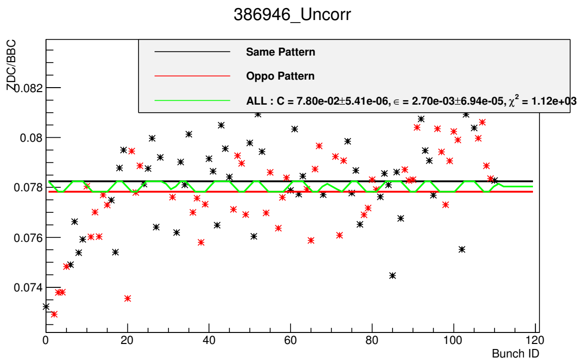

Figure 6.3: Example of bunch fitting without any correction. (Runnumber 386946) Black points are the ZDC/BBC ratios for same helicity crossing and red point are the ratios for opposite helicity crossing. Black line is a constant function fit on same helicity crossing and red line is a constant fit on opposite helicity crossings. Green line is a function described in Eq. 6.4 fit on all crossings.

Physics asymmetry, $A_{LL}^{ZDC/BBC}$ is calculated by normalizing polarization of each RHIC beam. Uncertainty of $A_{LL}^{ZDC/BBC}$ includes $\Delta\varepsilon_{LL}$ from bunch fitting and statistical uncertainties of each RHIC beam polarizations. Considering large χ^2_{re} of bunch fitting, $\Delta\varepsilon_{LL}$ is scaled by $\sqrt{\chi^2_{re}}$ of bunch fitting. The procedure above has been done for all runnumber.

$$\Delta A_{LL}^{ZDC/BBC} = \frac{1}{P_B P_Y}\sqrt{(\Delta\varepsilon_{LL} \times \sqrt{\chi^2_{re}})^2 + \varepsilon^2_{LL}\left((\frac{\Delta P_B}{P_B})^2 + (\frac{\Delta P_Y}{P_Y})^2\right)} \tag{6.5}$$

However, until correction parameters are fixed, scaling of uncertainty of ε_{LL} is omitted because it dilute behavior of each correction.

Then, constant fitting has been done and $A_{LL}^{ZDC/BBC}$ has been taken. Let’s call the fitting “run fitting”. Fig. 6.4 shows result of “run fitting”. Without any correction,

$$\begin{aligned} A_{LL}^{ZDC/BBC} &= 2.552 \times 10^{-4} \pm 2.039 \times 10^{-5} \\ \chi^2_{re}(runfitting) &= 1.133 \times 10^{4}/219 = 5.174 \times 10^{1} \\ \overline{\chi^2_{re}(bunchfitting)} &= 1.675 \times 10^{3} \end{aligned} \tag{6.6}$$

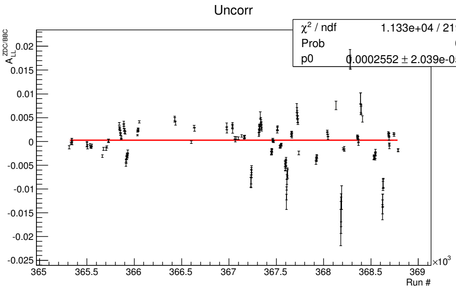

(a) Run12

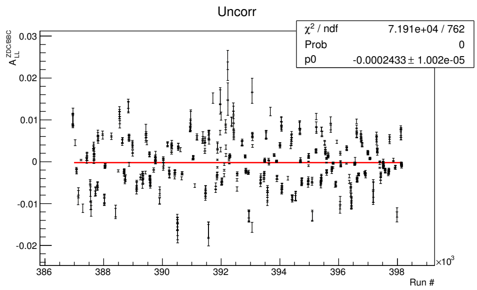

(b) Run13

Figure 6.4: Run fitting without any correction. Scaling factor of $\Delta\varepsilon_{LL}$ from χ^2_{re} of bunch fitting is not considered.

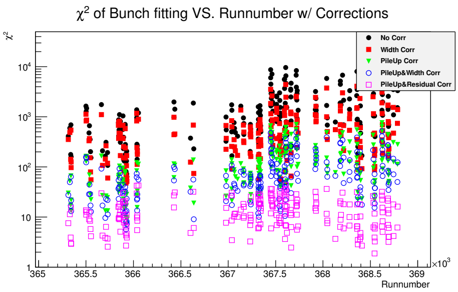

(a) Run12

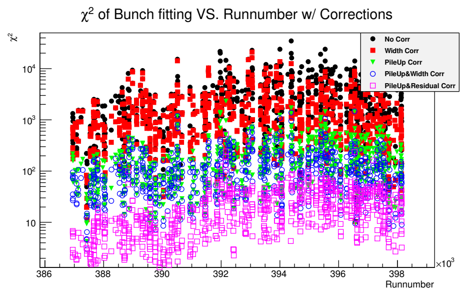

(b) Run13

Figure 6.5: Run-by-run χ^2_{re} of bunch fittings with various corrections.

is obtained for Run12 and

$$\begin{aligned} A_{LL}^{ZDC/BBC} &= -2.433\times10^{-4} \pm 1.002\times10^{-5} \\ \chi^2_{re}(runfitting) &= 7.191\times10^{4}/762 = 9.437\times10^{1} \\ \overline{\chi^2_{re}(bunchfitting)} &= 3.084\times10^{3} \end{aligned} \tag{6.7}$$

is obtained for Run13. Fig 6.5 shows run-by-run χ^2_{re} of bunch fittings. Corrections in Fig 6.5 will be explained in Sec. 6.4, 6.5, and 6.6.

6.4 Pileup Correction

6.4.1 Motivation and Procedure

Pileup of collisions can occur when there is two or more $p+p$ collisions in single bunch crossing. Fig. 6.6 shows how pileup of collisions and scaler miscount occur. As collision rate increases, likelihood of the pileup increases. As collision rate has increased in Run13 much, it is very important to correct scaler miscount due to the pileup of collisions.

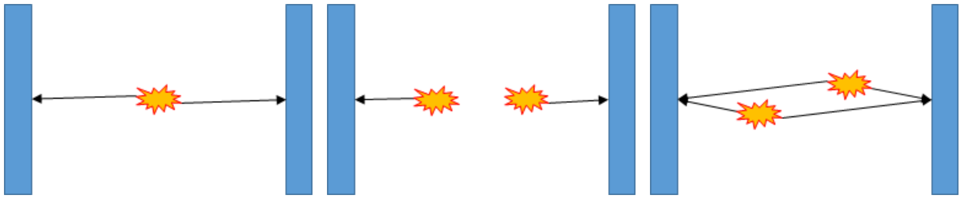

Figure 6.6: How pileup of collisions occurs. Blue rectangles represents south and north side BBC or ZDC. Yellow stars represents collisions occur. Black arrows represent particles from the corresponding collision detected by the side of BBC or ZDC. (a) One collision occurs and one "real" collision vertex is reconstructed. (b) Two collisions occur and one "wrong" collision vertex is reconstructed by two single sided events. Actually no collision vertex should not have been reconstructed in the case. Scaler overcount occurs. (c) Two collisions occur and only one collision vertex is reconstructed because BBC or ZDC can not distinguish two particles from two corresponding collisions. Actually two collision vertexes should have been reconstructed. Scaler undercount occurs.

Purpose of pileup correction[1] is restore scaler miscount caused by the pileup of collision by finding relation between true coincident collision rate, Coin. Rate^{true} and observed coincident collision rate, Coin. Rate$^{ob.}$. To describe conclusion first, Eq. 6.8 is the relation.

$$\begin{aligned} \text{Coin. Rate}^{ob.} = 1 - &e^{-\text{Coin. Rate}^{true}(1+k_N)} \\ &- e^{-\text{Coin. Rate}^{true}(1+k_S)} + e^{-\text{Coin. Rate}^{true}(1+k_N+k_S)} \end{aligned} \tag{6.8}$$

where, where, $k_{N(S)}$ is the exclusive north (south) side hit probability, $\varepsilon_{N(S)}$ to coincidence hit probability ratio, ε_{NS}. Derivation of Eq. 6.8 is discussed in the following.

For single collision, one of the following four things can occur.

- ε_0: the probability that no hit is observed in neither north side detector nor south side detector for a given collision.
- ε_N: the probability that hits are observed in north side detector but no hit is observed in south side detector for a given collision.
- ε_S: the probability that hits are observed in south side detector but no hit is observed in north side detector for a given collision.
- ε_{NS}: the probability that hits are observed in both of north and south side detectors for a given collision.

[1]The correction is called as rate correction, sometimes.

It’s obvious that there are only the four case and

$$\varepsilon_0 + \varepsilon_N + \varepsilon_S + \varepsilon_{NS} = 1 \tag{6.9}$$

is hold. Let’s define one more probability to proceed the derivation.

- $P(i,\mu)$: the probability that i different collisions occur when average collision rate is μ.
- $P(kl)$: the probability that north side detector observes hits from k different corresponding collisions and south side detector observes hits from l different corresponding collisions for a given bunch crossing.
- $P(kl|N)$: the conditional probability of $P(kl)$ when N collisions occurs.

As $p+p$ collision is very rare, $P(i,\mu)$ follows Poissonian statistics. One $p+p$ collision happens when $O(10^{11})$ protons pass through $O(10^{11})$ protons. Thus,

$$P(i,\mu) = \frac{e^{-\mu}\mu^i}{i!} \tag{6.10}$$

Let’s focus on $P(0,0)$, the probability that no hit is observed in neither north side detector nor south side detector for a given bunch crossing. Because the number of collisions occur for a given bunch crossing, i is arbitrary, $P(0,0)$ can be written as

$$P(0,0) = \sum_{i=0}^{\infty} P(00|i)P(i,\mu) \tag{6.11}$$

With $P(00|i) = \varepsilon_0^i$ and Eq. 6.10, Eq. 6.11 can be written as

$$\begin{aligned} P(0,0) &= \sum_{i=0}^{\infty} \varepsilon_0^i \frac{e^{-\mu}\mu^i}{i!} \\ &= e^{-\mu(1-\varepsilon_0)} \end{aligned} \tag{6.12}$$

Let’s proceed more and build $P(k>0,0)$, the probability that hits are observed in north side detector but no hit is observed in south side detector for a given bunch crossing. Firstly, we need to build $P(k,0)$.

$$\begin{aligned} P(k,0) &= \sum_{i=k}^{\infty} P(k,0|i)P(i,\mu) \\ &= \sum_{i=k}^{\infty} \binom{i}{k} \varepsilon_0^{i-k}\varepsilon_N^k \frac{e^{-\mu}\mu^i}{i!} \\ &= e^{-\mu(1-\varepsilon_0)} \frac{\mu\varepsilon_N^k}{k!} \end{aligned} \tag{6.13}$$

Then,

$$\begin{aligned}
P(k>0,0) &= \sum_{k=1}^{\infty} P(k,0) \\
&= \sum_{k=0}^{\infty} P(k,0) - P(0,0) \\
&= \sum_{k=0}^{\infty} e^{-\mu(1-\varepsilon_0)} \frac{\mu\varepsilon_N^k}{k!} - e^{-\mu(1-\varepsilon_0)} \\
&= e^{-\mu(1-\varepsilon_0)}(e^{\mu\varepsilon_N} - 1)
\end{aligned} \tag{6.14}$$

is obtained. By similar way,

$$P(0,l>0) = e^{-\mu(1-\varepsilon_0)}(e^{\mu\varepsilon_S} - 1) \tag{6.15}$$

is obtained.

Finally, $P(k>0,l>0)$, the probability that coincident true or accidental hits in both side of detector for a given bunch crossing, is obtained indirectly. By definition, it is obvious that sum of the $P(0,0)$, $P(k>0,0)$, $P(0,l>0)$ and $P(k>0,l>0)$ is 1. Then,

$$\begin{aligned}
P(k>0,l>0) &= 1 - P(0,0) - P(k>0,0) - P(0,l>0) \\
&= 1 - e^{-\mu(1-\varepsilon_0)} - e^{-\mu(1-\varepsilon_0)}(e^{\mu\varepsilon_N} - 1) - e^{-\mu(1-\varepsilon_0)}(e^{\mu\varepsilon_S} - 1) \\
&= 1 - e^{-\mu(\varepsilon_N+\varepsilon_{NS})} - e^{-\mu(\varepsilon_S+\varepsilon_{NS})} + e^{-\mu(\varepsilon_N+\varepsilon_S+\varepsilon_{NS})} \\
&= 1 - e^{-\mu\varepsilon_{NS}(1+k_N)} - e^{-\mu\varepsilon_{NS}(1+k_S)} + e^{-\mu\varepsilon_{NS}(1+k_N+k_S)}
\end{aligned} \tag{6.16}$$

is derived. Last step of Eq. 6.16 is done by introducing $k_N = \frac{\varepsilon_N}{\varepsilon_{NS}}$ and $k_S = \frac{\varepsilon_S}{\varepsilon_{NS}}$. In Eq. 6.16, $\mu\varepsilon_{NS}$ is nothing but true coincident rate and $P(k>0,l>0)$ is observed coincident rate. Then Eq. 6.8 is derived.

Observed coincident rate can be calculated by dividing each coincident scaler counts by Clock scaler counts. Then true coincident rate can be obtained by numerically solving Eq. 6.8. True coincident count can be obtained by multiplying true coincident rate and Clock scaler count.

Before applying pileup correction, we need to determine k_N and k_S.

6.4.2 Determining k_N and k_S

k_N and k_S can be determined with single sided and coincident scaler counts by Star scaler. Fig. 6.7 shows various scaler counts of example run. k_N and k_S of each bunch ID and runnumber are calculated with the scaler counts and drawn as function of the coincident rate. Then, constant fitting is done to obtain average value. Fig. 6.8 and Fig. 6.9 show the results. One thing to be cared is the pileup effect affects k_N and k_S also and suitable correction is needed. Eq. 6.17 and Eq. 6.18 are the necessary correction.

$$\begin{aligned}\text{Coin. Rate}^{true} =& ln(1-\text{Inc. Rate}^{ob.}_{N}-\text{Inc. Rate}^{ob.}_{S}+\text{Coin. Rate}^{Ob}) \\ &-ln(1-\text{Inc. Rate}^{ob.}_{N})-ln(1-\text{Inc. Rate}^{ob.}_{S})\end{aligned} \tag{6.17}$$

$$\text{Exc. Rate}^{true}_{N(S)} = -ln(1-\text{Inc. Rate}^{ob.}_{N(S)})-\text{Coin. Rate}^{true} \tag{6.18}$$

, where Coin. Rate^{true} is pileup corrected coincident rate, Exc. Rate$^{true}_{N(S)}$ is pileup corrected exclusive[2] north (south) sided rate and Inc. Rate$^{ob.}_{N(S)}$ is observed inclusive[3] north (south) sided rate. The derivation of Eq. 6.17 and Eq. 6.18 is very similar the derivation Eq. 6.8 and the derivation is not repeated, in here.

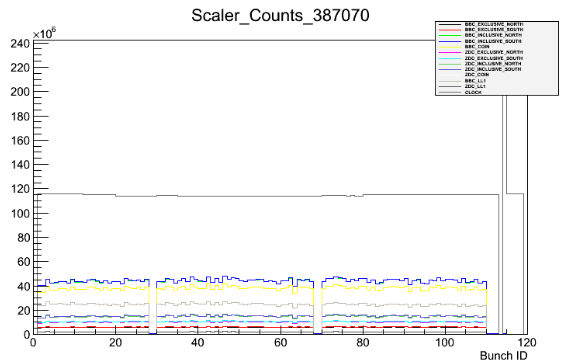

Figure 6.7: Various scaler counts vs. bunch ID for calculating k_N and k_S of example run.

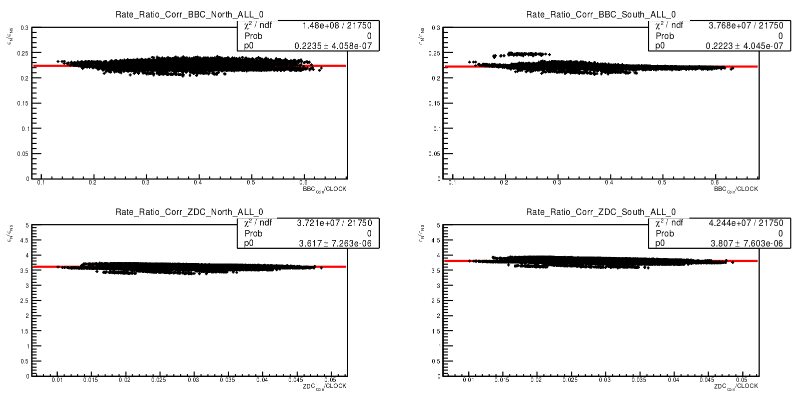

Figure 6.8: Determination of k_N and k_S of Run12. To remove rate dependence, each point is corrected as Eq. 6.17 and Eq. 6.18.

[2] single sided events only

[3] single sided or coincident events

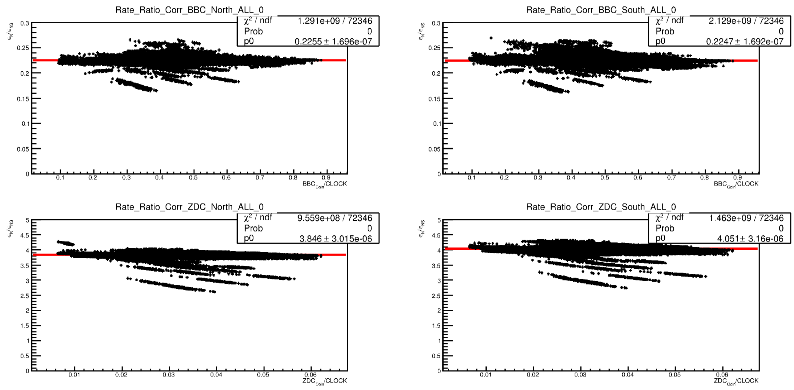

Figure 6.9: Determination of k_N and k_S of Run13. To remove rate dependence, each point is corrected as Eq. 6.17 and Eq. 6.18.

6.4.3 Effect of Pileup Correction on BBC and ZDC Scaler Rate

With determined k_N and k_S and observed scaler rates, true scaler rates are obtained with Eq. 6.8. Fig. 6.10 shows scaler undercounting is dominant for BBC and scaler overcounting is dominant for ZDC.

6.4.4 Effect of Pileup Correction on $A_{LL}^{ZDC/BBC}$

With the pileup correction,

$$\begin{aligned} A_{LL}^{ZDC/BBC} &= 3.188 \times 10^{-6} \pm 1.988 \times 10^{-5} \\ \chi^2_{re}(runfitting) &= 3.988 \times 10^3/219 = 1.821 \times 10^1 \\ \overline{\chi^2_{re}(bunchfitting)} &= 1.531 \times 10^2 \end{aligned} \tag{6.19}$$

is obtained for Run12 and

$$\begin{aligned} A_{LL}^{ZDC/BBC} &= -5.828 \times 10^{-5} \pm 9.293 \times 10^{-6} \\ \chi^2_{re}(runfitting) &= 2.606 \times 10^4/762 = 3.420 \times 10^1 \\ \overline{\chi^2_{re}(bunchfitting)} &= 2.047 \times 10^2 \end{aligned} \tag{6.20}$$

is obtained for Run13.

Fig. 6.11 show the effect of the pileup correction on example bunch fitting. We can see χ^2_{re} is decreased a lot. Fig. 6.5 shows that pileup correction reduces χ^2_{re} of bunch fitting successfully for other runs. Fig. 6.12 shows result of run fitting with pileup correction. We can see not only $A_{LL}^{ZDC/BBC}$ but also χ^2_{re} of run fitting are reduced. (cf. Fig. 6.4) The reduction of χ^2_{re} implies the pileup correction works well.

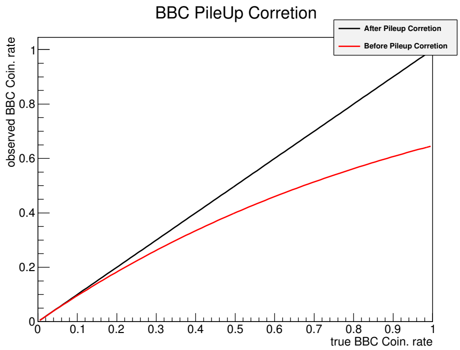

(a) Run12 BBC

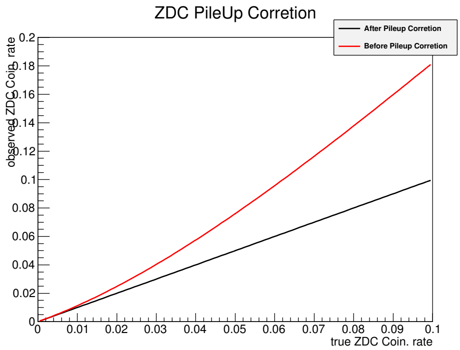

(b) Run12 ZDC

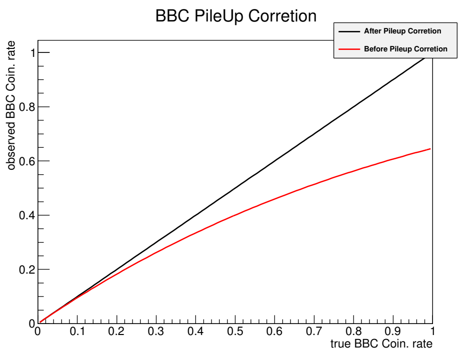

(c) Run13 BBC

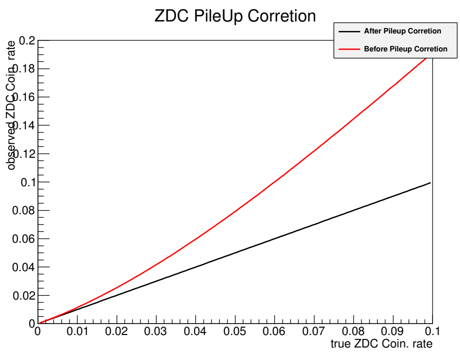

(d) Run13 ZDC

Figure 6.10: BBC and ZDC Rate with and without Pileup Correction. For BBC, scaler undercounting is dominant for high rate. For ZDC, scaler overcounting is dominant for high rate.

6.4.5 Vertex$_z$ Cut and Spin Pattern Separation Problem

When 30cm vertex$_z$ cut is applied on scaler counts, pileup correction fails a bit because of no consideration of vertex$_z$ cut when Eq. 6.8 is derived. Thus pileup correction works really well when no vertex$_z$ cut is applied only. As discussed in Subsec. 5.2.2, this measurement needs vertex$_z$ cut scaler counts. This means additional correction which handles effects of vertex$_z$ cut is needed. Without the additional correction, unacceptable increase of $A_{LL}^{ZDC/BBC}$ and spin pattern separation problem occurs. Fig. 6.13 shows this.

Width correction and residual rate correction are the correction for vertex$_z$ cut. Width correction is discussed in Sec. 6.5 and residual rate correction is discussed in Sec. 6.6.

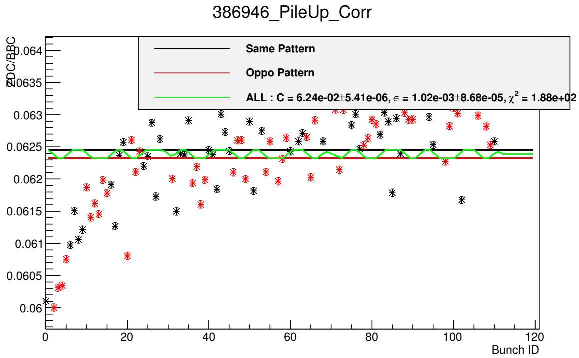

Figure 6.11: Example of bunch fitting with pileup correction. (Runnumber 386946) χ^2_{re} is dramatically reduced. (cf. Fig. 6.3)

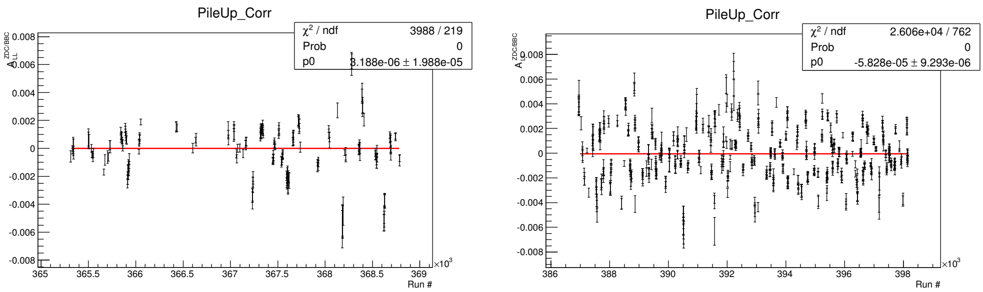

(a) Run12 (b) Run13

Figure 6.12: Run fitting with pileup correction. Not only $A_{LL}^{ZDC/BBC}$ but also χ^2_{re} are successfully reduced. (cf. Fig. 6.4) Scaling factor of $\Delta\varepsilon_{LL}$ from χ^2_{re} of bunch fitting is not considered.

6.5 Width Correction

6.5.1 Motivation and Procedure

Width correction is a classical way to handle scaler miscount due to vertex$_z$ cut, especially for ZDC. As discussed in Subsec. 3.1.2, vertex$_z$ resolution of ZDC is poor compared to width of vertex$_z$ distribution. With the poor resolution, scaler undercount can happens when vertex$_z$ cut is applied. To justify the statement, let's think two extreme cases. First case is vertex$_z$ is distributed very narrow like δ-function. In the case, every collision should have passed the vertex$_z$ cut. However, some of vertex$_z$ are reconstructed wrongly due to the poor resolution and cut by vertex$_z$ cut. Second case is vertex$_z$ is distributed uniformly i.e., infinity width. Scaler undercount and overcount are balanced when vertex$_z$ are distributed uniformly. For real vertex$_z$ distribution, scaler undercount and overcount happens simultaneously but scaler undercount is dominant and net scaler undercount

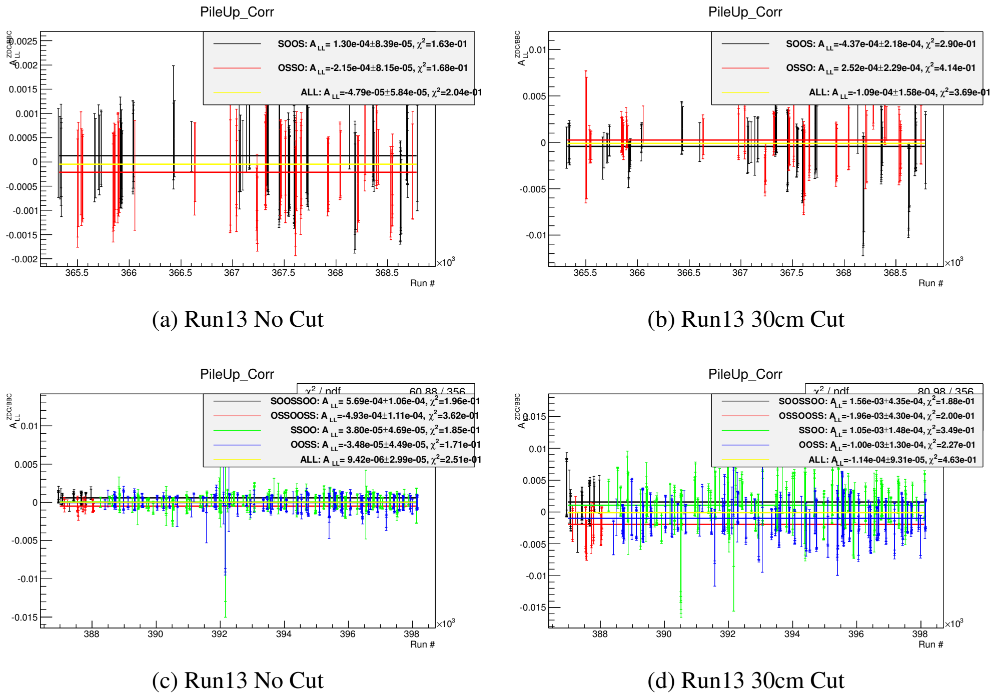

(a) Run13 No Cut

(b) Run13 30cm Cut

(c) Run13 No Cut

(d) Run13 30cm Cut

Figure 6.13: Effect of vertex$_z$ cut on $A_{LL}^{ZDC/BBC}$. When vertex$_z$ cut is applied, $A_{LL}^{ZDC/BBC}$ increases and spin pattern separation problem occurs. Scaling factor of $\Delta\varepsilon_{LL}$ from χ^2_{re} of bunch fitting is considered, in here.

occurs.

With the discussion above, ZDC undercounting is expected and the undercounting will depend on the vertex$_z$ width. The narrower vertex$_z$ width, the more undercounting will occur. Thus we need to correct ZDC/BBC ratio by vertex$_z$ width.

To parametrize vertex$_z$ width, we define σ_{proxy} which is

$$\sigma_{proxy} = \frac{ZDC_{out}}{ZDC_{narrow}} \tag{6.21}$$

where $ZDC_{narrow} = ZDC_{30cm}$ and $ZDC_{out} = ZDC_{NoVtx} - ZDC_{norrow}$. The larger σ_{proxy}, the larger vertex$_z$ width and the large ZDC/BBC ratio if above understanding is true. Fig. 6.14 shows there is such a correlation between σ_{proxy} and the ratio.

Thus, it's natural to assert that the ratio should be correct as:

$$\left(\frac{ZDC}{BBC}\right)' = \left(\frac{ZDC}{BBC}\right)\frac{<\frac{ZDC}{BBC}>}{P_0 + P_1\sigma_{proxy}} \tag{6.22}$$

The correction is so called width correction.

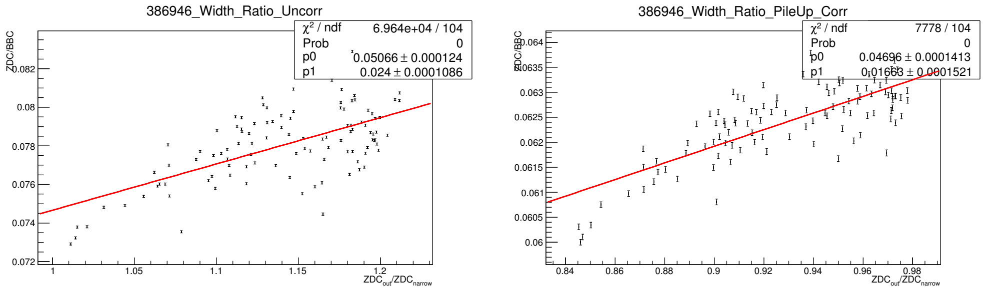

(a) Before Pileup Correction

(b) After Pileup Correction

Figure 6.14: Correlation between vertex width and ZDC/BBC ratio before and after pileup correction. Correlation itself is clear. However large χ^2_{re} implies there may other structure exists although χ^2_{re} is reduced much after pileup correction is applied.

6.5.2 Effect of Width Correction on $A_{LL}^{ZDC/BBC}$

With the width correction,

$$\begin{aligned} A_{LL}^{ZDC/BBC} &= 5.017\times 10^{-5} \pm 1.937\times 10^{-5} \\ \chi^2_{re}(runfitting) &= 3.619\times 10^{3}/219 = 1.653\times 10^{1} \\ \overline{\chi^2_{re}(bunchfitting)} &= 9.438\times 10^{1} \end{aligned} \tag{6.23}$$

is obtained for Run12 and

$$\begin{aligned} A_{LL}^{ZDC/BBC} &= -1.704\times 10^{-5} \pm 8.794\times 10^{-6} \\ \chi^2_{re}(runfitting) &= 1.931\times 10^{4}/762 = 2.534\times 10^{1} \\ \overline{\chi^2_{re}(bunchfitting)} &= 1.279\times 10^{2} \end{aligned} \tag{6.24}$$

is obtained for Run13.

Fig. 6.15 shows the effect of the width correction on example bunch fitting. By Fig. 6.5, it is clear that the effect of width correction on χ^2_{re} of bunch fitting is limited. For Run12, χ^2_{re} of bunch fitting is even increased. Thus the effect of the width correction is unclear.

6.5.3 Spin Pattern Separation Problem and Width Correction

The width correction can not solve the spin pattern separation problem enough also. Fig. 6.17 shows the spin pattern separation of $A_{LL}^{ZDC/BBC}$ and still lots of spin pattern separation still remains. It may imply the width correction miss some important factor behind.

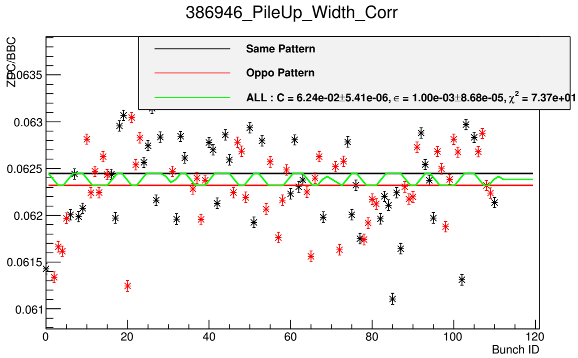

Figure 6.15: Example of bunch fitting with pileup and width correction. χ^2_{re} is reduced additionally by width correction but still large. (cf. Fig. 6.11)

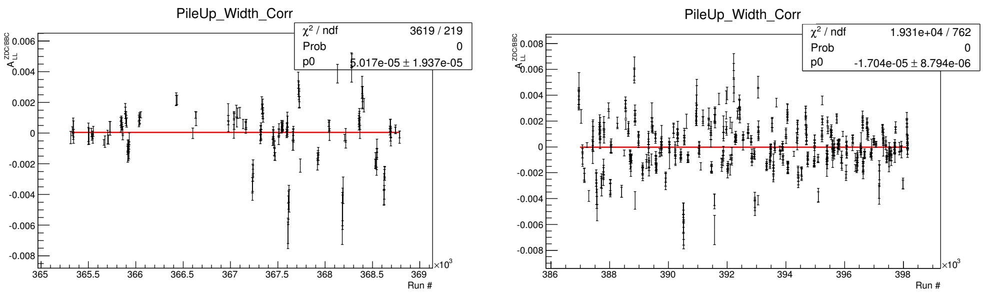

(a) Run12

(b) Run13

Figure 6.16: Run fitting with pileup and width correction. $A_{LL}^{ZDC/BBC}$ of Run13 is decreased but $A_{LL}^{ZDC/BBC}$ of Run12 is increased. χ^2_{re} are a bit decreased for both of Runs but the effect is limited. (cf. Fig. 6.4) Scaling factor of $\Delta\varepsilon_{LL}$ from χ^2_{re} of bunch fitting is not considered.

6.5.4 Criticism on Width Correction

Although width correlation is observed in data (see Fig. 6.14) and width correction succeeds in reducing χ^2_{re} of bunch fitting and run fitting to a certain extent, validity of width correction is questionable.

First reason is large fluctuation of width correlation. Fig. 6.18 shows it. Large χ^2_{re} of the correlation is second concern. Pileup correction fixes the two concern mostly but not perfectly. The other and the most critical reason is some runs have negative correlation. Pileup correction can't fix it. Even after pileup correction applied, there are some runs still have negative correlation. When we've introduced width correction in Subsec. 6.5.1, we've assumed the wider vertex width, the more ZDC counts and the higher ZDC/BBC ratio. Thus the negative correlation is completely out of range of width correction and there must be something the width correction overlooks. For the above reason, width

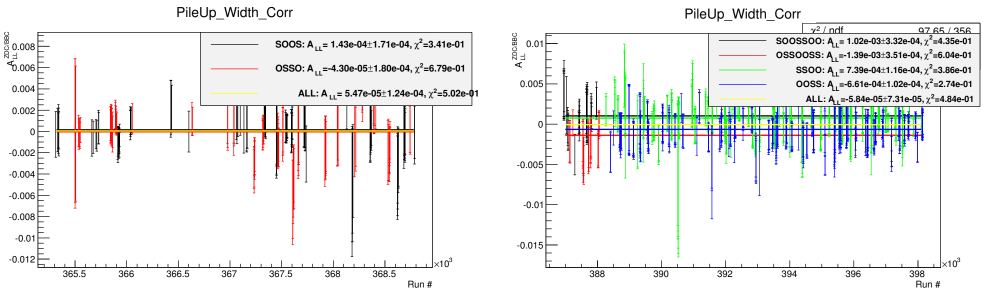

(a) Run12 (b) Run13

Figure 6.17: Spin pattern separated run fitting with pileup and width correction. Significant spin pattern separation still remains, especially for Run13. Scaling factor of $\Delta\varepsilon_{LL}$ from χ^2_{re} of bunch fitting is considered, in here.

correction is abandoned.

In Sec. 6.6, residual rate correction will be discussed for the alternative way of correcting scaler miscount from vertex cut.

6.6 Residual Rate Correction

6.6.1 Motivation and Procedure

The idea of residual rate correction is following. Firstly, let's define factor f as the fraction of crossings where a coincidence is found, real or accidental, such that the vertex$_z$ is reconstructed within the 30cm vertex$_z$ cut.

$$f = \frac{\text{Observed 30cm vertex}_z \text{ scaler count}}{\text{Observed no vertex}_z \text{ scaler count}} \tag{6.25}$$

Bunch-by-bunch factor f can be obtained from Star Scaler data. If we apply the factor f to observed rate in Eq. 6.8, we can obtain vertex$_z$ cut true rate approximately.

$$\begin{aligned} \text{Rate}_{obs} &\rightarrow f\text{Rate}_{obs} \\ \text{Rate}_{obs} &= F(\text{Rate}_{true}) \\ \rightarrow f\text{Rate}_{obs} &\approx F(\text{Rate}_{true,vtx}) \end{aligned} \tag{6.26}$$

where, F is right-hand side of Eq. 6.8. If we solve Eq. 6.26, Rate$_{true}$ and Rate$_{true,vtx}$ are obtained.

$$\begin{aligned} \text{Rate}_{true} &= F^{-1}(\text{Rate}_{obs}) \\ \text{Rate}_{true,vtx} &\approx F^{-1}(f\text{Rate}_{obs}) \end{aligned} \tag{6.27}$$

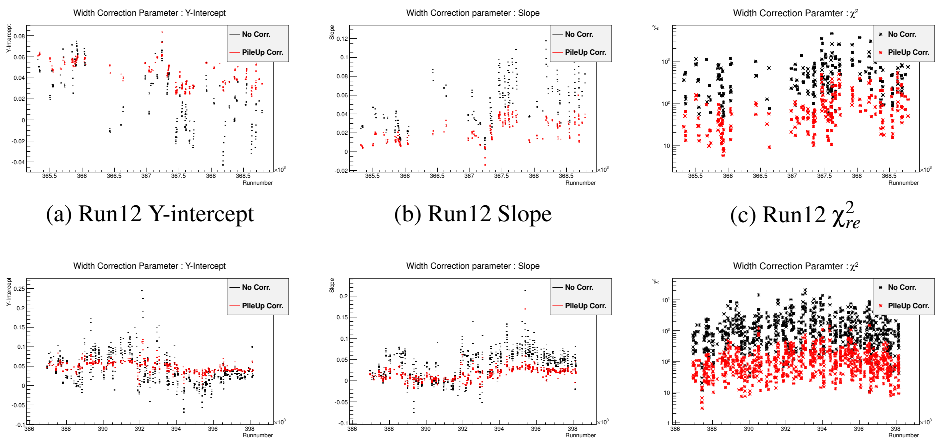

(a) Run12 Y-intercept (b) Run12 Slope (c) Run12 χ^2_{re}

(d) Run13 Y-intercept (e) Run13 Slope (f) Run13 χ^2_{re}

Figure 6.18: Width correlation parameters vs. runnumber without and with pileup correction. Run-by-run correlation parameters fluctuation is a lot, although pileup correction fixes it much. Large χ^2_{re} is other concern. However most strange thing is some runs have negative correlation. The behavior can not be explainable under hypothesis of width correction.

By using Eq. 6.27, we can see additional factor appears in the relation between Rate_{true} and $\text{Rate}_{true,vtx}$.

$$\begin{aligned} \text{Rate}_{true,vtx} &\approx f\text{Rate}_{true}/C_{res} \\ \text{instead of } \text{Rate}_{true,vtx} &= f\text{Rate}_{true} \\ \text{where, } C_{res} &\equiv \frac{fF^{-1}(\text{Rate}_{obs})}{F^{-1}(f\text{Rate}_{obs})} \end{aligned} \tag{6.28}$$

Instead of observed no vertex$_z$ cut rate, C_{res} can be written in observed vertex$_z$ cut rate.

$$C_{res} = \frac{fF^{-1}(\frac{1}{f}\text{Rate}_{obs,vtx})}{F^{-1}(\text{Rate}_{obs,vtx})} \tag{6.29}$$

As Eq. 6.28 shows, $\text{Rate}_{true,vtx}$ is suppressed as C_{res}. Thus we need to correct it by multiplying C_{res} to observed vertex$_z$ cut rate.

$$\text{Rate}_{obs,vtx,residual} = \text{Rate}_{obs,vtx} \times C_{res} \tag{6.30}$$

That's the residual rate correction.

C_{res} is obtained by solving Eq. 6.29 with bunch-by-bunch f and observed vertex$_z$ cut rate. Fig. 6.19 shows calculated C_{res} of BBC and ZDC.

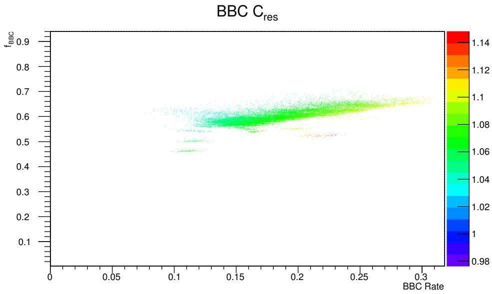

(a) Run12 BBC

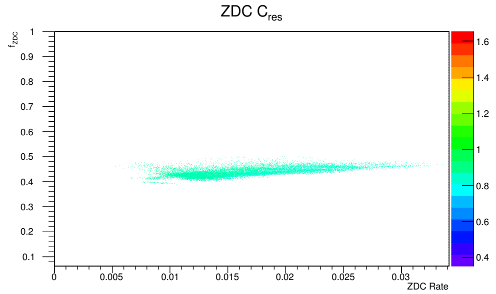

(b) Run12 ZDC

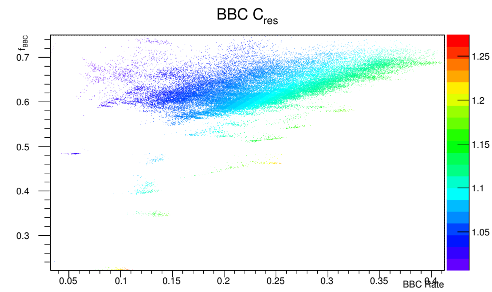

(c) Run13 BBC

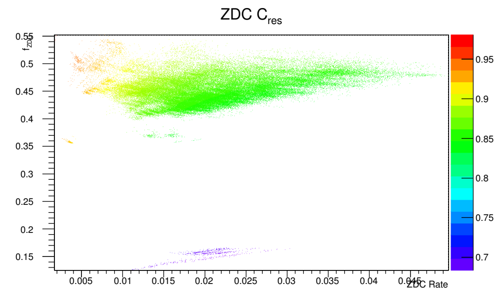

(d) Run13 ZDC

Figure 6.19: C_{res} of BBC and ZDC. Horizontal axis is observed vertex cut rate of BBC and ZDC. Vertical axis is the factor f of BBC and ZDC. Color code of C_{res} is in right axis of the plots.

6.6.2 Connection to Width Correction

Like the width correction, the residual rate correction is applied to correct scaler miscount by the factor f. By definition, the factor f has negative correlation with vertex$_z$ width and corrects scaler miscount due to vertex$_z$ cut. Thus the residual rate correction is the generalized version of the width correction.

6.6.3 Effect of Residual Rate Correction on $A_{LL}^{ZDC/BBC}$

With the residual rate correction,

$$\begin{aligned} A_{LL}^{ZDC/BBC} &= 7.964 \times 10^{-5} \pm 2.113 \times 10^{-5} \\ \chi^2_{re}(runfitting) &= 4.560 \times 10^2/219 = 2.082 \times 10^0 \\ \overline{\chi^2_{re}(bunchfitting)} &= 1.454 \times 10^1 \end{aligned} \tag{6.31}$$

is obtained for Run12 and

$$\begin{aligned} A_{LL}^{ZDC/BBC} &= 5.610 \times 10^{-5} \pm 1.002 \times 10^{-5} \\ \chi^2_{re}(runfitting) &= 4.237 \times 10^3 / 762 = 5.560 \times 10^0 \\ \overline{\chi^2_{re}(bunchfitting)} &= 2.355 \times 10^1 \end{aligned} \tag{6.32}$$

is obtained for Run13.

Fig. 6.20 show the effect of the residual rate correction on example bunch fitting. We can see χ^2_{re} is decreased really much. Fig. 6.5 shows that residual rate correction reduces χ^2_{re} of run fitting for other runs. Although $A_{LL}^{ZDC/BBC}$ increases a bit, dramatically reduced χ^2_{re} of bunch fitting and run fitting support validity of the correction.

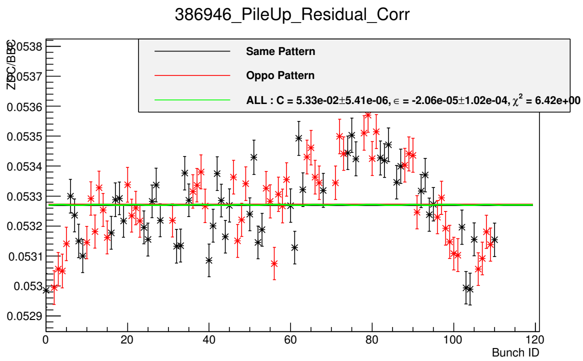

Figure 6.20: Example of bunch fitting with residual rate correction. χ^2_{re} is reduced dramatically by residual rate correction. (Cf. Fig. 6.11 and Fig. 6.15)

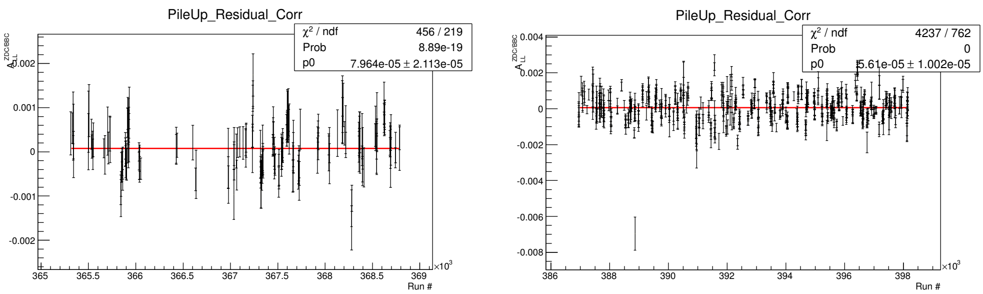

(a) Run12

(b) Run13

Figure 6.21: Run fitting with residual rate correction. $A_{LL}^{ZDC/BBC}$ is a bit increased. However χ^2_{re} is dramatically reduced. (cf. Fig. 6.12 and 6.16) Scaling factor of $\Delta\epsilon_{LL}$ from χ^2_{re} of bunch fitting is not considered.

6.6.4 Spin Pattern Separation Problem and Residual Rate Correction

Substantial amount of the spin pattern separation problem is resolved by the residual rate correction. Fig. 6.22 show the result. The validity of the residual rate correction is supported again.

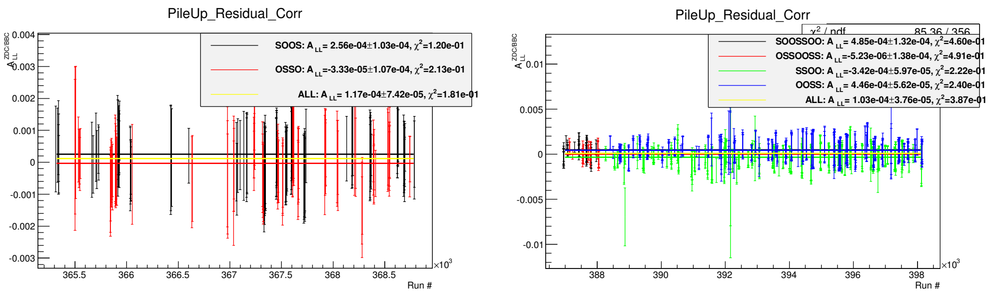

(a) Run12 (b) Run13

Figure 6.22: Spin pattern separated run fitting with residual rate correction. Compared with Fig. 6.17, significant amount of spin pattern separation of $A_{LL}^{ZDC/BBC}$ is removed. Scaling factor of $\Delta\varepsilon_{LL}$ from χ^2_{re} of bunch fitting is considered, in here.

6.7 Measured $A_{LL}^{ZDC/BBC}$

With pileup and residual rate correction, $A_{LL}^{ZDC/BBC}$ has been measured. Fig. 6.22 shows the result. In the result, still large χ^2_{re} of bunch fitting is considered by multiplying $\sqrt{\chi^2_{re}}$ on statistical uncertainty of each bunch fitting.

$$\begin{aligned} \text{Run12: } A_{LL}^{ZDC/BBC} &= 1.172 \times 10^{-4} \\ \text{Run13: } A_{LL}^{ZDC/BBC} &= -1.026 \times 10^{-4} \end{aligned} \tag{6.33}$$

6.7.1 Statistical Uncertainty

Statistical uncertainty of $A_{LL}^{ZDC/BBC}$ is estimated by uncertainty of fitting.

$$\begin{aligned} \text{Run12: } \Delta A_{LL}^{ZDC/BBC}(stat.) &= 7.424 \times 10^{-5} \\ \text{Run13: } \Delta A_{LL}^{ZDC/BBC}(stat.) &= 3.762 \times 10^{-5} \end{aligned} \tag{6.34}$$

is assigned as statistical uncertainty.

6.7.2 Systematic Uncertainty

Due to Correction

To estimate any systematic uncertainty form corrections, $A_{LL}^{ZDC/BBC}$s are obtained with varied correction parameters. With pileup and residual rate correction, the correction parameters which can affect measured $A_{LL}^{ZDC/BBC}$ are k_N and k_S. As Fig. 6.8 and Fig. 6.9 shows, The k_N and k_S are obtained by fitting. The k_N and k_S are varied by adding $N \times \sqrt{\chi^2_{re}} \times$ statistical uncertainty of the fitting, where $N = -2, -1, 0, 1, 2$. $A_{LL}^{ZDC/BBC}$ has been calculated with 25 kinds of correction parameters sets. Fig. 6.23 shows the result and we can check variance of $A_{LL}^{ZDC/BBC}$ is small. From the variance of $A_{LL}^{ZDC/BBC}$,

$$
\begin{aligned}
\text{Run13: } \Delta A_{LL}^{ZDC/BBC}(syst.correction) &= 7.003 \times 10^{-8} \\
\text{Run13: } \Delta A_{LL}^{ZDC/BBC}(syst.correction) &= 8.727 \times 10^{-8}
\end{aligned}
\tag{6.35}
$$

is assigned as systematic uncertainty from corrections. The uncertainty is negligible compared to other uncertainties.

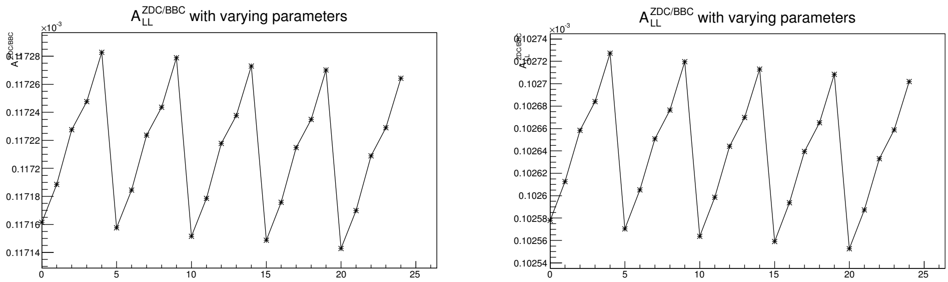

(a) Run12 (b) Run13

Figure 6.23: $A_{LL}^{ZDC/BBC}$ with varied correction parameters, k_N and k_S to estimate systematic uncertainty due to k_N and k_S determination.

Due to Spin Pattern Separation

Fig. 6.22 shows result of spin pattern separated run fitting and $A_{LL}^{ZDC/BBC}$ for each spin pattern. There is clear difference of $A_{LL}^{ZDC/BBC}$ for each spin pattern. The difference is handled as source of systematic uncertainty. Systematic uncertainty is assigned by weight average of absolute deviation of each spin pattern separated $A_{LL}^{ZDC/BBC}$. Square of statistical uncertainty of each spin pattern is assigned as the weight.

$$
\begin{aligned}
\text{Run12: } \Delta A_{LL}^{ZDC/BBC}(syst, pattern) &= 1.445 \times 10^{-4} \\
\text{Run13: } \Delta A_{LL}^{ZDC/BBC}(syst.pattern) &= 3.694 \times 10^{-4}
\end{aligned}
\tag{6.36}
$$

is assigned as systematic uncertainty from spin pattern difference of $A_{LL}^{ZDC/BBC}$.

ΔA_{LL} due to Relative Luminosity

From the discussion above, measured $A_{LL}^{ZDC/BBC}$ is

$$\begin{aligned} A_{LL}^{ZDC/BBC} =& 1.172\times10^{-4}\pm7.424\times10^{-5}(stat.)\\ &\pm7.003\times10^{-8}(syst.correction)\\ &\pm1.445\times10^{-4}(syst.pattern) \end{aligned} \tag{6.37}$$

for Run12 and

$$\begin{aligned} A_{LL}^{ZDC/BBC} =& -1.026\times10^{-4}\pm3.762\times10^{-5}(stat.)\\ &\pm8.727\times10^{-8}(syst.correction)\\ &\pm3.694\times10^{-4}(syst.pattern) \end{aligned} \tag{6.38}$$

for Run13. By quadratic sum, ΔA_{LL} due to relative luminosity

$$\begin{aligned} &\text{Run12: } \Delta A_{LL}(Rel.Lumi) = 2.003\times10^{-4}\\ &\text{Run13: } \Delta A_{LL}(Rel.Lumi) = 3.853\times10^{-4} \end{aligned} \tag{6.39}$$

is assigned.

	Uncorr	**Pileup**	**Width**	**Residual**
$A_{LL}^{ZDC/BBC}$	-2.18×10^{-4}	-1.09×10^{-4}	5.47×10^{-4}	1.17×10^{-4}
$\chi^2_{re}(run)$	5.17×10^{1}	1.82×10^{1}	1.65×10^{1}	2.08×10^{0}
$\overline{\chi^2_{re}(bunch)}$	1.68×10^{3}	6.73×10^{2}	9.44×10^{2}	1.45×10^{1}
Syst.Pattern	6.23×10^{-3}	3.44×10^{-4}	9.28×10^{-5}	1.44×10^{-4}

Table 6.1: Run12 summary of corrections on scaler counts.

	Uncorr	**Pileup**	**Width**	**Residual**
$A_{LL}^{ZDC/BBC}$	-2.43×10^{-4}	-5.83×10^{-5}	-1.70×10^{-5}	5.61×10^{-5}
$\chi^2_{re}(run)$	9.44×10^{1}	3.42×10^{1}	2.53×10^{1}	5.56×10^{0}
$\overline{\chi^2_{re}(bunch)}$	3.08×10^{3}	2.05×10^{2}	1.28×10^{2}	2.36×10^{1}
Syst.Pattern	3.00×10^{-3}	1.08×10^{-3}	7.34×10^{-4}	3.69×10^{-4}

Table 6.2: Run13 summary of corrections on scaler counts.

Chapter 7

A_{LL} Analysis

7.1 A_{LL} Calculation

A raw asymmetry, ε_{LL} is calculated for the red "peak" (112 MeV/c^2 < $M_{\gamma\gamma}$ <162 MeV/c^2) and blue "sideband" (47 MeV/c^2 < $M_{\gamma\gamma}$ <97 MeV/c^2 and 177 MeV/c^2 < $M_{\gamma\gamma}$ <217 MeV/c^2) regions using Eq. 4.4 on a run-by-run basis, for 14 P_T bins. (See Fig. 4.1) Corresponding polarizations for that a run are then used to turn the ε_{LL} into A_{LL}. Polarization values are summarized in Fig. 2.7 and Fig. 2.8.

As discussed in Subsubsec. 3.6.3, the analysis is carried out separately for even and odd crossing. Run-by-run $A_{LL}^{\pi^0+BG}$ is calculated with "peak" region yields for odd and even bunches. Similarly, A_{LL}^{BG} is calculated with "sideband" region yields from odd and even bunches.

Once run-by-run $A_{LL}^{\pi^0+BG}$s and A_{LL}^{BG}s are obtained, constant fittings are done on the run-by-run $A_{LL}^{\pi^0+BG}$s and A_{LL}^{BG}s to obtain average $A_{LL}^{\pi^0+BG}$s and A_{LL}^{BG}s. The fittings are done spin patterns separately to avoid fake asymmetry from ghost clusters as discussed in Subsec. 7.2.1. Run12 run-by-run $A_{LL}^{\pi^0+BG}$s and A_{LL}^{BG}s and the fitting results are shown in Fig. 7.1, Fig. 7.2, Fig. 7.3 and Fig. 7.4. Run13 run-by-run $A_{LL}^{\pi^0+BG}$s and A_{LL}^{BG}s and the fitting results are shown in Fig. 7.7, Fig. 7.8, Fig. 7.9, and Fig. 7.10.

With the fitting results, A_{LL}s as function of $\langle P_T \rangle$ are drawn. Fig. 7.5 and Fig. 7.6 show $A_{LL}^{\pi^0+BG}$ and A_{LL}^{BG} as function of $\langle P_T \rangle$ for Run12. Fig. 7.11 and Fig. 7.12 show the $A_{LL}^{\pi^0+BG}$ and A_{LL}^{BG} curves for Run13.

Then physics asymmetries, $A_{LL}^{\pi^0}$s are obtained by using Eq. 4.6 and background fraction obtained in Subsec. 7.1.5. For Run12, Fig 7.17 shows the results and for Run13, Fig 7.18 shows the results.

7.1.1 Statistics Requirement for A_{LL} Calculation

To assure that there are enough statistics to assume Gaussian uncertainties in the calculation, minimum statistics are required. For the "peak" region calculation, runs where

$$N_{++} + N_{+-} < 10 \tag{7.1}$$

for a given (crossing, P_T) bin are excluded from the analysis for that bin. The requirement is applied in this way so that N_{++} and N_{+-} would have enough counts each and be distributed according to Gaussian statistics. Actually the requirement may not enough for the approximation. However to save statistics, the condition is compromised.

N_{++} and N_{+-} are not counted separately such as $N_{++} < 5||N_{+-} < 5$ because it would introduce bias because it would increase the magnitude of any asymmetry when the yields were near the threshold.

For the "sideband" region calculation, the condition for exclusion is

$$N_{++} < 1||N_{+-} < 1 \tag{7.2}$$

in order to avoid divide-by-zero in uncertainty calculations.

7.1.2 Choice of P_T Bins

The asymmetries are calculated in 14 P_T bins: 2.0-2.5, 2.5-3.0, 3.0-3.5, 3.5-4.0, 4.0-4.5, 4.5-5.0, 5.0-6.0, 6.0-7.0, 7.0-8.0, 8.0-9.0, 9.0-10.0, 10.0-12.0, 12.0-15.0, 15.0-20.0 GeV/c.

Note that higher P_T bins are 2, 3 or 5 GeV/c wide, in order for most of the runs to pass the statistics cut described in Subsec. 7.1.1.

The average $P_T^{\pi^0}$ in each P_T bin is is calculated from $\langle P_T \rangle$ in peak region and sidebands by using Eq. 7.3.

$$\langle P_T^{\pi^0} \rangle = \frac{\langle P_T^{\pi^0+BG} \rangle - r\langle P_T^{BG} \rangle}{1-r} \tag{7.3}$$

here r is background contribution obtained in Subsec. 7.1.5. The mean P_T values are summarized in Tab. 7.1.

7.1.3 Relative Luminosity

Relative luminosity is calculated as the ratio between BBCLL1 trigger counts in same helicity crossing to the number in opposite helicity crossing. The trigger counts are from the Star scaler basically because Star scaler gives much more information, especially clock trigger counts and no vertex$_z$ cut scaler counts that those facilitate corrections on scaler count such as pileup correction and residual rate correction. However, for Run13, Star scaler had not been setup until run number 386946 and GL1p scaler is used for those initial runs of Run13.

Pileup and residual rate correction should be applied to correct scaler miscount by piled event, single-side event and effect of vertex cut. Thus scaler counts with pileup and residual rate correction are used to calculate relative luminosity. For initial runs of Run13 which have been taken without proper Star scaler setup, no scaler corrections are considered because GL1p don't give enough information for the correction. However, as the effect of the corrections on relative luminosity is not significant, choice of scaler and correction don't affect physics results much.

Relative luminosity as function of run number is shown in Fig. 6.1 and Fig. 6.2.

P_T bin (GeV/c)	$\langle P_T \rangle$ (Run12)	$\langle P_T \rangle$ (Run13)	$\langle P_T \rangle$ (Comb.)
2.0-2.5	2.2757e+0	2.2801e+0	2.2795e+0
2.5-3.0	2.7618e+0	2.7627e+0	2.7626e+0
3.0-3.5	3.2516e+0	3.2507e+0	3.2508e+0
3.5-4.0	3.7458e+0	3.7440e+0	3.7442e+0
4.0-4.5	4.2415e+0	4.2401e+0	4.2403e+0
4.5-5.0	4.7387e+0	4.7378e+0	4.7379e+0
5.0-6.0	5.4475e+0	5.4460e+0	5.4462e+0
6.0-7.0	6.4458e+0	6.4454e+0	6.4454e+0
7.0-8.0	7.4445e+0	7.4454e+0	7.4452e+0
8.0-9.0	8.4470e+0	8.4471e+0	8.4472e+0
9.0-10.	9.4507e+0	9.4512e+0	9.4511e+0
10.-12.	1.0824e+1	1.0824e+1	1.0824e+1
12.-15.	1.3140e+1	1.3140e+1	1.3140e+1
15.-20.	1.6615e+1	1.6627e+1	1.6624e+1

Table 7.1: Mean P_T for each P_T bin. The fourth column is mean P_T of Run12 and Run13 combined data.

7.1.4 Statistical Uncertainty of A_{LL}

Statistical uncertainty in run-by-run A_{LL} is

$$\begin{aligned}(\Delta A_{LL})^2 =& \left(\frac{1}{P_B P_Y}\frac{2RN_{++}N_{+-}}{(N_{++}+RN_{+-})^2}\right)^2\Big(\big(\frac{\Delta N_{++}}{N_{++}}\big)^2+\big(\frac{\Delta N_{+-}}{N_{+-}}\big)^2+\big(\frac{\Delta R}{R}\big)^2\Big) \\ &+\Big(\big(\frac{\Delta P_B}{P_B}\big)^2+\big(\frac{\Delta P_Y}{P_Y}\big)^2\Big)A_{LL}^2\end{aligned} \tag{7.4}$$

The uncertainty in the γ pair yield, $\Delta N_{\gamma\gamma}$ is not simply $\sqrt{\Delta N_{\gamma\gamma}}$ as there may be more than one di-photon pair per event in the specified mass range. [45] The number of recorded γ pair yield, $N_{\gamma\gamma}$ fluctuates due to fluctuations of not only the number of recorded events, N_{ev} but also the multiplicity per event, k.

$$\begin{aligned}N_{\gamma\gamma} &= N_{ev}\bar{k} \\ \sigma^2_{N_{\gamma\gamma}} &= \sigma^2_{N_{ev}}\bar{k}^2 + N_{ev}^2\sigma^2_{\bar{k}}\end{aligned} \tag{7.5}$$

Since N_{ev} is Poisson distributed, $\sigma^2_{N_{ev}} = N_{ev}$. Also $\sigma^2_{\bar{k}} = \frac{1}{N_{ev}}\sigma^2_k$. Then,

$$\begin{aligned}\sigma^2_{N_{\gamma\gamma}} &= N_{ev}(\bar{k}^2+\sigma^2_k) \\ &= N_{ev}\overline{k^2} \\ &= N_{\gamma\gamma}\frac{\overline{k^2}}{\bar{k}}\end{aligned} \tag{7.6}$$

Thus,

$$\sigma_{N_{\gamma\gamma}} = \sqrt{\frac{\overline{k^2}}{\overline{k}} N_{\gamma\gamma}} \tag{7.7}$$

is obtained. Because of multiplicity, the additional factor $\frac{\overline{k^2}}{\overline{k}}$ appears. The factor is called the enhancement factor, k_{en} because it enhances uncertainty.

Tab. 7.2 lists the value of k_{en}^2 for each P_T bin of $N_{\pi^0+BG.}$ and $N_{BG.}$ for Run12 data. Tab. 7.3 is the table for Run13.

P_T (GeV)	k_{en}^2 P, E	k_{en}^2 S, E	k_{en}^2 P, O	k_{en}^2 S, O
2.0-2.5	1.0591	1.1266	1.0592	1.1222
2.5-3.0	1.0438	1.1077	1.0440	1.1066
3.0-3.5	1.0358	1.0975	1.0353	1.0979
3.5-4.0	1.0303	1.0908	1.0303	1.0892
4.0-4.5	1.0265	1.0830	1.0259	1.0845
4.5-5.0	1.0222	1.0775	1.0221	1.0771
5.0-6.0	1.0325	1.1148	1.0325	1.1130
6.0-7.0	1.0247	1.1007	1.0249	1.1013
7.0-8.0	1.0217	1.0925	1.0205	1.0879
8.0-9.0	1.0176	1.0790	1.0172	1.0798
9.0-10.	1.0157	1.0757	1.0162	1.0754
10.-12.	1.0227	1.0965	1.0265	1.1065
12.-15.	1.0297	1.1243	1.0263	1.1014
15.-20.	1.0318	1.1108	1.0301	1.0947

Table 7.2: k_{en}^2 of Run12. Second column: peak region of even crossing. Third column: side region of even crossing. Fourth column: peak region of odd crossing. Fifth column: side region of odd crossing.

7.1.5 Background Fraction Estimation

Background fraction is background fraction in "peak" region. Background fraction is defined as Eq. 7.8.

$$r = \frac{\int_{m_1}^{m_2} \text{distribution describing background spectrum}}{\int_{m_1}^{m_2} \text{di-photon invariant mass spectrum}} \tag{7.8}$$

, where m_1 is 112 MeV and m_2 is 162 MeV. ("peak" region) Thus the distribution describing background spectrum is needed to be estimated.

To do this, regression with Gaussian processes (GPR) is used. Because no functional form is needed to be assumed in GPR, using GPR is safe way not to suffer from error from choosing wrong functional form describing background spectrum. Also it is second advantage of GPR that GPR gives uncertainty band of estimated distribution. To

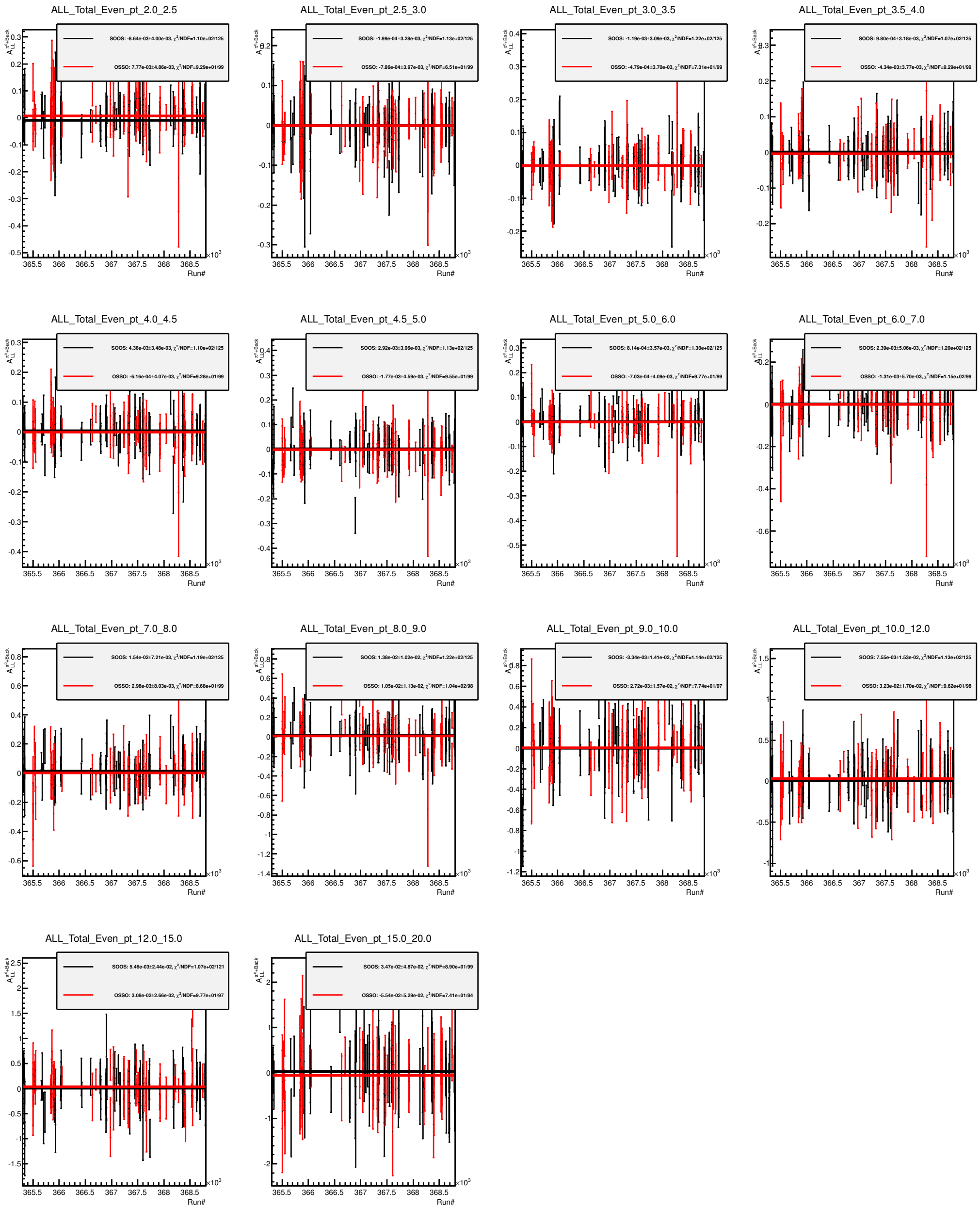

Figure 7.1: Run12 $A_{LL}^{\pi^0+BG}$ measured using Eq. 4.4 vs. runnumber in even crossings for various P_T bins. A constant is fit on the $A_{LL}^{\pi^0+BG}$ of each spin pattern.

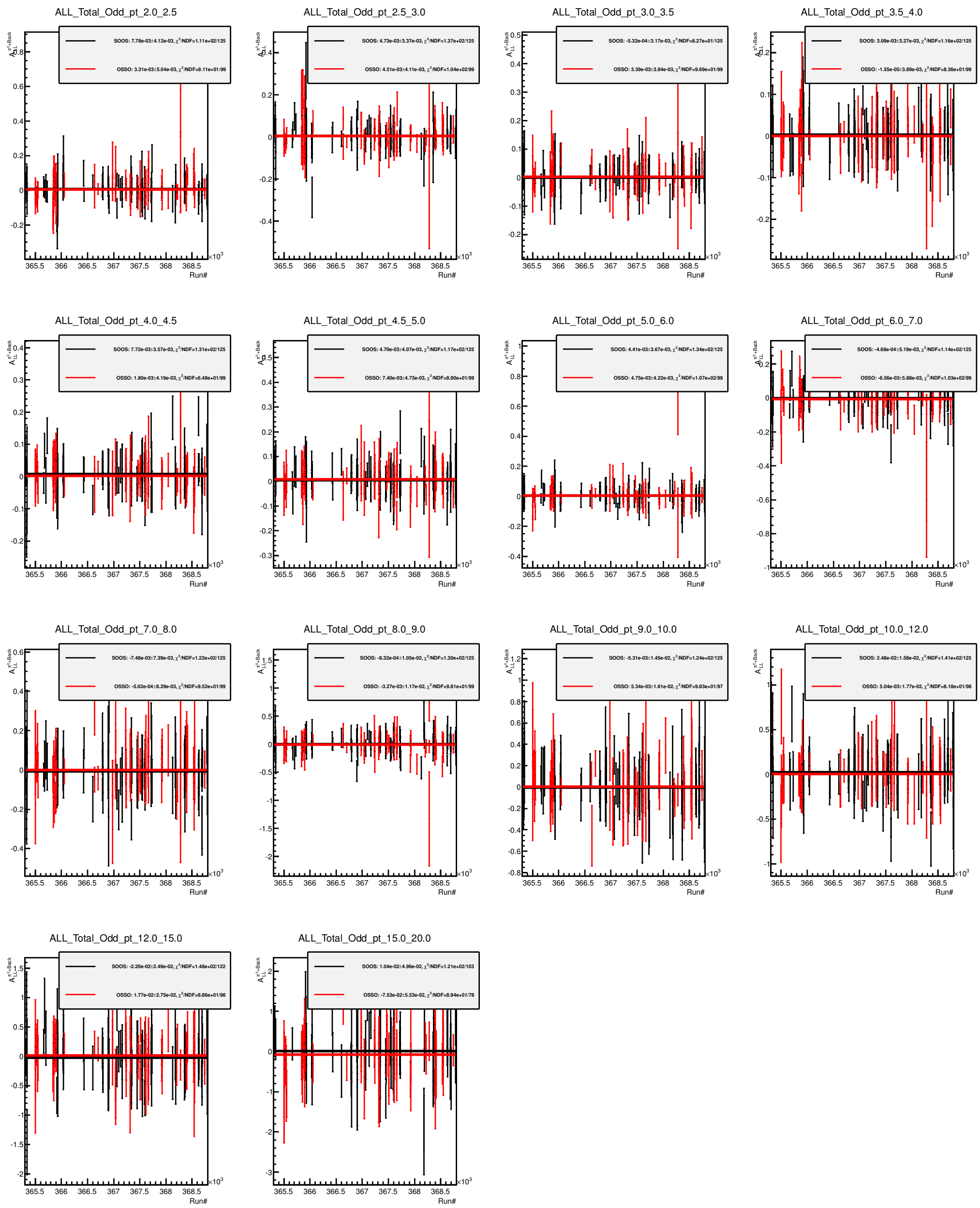

Figure 7.2: Run12 $A_{LL}^{\pi^0+BG}$ measured using Eq. 4.4 vs. runnumber in odd crossings for various P_T bins. A constant is fit on the $A_{LL}^{\pi^0+BG}$ of each spin pattern.

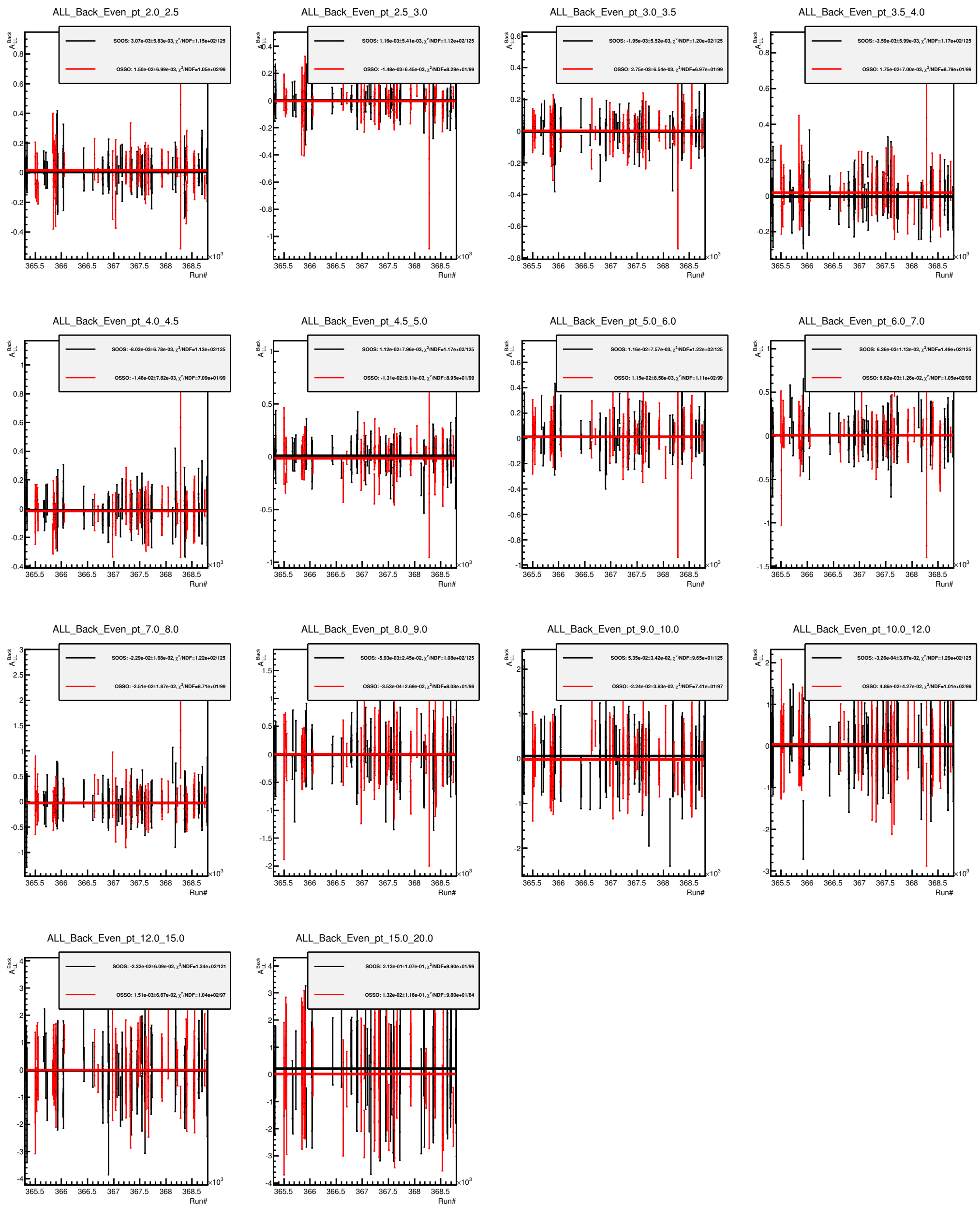

Figure 7.3: Run12 A_{LL}^{BG} measured using Eq. 4.4 vs. runnumber in even crossings for various P_T bins. A constant is fit on the A_{LL}^{BG} of each spin pattern.

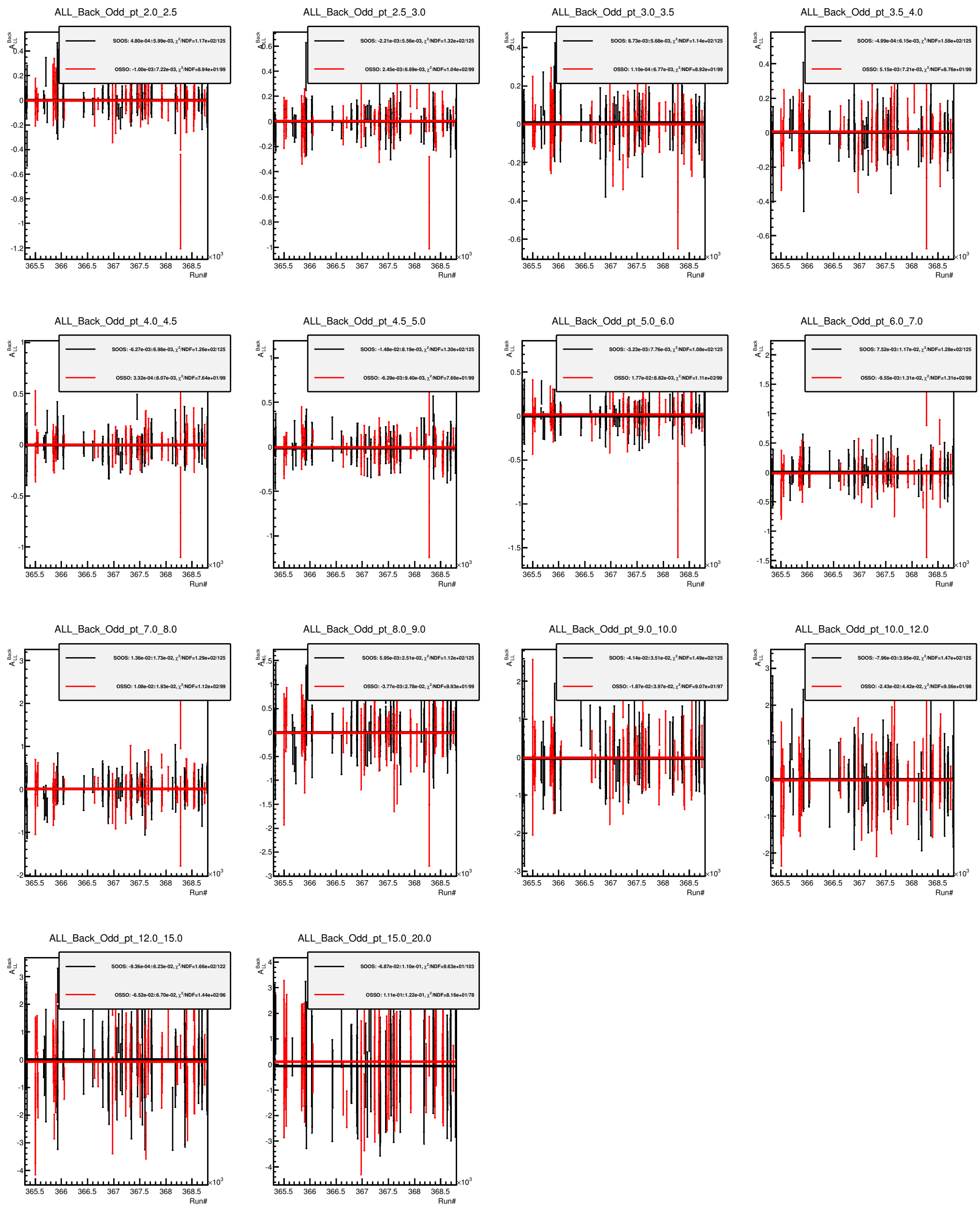

Figure 7.4: Run12 A_{LL}^{BG} measured using Eq. 4.4 vs. runnumber in odd crossings for various P_T bins. A constant is fit on the A_{LL}^{BG} of each spin pattern.

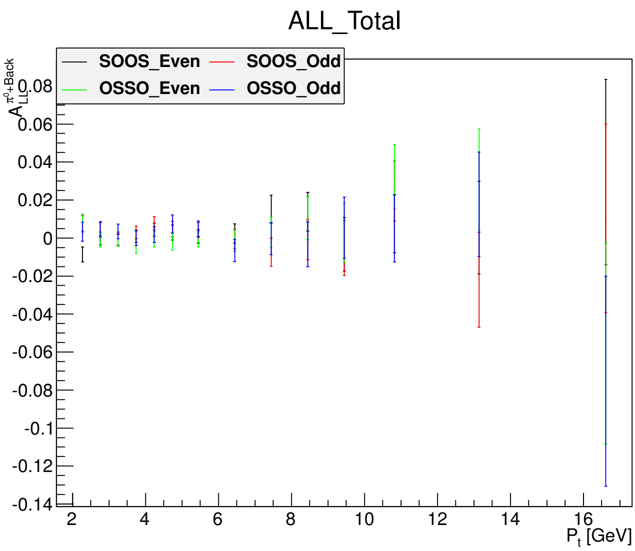

Figure 7.5: Run12 $A_{LL}^{\pi^0+BG}$ vs. P_T for even/odd crossings and spin patterns.

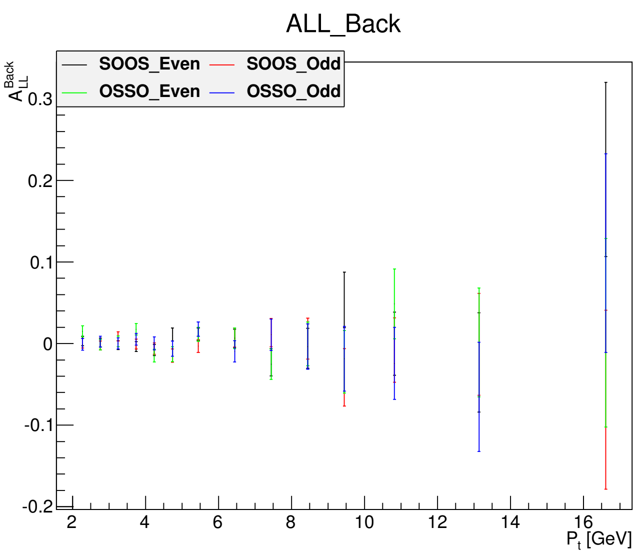

Figure 7.6: Run12 A_{LL}^{BG} vs. P_T for even/odd crossings and spin patterns

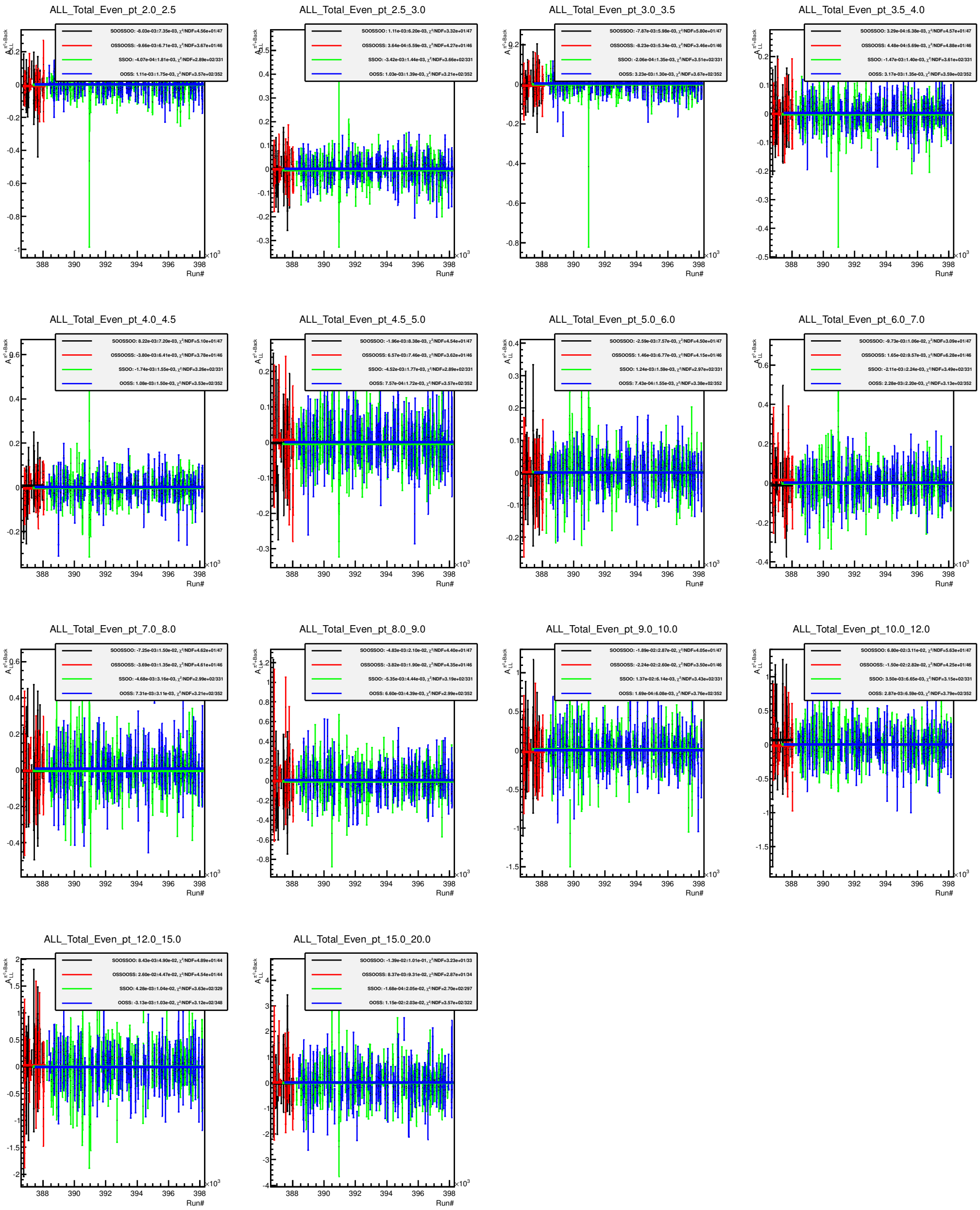

Figure 7.7: Run13 $A_{LL}^{\pi^0+BG}$ measured using Eq. 4.4 vs. runnumber in even crossings for various P_T bins. A constant is fit on the $A_{LL}^{\pi^0+BG}$ of each spin pattern.

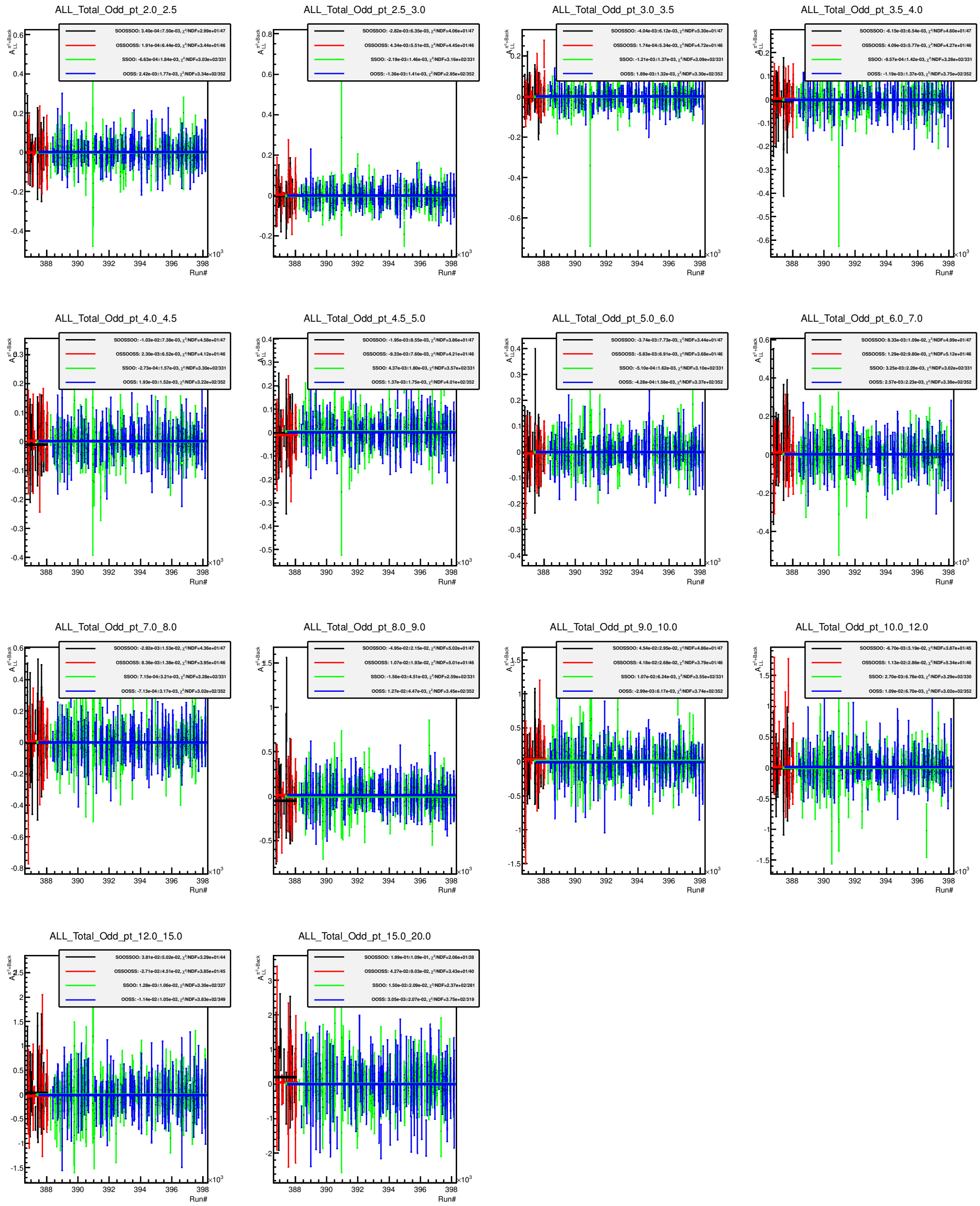

Figure 7.8: Run13 $A_{LL}^{\pi^0+BG}$ measured using Eq. 4.4 vs. runnumber in odd crossings for various P_T bins. A constant is fit on the $A_{LL}^{\pi^0+BG}$ of each spin pattern.

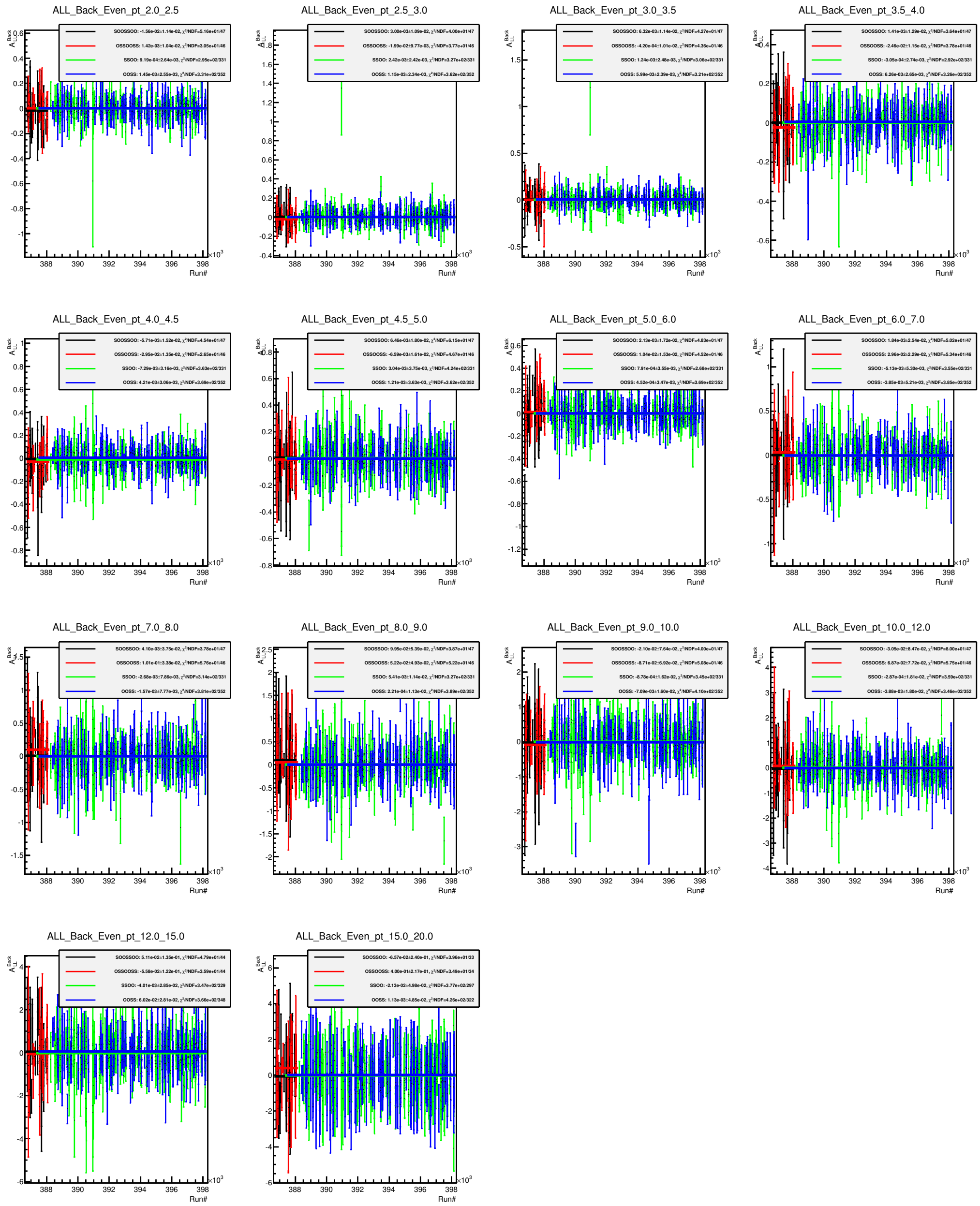

Figure 7.9: Run13 A_{LL}^{BG} measured using Eq. 4.4 vs. runnumber in even crossings for various P_T bins. A constant is fit on the A_{LL}^{BG} of each spin pattern.

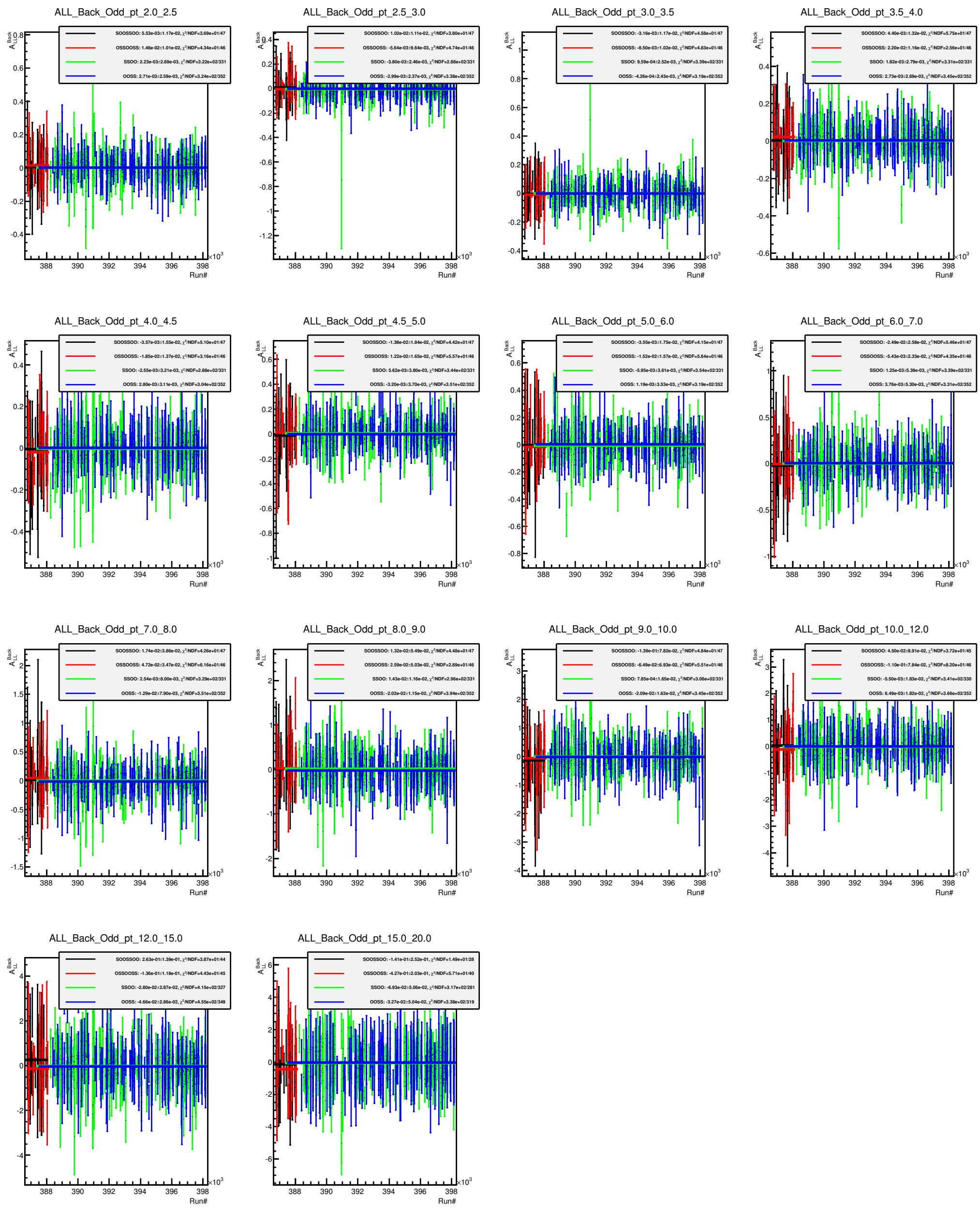

Figure 7.10: Run13 A_{LL}^{BG} measured using Eq. 4.4 vs. runnumber in odd crossings for various P_T bins. A constant is fit on the A_{LL}^{BG} of each spin pattern.

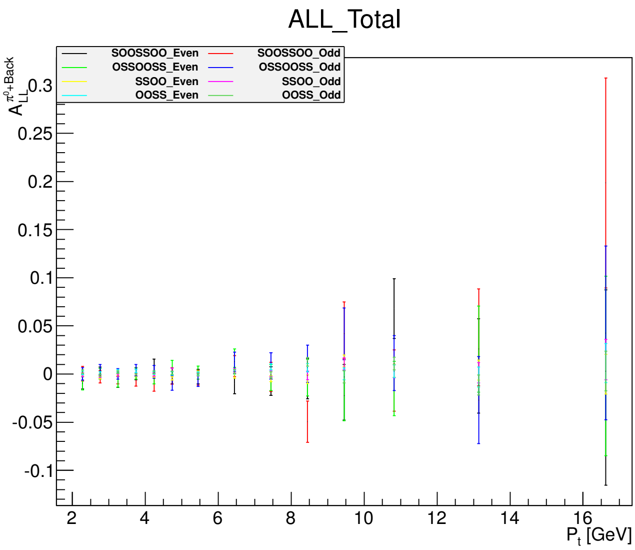

Figure 7.11: Run13 $A_{LL}^{\pi^0+BG}$ vs. P_T for even/odd crossings and spin patterns.

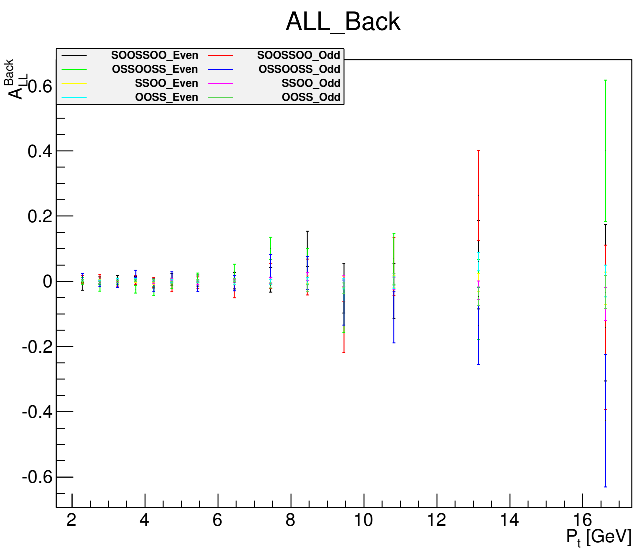

Figure 7.12: Run13 A_{LL}^{BG} vs. P_T for even/odd crossings and spin patterns

P_T (GeV)	k_{en}^2 P, E	k_{en}^2 S, E	k_{en}^2 P, O	k_{en}^2 S, O
2.0-2.5	1.0581	1.1200	1.0582	1.1247
2.5-3.0	1.0461	1.1064	1.0463	1.1029
3.0-3.5	1.0369	1.0905	1.0373	1.0904
3.5-4.0	1.0295	1.0815	1.0296	1.0810
4.0-4.5	1.0243	1.0716	1.0239	1.0720
4.5-5.0	1.0197	1.0661	1.0195	1.0661
5.0-6.0	1.0277	1.0999	1.0275	1.0994
6.0-7.0	1.0205	1.0865	1.0210	1.0884
7.0-8.0	1.0168	1.0766	1.0171	1.0787
8.0-9.0	1.0147	1.0709	1.0146	1.0691
9.0-10.	1.0132	1.0664	1.0131	1.0660
10.-12.	1.0198	1.0943	1.0209	1.0944
12.-15.	1.0230	1.0877	1.0231	1.0945
15.-20.	1.0291	1.1030	1.0269	1.0987

Table 7.3: k_{en}^2 of Run13. Second column: peak region of even crossing. Third column: side region of even crossing. Fourth column: peak region of odd crossing. Fifth column: side region of odd crossing.

apply GPR, framework of [46] is used. Input regions of interpolation are 67-87 MeV/c^2 and 187-212MeV/c^2. To avoid the input regions are contaminated by π^0 signal, the inner region of the interpolation is fixed to be far five sigmas away. The outer region of the interpolation is fixed to avoid "peak" structure of background in low mass region, especially at low P_T bins.

The results of GPR for estimating background distribution are summarized in Fig. 7.13, Fig. 7.14, Fig. 7.15 and Fig. 7.16.

7.2 Systematic Uncertainties

7.2.1 False Asymmetry in Background due to Ghost Clusters: Low P_T

It has been reported that there might be some systematic difference between the different spin pattern in the run-by-run A_{LL}s especially at low P_T. [47] The effect is more emerged in the sideband region than signal region. We attribute this effect to the way in which the EMCal stores energy information. As discussed in Subsubsec. 5.3.2, clusters may survive up to three crossings. The survived clusters make combinatorial background. The combinatorial background may depend spin patterns. Thus false asymmetry may occur due to the ghost cluster.

Let's think simple deduction to explain how the combinatorial background have the dependency. Let's define N_r which is the average number of real clusters and N_g which is the average number of ghost clusters. After abort gap, for ith bunch, the number of

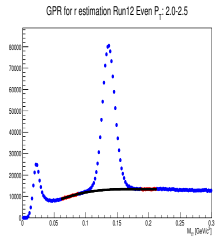

(a) P_T: 2.0-2.5

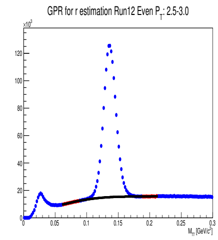

(b) P_T: 2.5-3.0

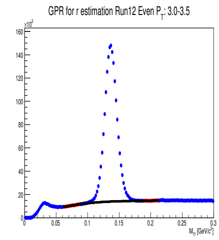

(c) P_T: 3.0-3.5

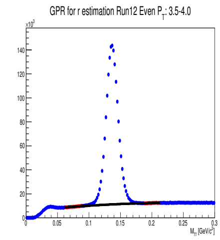

(d) P_T: 3.5-4.0

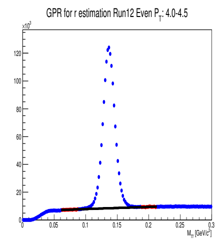

(e) P_T: 4.0-4.5

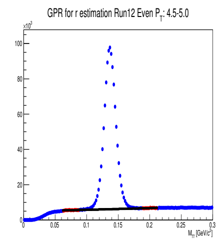

(f) P_T: 4.5-5.0

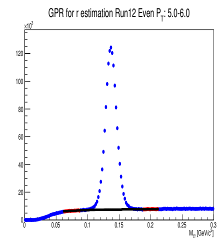

(g) P_T: 5.0-6.0

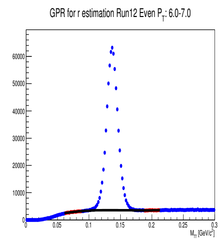

(h) P_T: 6.0-7.0

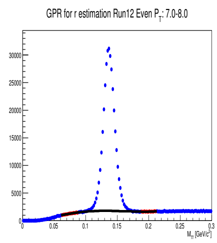

(i) P_T: 7.0-8.0

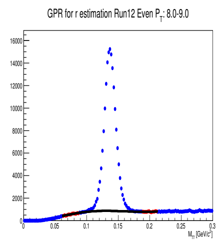

(j) P_T: 8.0-9.0

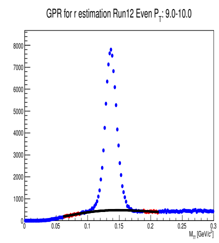

(k) P_T: 9.0-10.0

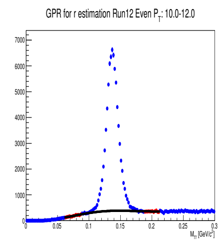

(l) P_T: 10.0-12.0

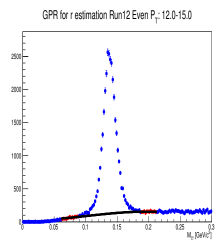

(m) P_T: 12.0-15.0

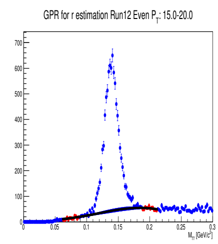

(n) P_T: 15.0-20.0

Figure 7.13: GPR results of Run12 even crossing for background fraction estimation. Red points are used for GPR.

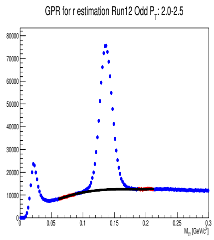

(a) P_T: 2.0-2.5

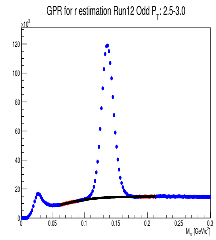

(b) P_T: 2.5-3.0

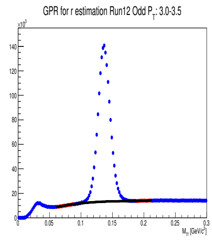

(c) P_T: 3.0-3.5

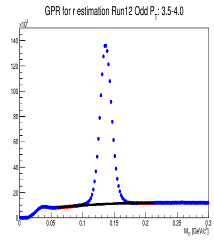

(d) P_T: 3.5-4.0

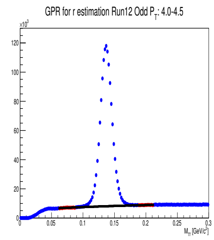

(e) P_T: 4.0-4.5

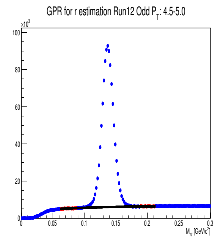

(f) P_T: 4.5-5.0

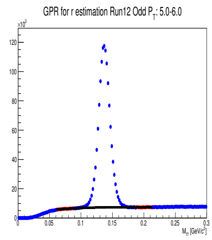

(g) P_T: 5.0-6.0

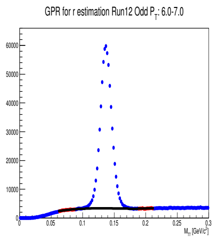

(h) P_T: 6.0-7.0

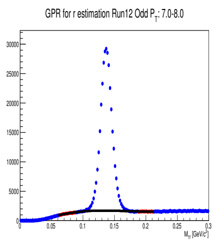

(i) P_T: 7.0-8.0

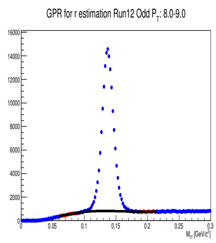

(j) P_T: 8.0-9.0

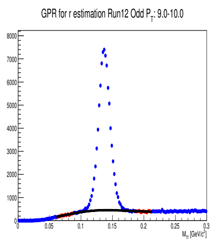

(k) P_T: 9.0-10.0

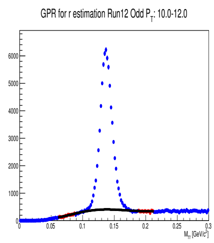

(l) P_T: 10.0-12.0

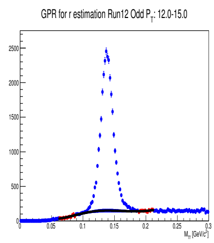

(m) P_T: 12.0-15.0

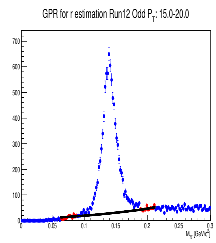

(n) P_T: 15.0-20.0

Figure 7.14: GPR results of Run12 odd crossing for background fraction estimation. Red points are used for GPR.

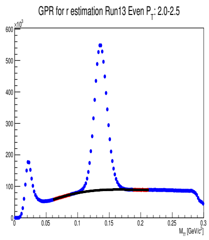

(a) P_T: 2.0-2.5

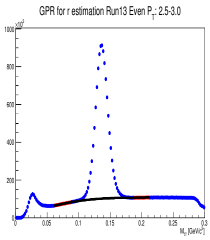

(b) P_T: 2.5-3.0

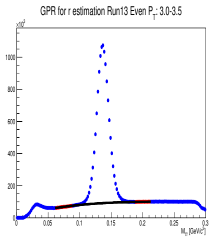

(c) P_T: 3.0-3.5

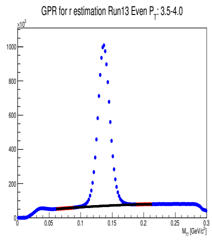

(d) P_T: 3.5-4.0

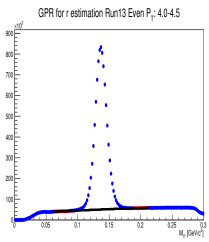

(e) P_T: 4.0-4.5

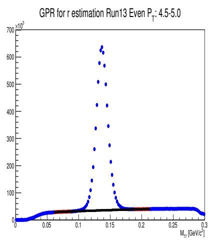

(f) P_T: 4.5-5.0

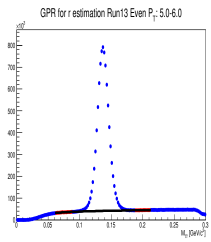

(g) P_T: 5.0-6.0

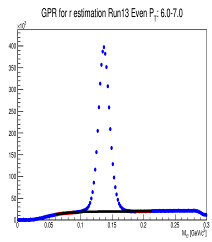

(h) P_T: 6.0-7.0

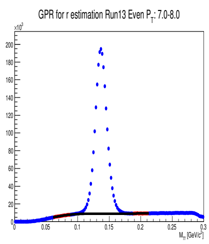

(i) P_T: 7.0-8.0

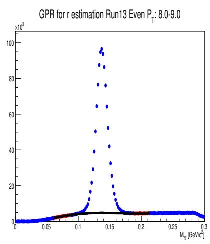

(j) P_T: 8.0-9.0

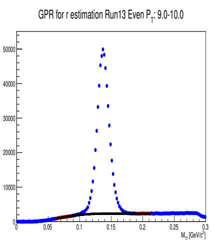

(k) P_T: 9.0-10.0

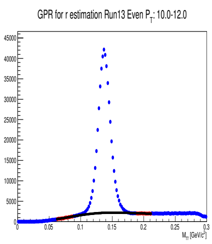

(l) P_T: 10.0-12.0

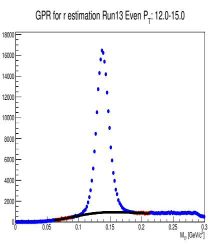

(m) P_T: 12.0-15.0

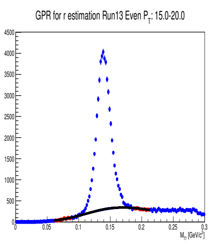

(n) P_T: 15.0-20.0

Figure 7.15: GPR results of Run13 even crossing for background fraction estimation. Red points are used for GPR.

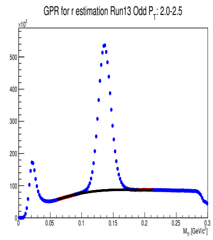

(a) P_T: 2.0-2.5

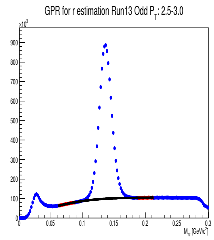

(b) P_T: 2.5-3.0

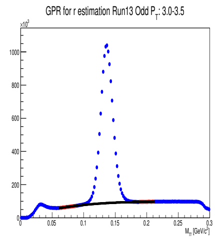

(c) P_T: 3.0-3.5

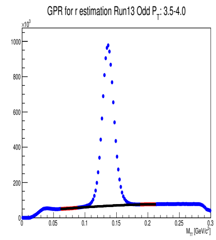

(d) P_T: 3.5-4.0

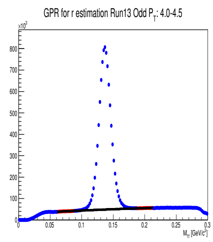

(e) P_T: 4.0-4.5

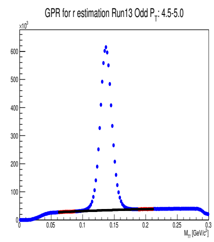

(f) P_T: 4.5-5.0

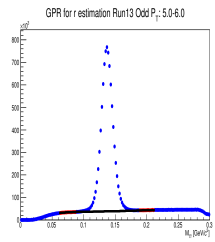

(g) P_T: 5.0-6.0

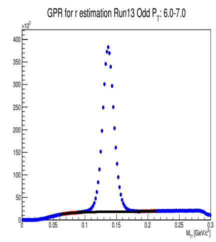

(h) P_T: 6.0-7.0

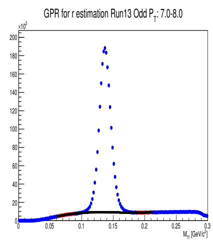

(i) P_T: 7.0-8.0

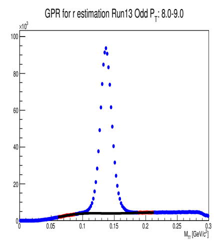

(j) P_T: 8.0-9.0

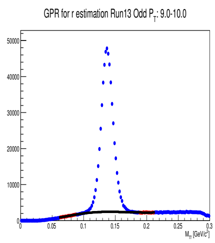

(k) P_T: 9.0-10.0

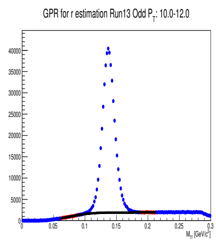

(l) P_T: 10.0-12.0

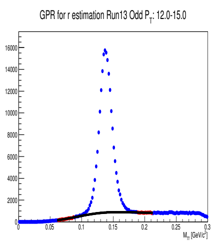

(m) P_T: 12.0-15.0

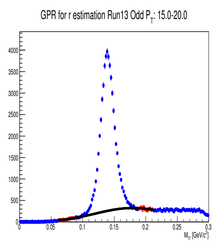

(n) P_T: 15.0-20.0

Figure 7.16: GPR results of Run13 odd crossing for background fraction estimation. Red points are used for GPR.

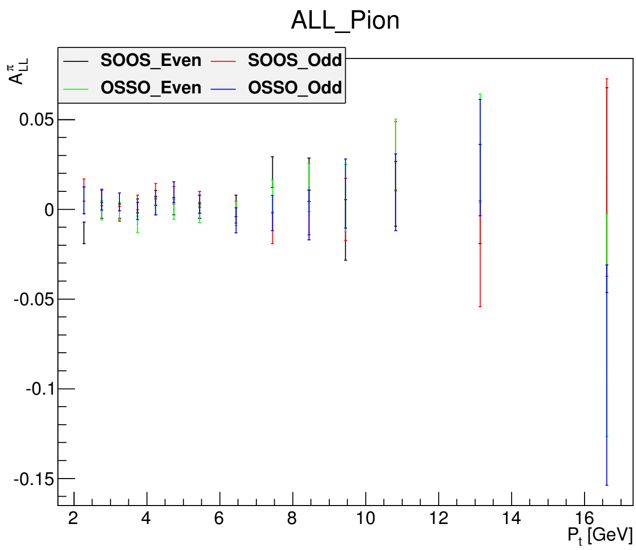

Figure 7.17: Run12 $A_{LL}^{\pi^0}$ vs. P_T for even/odd crossings and spin patterns

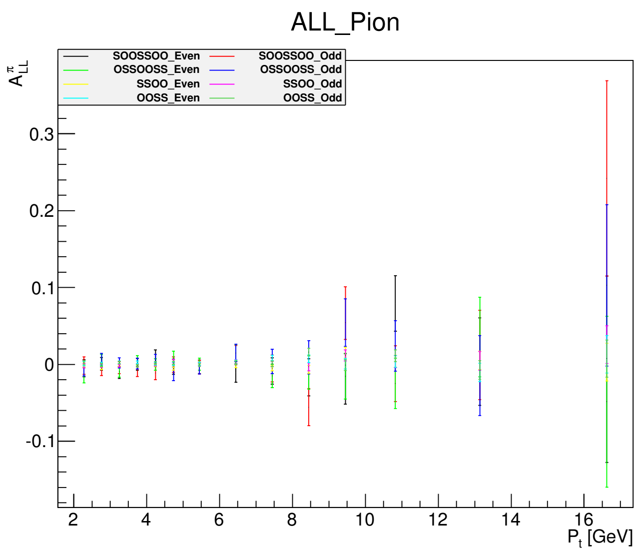

Figure 7.18: Run13 $A_{LL}^{\pi^0}$ vs. P_T for even/odd crossings and spin patterns

cluster, N_i is

$$\begin{aligned}
N_0 &= N_r \\
N_1 &= N_r + N_g \\
N_2 &= N_r + 2N_g \\
N_3 &= N_r + 3N_g \\
N_4 &= N_r + 3N_g \\
N_5 &= N_r + 3N_g \\
N_6 &= N_r + 3N_g \\
N_7 &= N_r + 3N_g \\
&\cdots
\end{aligned} \tag{7.9}$$

For the spin pattern "SOOS", the number of γ pair combinations in same helicity crossings is $\binom{N_r}{2} + \binom{N_r+3N_g}{2} + \binom{N_r+3N_g}{2} + \binom{N_r+3N_g}{2} \ldots$ and the number in opposite crossings is $\binom{N_r+N_g}{2} + \binom{N_r+2N_g}{2} + \binom{N_r+3N_g}{2} + \binom{N_r+3N_g}{2} + \ldots$. For the spin pattern "OSSO", the opposite situation happens. Because the γ pairs containing ghost cluster make combinatorial background, that's how ghost clusters make spin pattern dependent the combinatorial background. The effect has been noticeable since Run09 due to increased luminosity. Because luminosity was increased further in Run13, the effect becomes more important in Run13 analysis.

To avoid mixing false asymmetry, spin pattern separated analysis is done. By this way, it is ensured that A_{LL}^{BG} is subtracted from $A_{LL}^{\pi^0+BG}$ when $A_{LL}^{\pi^0}$ is calculated. In addition to the spin pattern separate analysis, ToF cut is required for both of clusters to reject the ghost cluster as discussed in Subsubsec 5.3.2.

With the ToF cut and after subtracting the sideband asymmetries, the results for $A_{LL}^{\pi^0}$ are consistent within statistical uncertainties.

7.2.2 Uncertainty of Relative Luminosity

As discussed in Chap. 6, the upper limit on the systematic uncertainty in $A_{LL}^{\pi^0}$ due to relative luminosity are $\Delta A_{LL}^{\pi^0}(RelLumi.) = 2.003 \times 10^{-4}$ for Run12 and $\Delta A_{LL}^{\pi^0}(RelLumi.) = 3.853 \times 10^{-4}$ for Run13. This systematic uncertainty applies globally to all P_T bins. This systematic uncertainty from relative luminosity is dominant systematic uncertainty of this analysis.

7.2.3 Global Scaling Uncertainty from Polarization

As discussed in Subsec. 2.3.1, the polarization group advises to use Run12 value for global systematic uncertainty on $P_B P_Y$ of 6.5%. As discussed in Sec. 3.5, additional uncertainty from polarization direction is negligible compared to the global scaling uncertainty of polarization. Thus the uncertainty from polarization direction is ignored. The uncertainty of polarization acts as global scaling uncertainty across all P_T.

7.2.4 Uncertainty of Background Fraction Estimation

Although GPR is best estimator for background fraction and we stick to the fraction obtained by GPR, the alternative way is also tried to estimate the fraction. The alternative way is assuming functional form of π^0 signal distribution and background distribution and fitting the di-photon invariant mass spectra. Traditionally Gaussian function is used to describe π^0 signal distribution and the third order polynomial function is used to describe background distribution. However Gaussian function can not describe signal distribution well, especially right tails of signal and peak. Thus the alternative function, the Voigt function is also tried. Fig. 7.19 shows example plots of the fitting results. To check dependence of fitting region, two different fitting regions are tried.

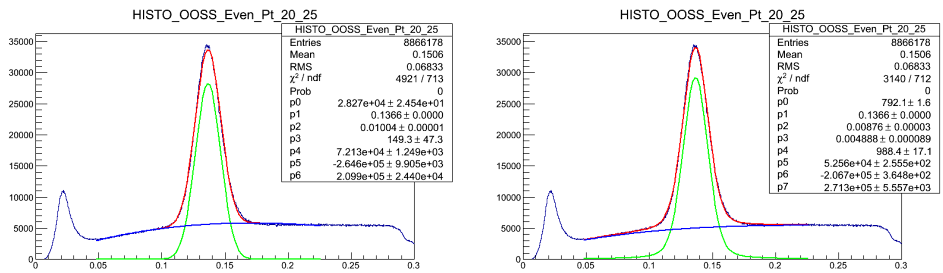

(a) Gaus+Pol3 (b) Voigt+Pol3

Figure 7.19: Example plots of the two fitting results.

As Fig. 7.20 and Fig 7.21 shows, the background fractions obtained by the five different ways are different systematically. Thus systematic uncertainty on $A_{LL}^{\pi^0}$ is assigned due to the background fractions.

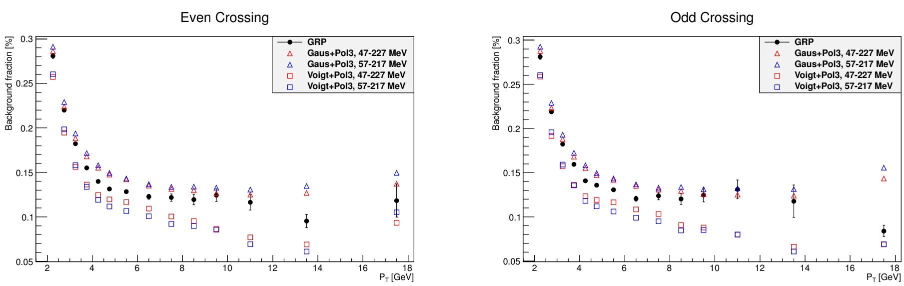

(a) Even (b) Odd

Figure 7.20: Run12 background fractions obtained by alternative ways.

To assign the systematic uncertainty, pattern-by-pattern and crossing-by-crossing background subtraction and average of $A_{LL}^{\pi^0}$s are repeated with the different backgrounds. Then the difference of $A_{LL}^{\pi^0}$ between maximum(minimum) $A_{LL}^{\pi^0}$ and $A_{LL}^{\pi^0}$ from GPR is assigned as systematic uncertainty. The systematic uncertainties are summarized in Tab. 8.3

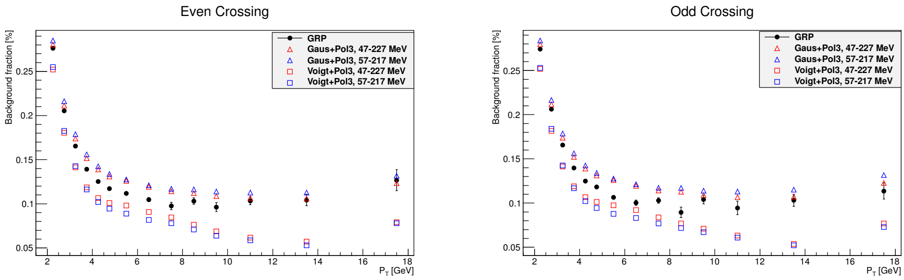

(a) Even (b) Odd

Figure 7.21: Run13 background fractions obtained by alternative ways.

7.3 Bunch Shuffling

Bunch Shuffling is a boot-strapping technique used to extract the statistical uncertainty on A_{LL} in a model independent way, i.e. no assumptions about underlying statistical distributions need to be assumed. The results of bunch shuffling can be checked to see if they agree with the result of the equations for calculating the uncertainty of A_{LL}, Eq. 7.4. The result of such a comparison could point to an unknown systematic uncertainty or overestimation of the statistical uncertainties.

7.3.1 Procedure

The spin pattern is completely randomized, separately for each fill, and then run-by-run A_{LL} is recalculated based on the random pattern. This procedure is repeated a large number of times, in this case 40,000. Inference can be obtained from the results of the 40,000 shuffles. No constraint on the number of "same" helicity bunches and "opposite" helicity bunches, so for example, just a few bunchs are assigned "same" helicity then the corresponding the relative luminosity would be < 0.1. Also statistics requirement of Eq. 7.1 is not applied for this bunch shuffling analysis. However Eq. 7.2 condition is applied for not only "peak" and "side" region to avoid not to divide by zero.

7.3.2 Bunch Shuffling Results

Statistical uncertainties from bunch shuffling are compared to those calculated from error propagation, Eq. 7.4 in each run by way of χ^2_{re} distribution. Specifically, A_{LL} and ΔA_{LL} are calculated with Eq. 4.4 and Eq. 7.4 and a constant functions are fit on the A_{LL}s vs. run, which gives one χ^2_{re} value per iteration of the bunch shuffling. 40,000 shuffles are iterated. Then it is check that the χ^2_{re} distribution agrees with the theoretical expectation.

The results of bunch shuffling are summarized in Fig. 7.22, Fig. 7.23, Fig. 7.24, and Fig. 7.23 for Run12 and Fig. 7.26, Fig. 7.27, Fig. 7.28, and Fig. 7.27 for Run13. Theoretical distributions are drawn by red line. Basically measured and theoretical distribution are matched. Mismatch at high P_T region occurs because of lack of statistics. As statistics is limited, Gaussian distribution approximation is failed and χ^2 distribution lose it's meaning. Also lack of statistics makes degree of freedom is fluctuating because the iteration is failed at Eq. 7.2, and makes width of measured χ^2_{re} distribution large. Thus the mismatch doesn't imply Eq. 7.4 is wrong.

The nice agreements assure that Eq. 7.4 is reasonable. Also it is checked that there is no unknown systematic uncertainties.

7.4 Single Spin Asymmetries, A_L

A single spin asymmetry is defined as

$$A_L \equiv \frac{\sigma_+ - \sigma_-}{\sigma_+ + \sigma_-} \tag{7.10}$$

, where $\sigma+$ (σ_-) is the cross section of positive (negative) helicity bunches for one beam (the other beam is summed over).

Because strong interaction is parity invariant, $A_L^{\pi^0}$ should be zero. Thus measuring $A_L^{\pi^0}$ and checking measured $A_L^{\pi^0}$ is really zero is another method of quality assurance the analysis.

Eq. 7.10 can be rewritten in terms of particle yield and luminosity with assumptions described in Sec. 4.1.

$$A_L = \frac{1}{P_{Beam}} \frac{N_+ - RN_-}{N_+ + RN_-}, \qquad where \quad R = \frac{L_+}{L_-} \tag{7.11}$$

where P_{Beam} is the polarization for that beam. The analysis procedures are similar to the those of A_{LL} analysis, with Eq. 7.11 substituted for Eq. 4.4.

Final results are give in Fig. 7.30 and Tab. 7.4 for Run12 and Fig. 7.31 and Tab.7.5 for Run13. It is checked that measured $A_L^{\pi^0}$s are zero within statistic uncertainty.

7.5 Parallel Cross-Check

This measurement is done by two analyzer independently, Hari Guarain[1] and Inseok Yoon[2]. The complete independent analysis is done from π^0 reconstruction. The cross-check results are listed in App. B. Perfectly consistent results assure the analysis is bug free.

[1] Geogia State University, USA.

[2] Seoul National University, Korea. The writer of the dissertation.

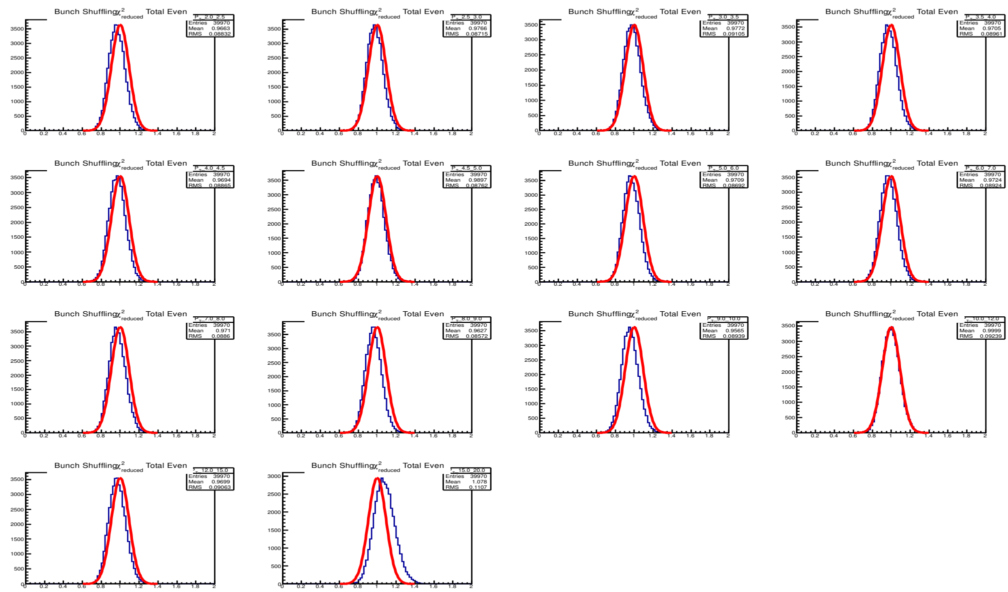

Figure 7.22: Run12 bunch shuffling χ^2_{re} distribution for “peak” region in even crossing, all spin patterns combined for various P_T bins. Theoretical distribution is drawn by red line.

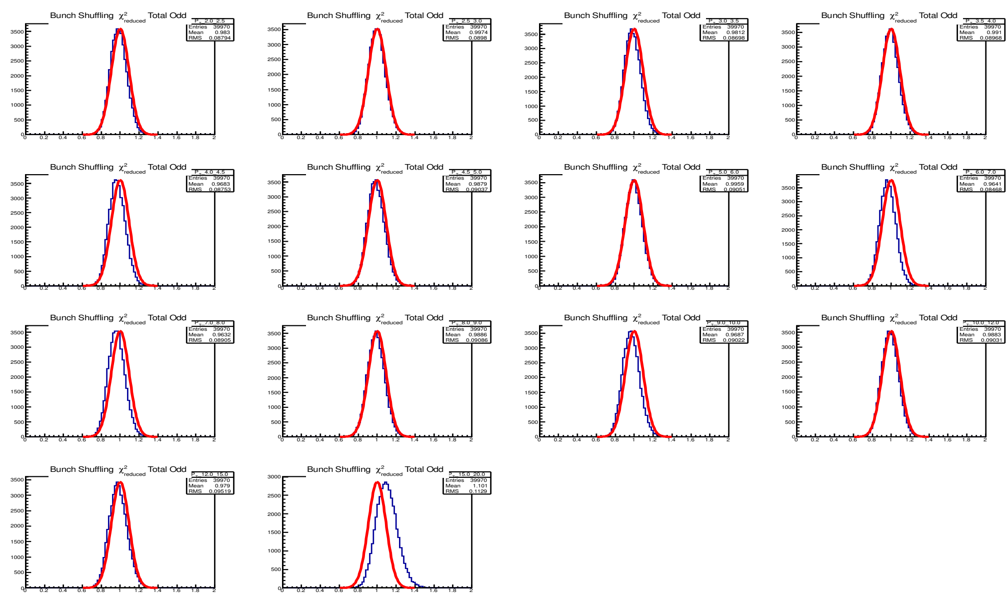

Figure 7.23: Run12 bunch shuffling χ^2_{re} distribution for “peak” region in odd crossing, all spin patterns combined for various P_T bins. Theoretical distribution is drawn by red line.

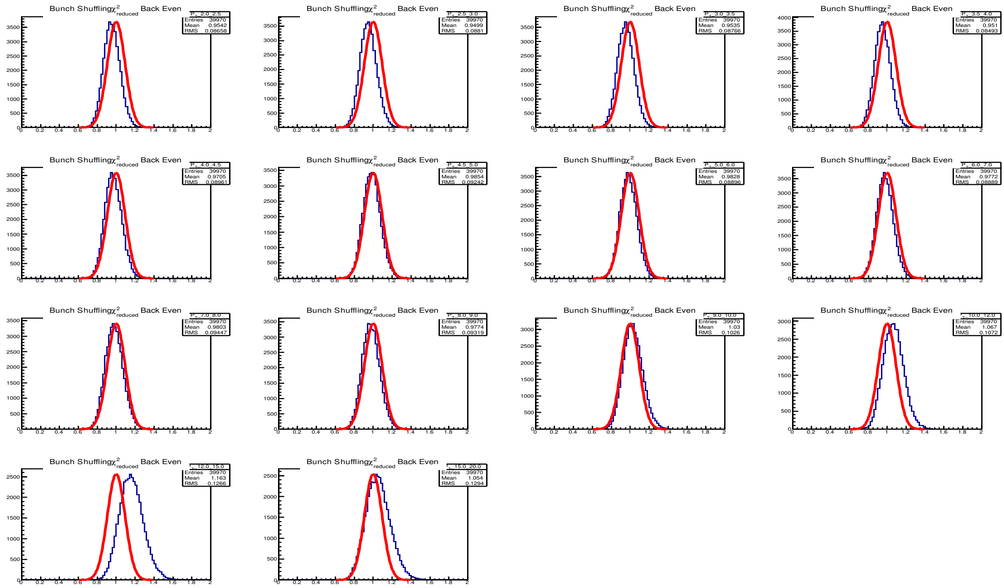

Figure 7.24: Run12 bunch shuffling χ^2_{re} distribution for “side” region in even crossing, all spin patterns combined for various P_T bins. Theoretical distribution is drawn by red line.

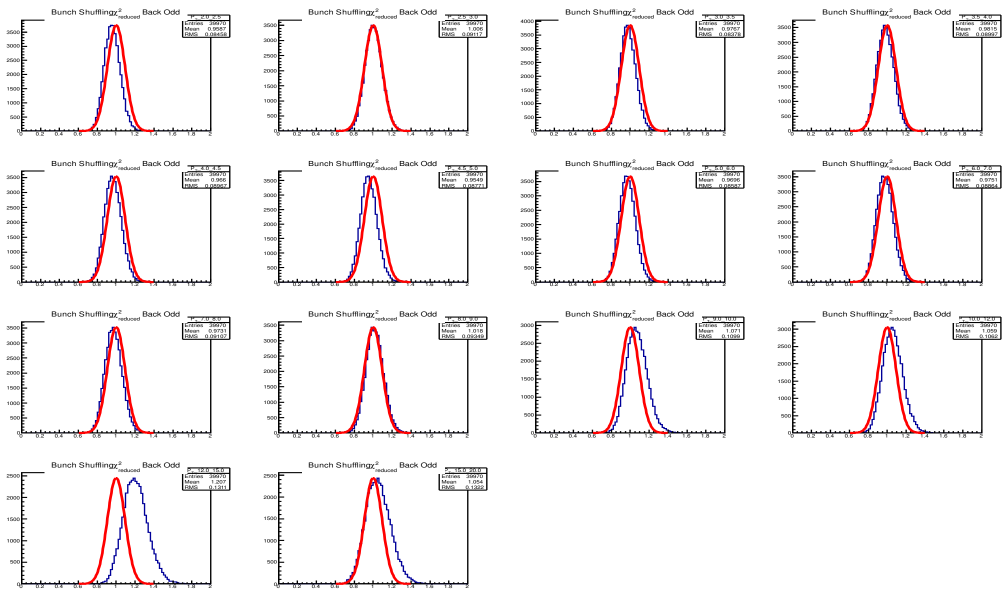

Figure 7.25: bunch shuffling χ^2_{re} distribution for “side” region in odd crossing, all spin patterns combined for various P_T bins. Theoretical distribution is drawn by red line.

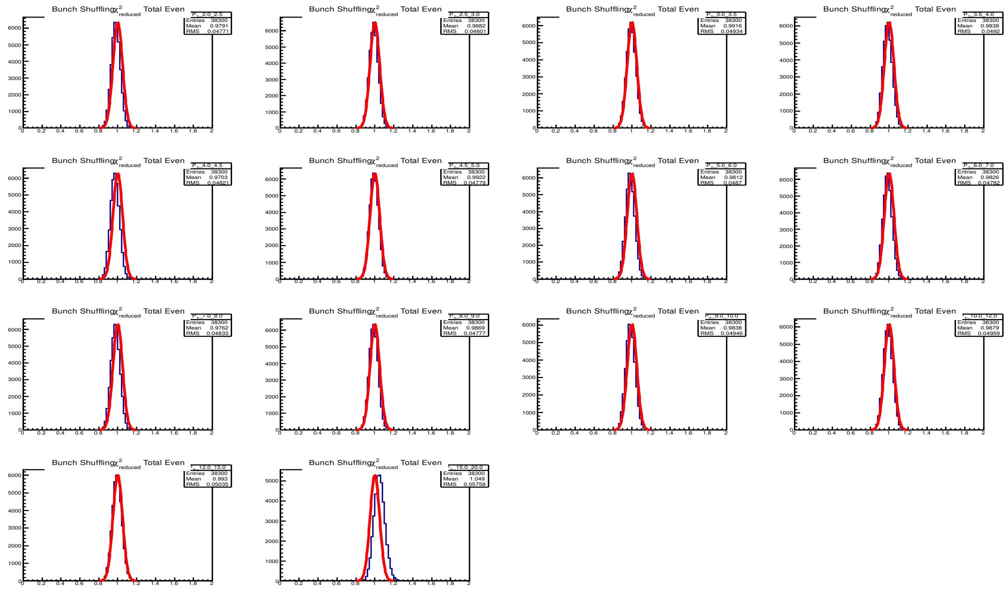

Figure 7.26: Run13 bunch shuffling χ^2_{re} distribution for "peak" region in even crossing, all spin patterns combined for various P_T bins. Theoretical distribution is drawn by red line.

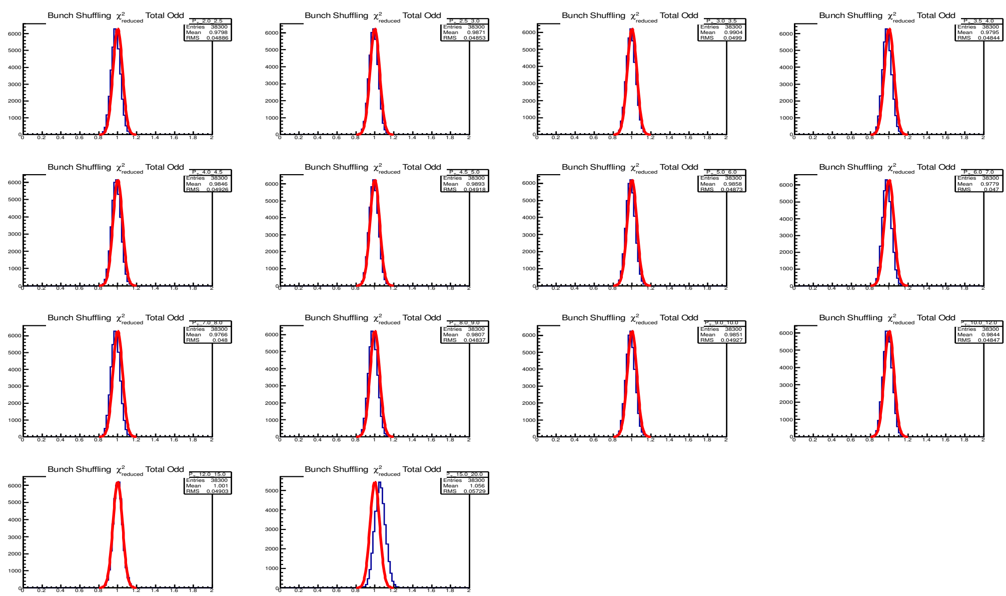

Figure 7.27: Run13 bunch shuffling χ^2_{re} distribution for "peak" region in odd crossing, all spin patterns combined for various P_T bins. Theoretical distribution is drawn by red line.

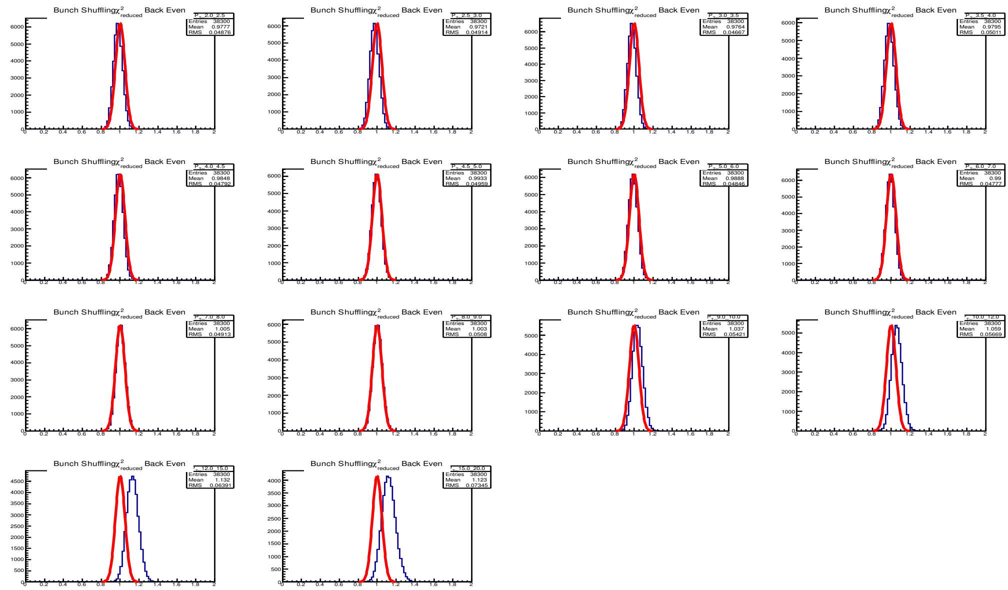

Figure 7.28: Run13 bunch shuffling χ^2_{re} distribution for “side” region in even crossing, all spin patterns combined for various P_T bins. Theoretical distribution is drawn by red line.

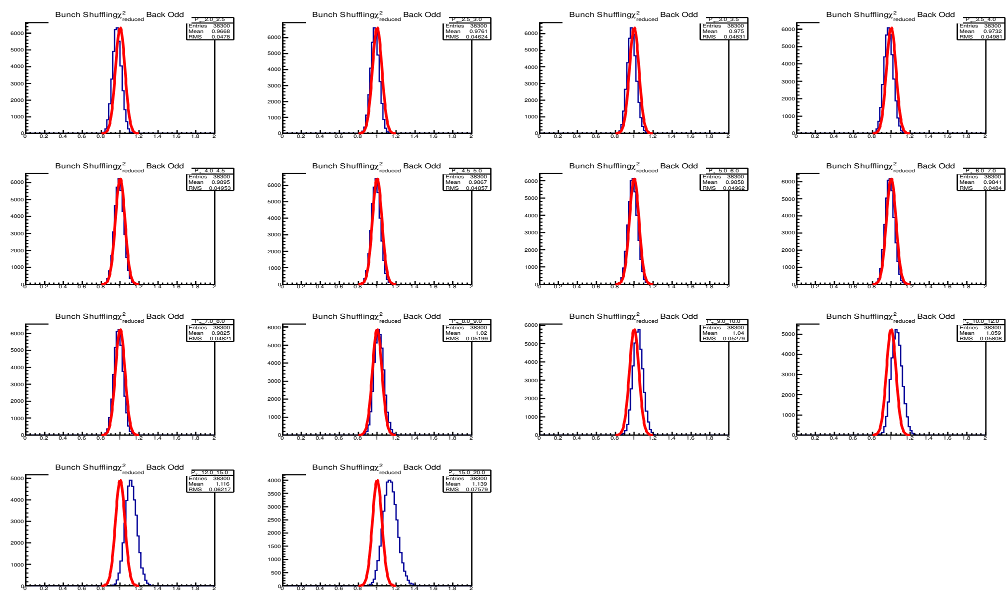

Figure 7.29: bunch shuffling χ^2_{re} distribution for “side” region in odd crossing, all spin patterns combined for various P_T bins. Theoretical distribution is drawn by red line.

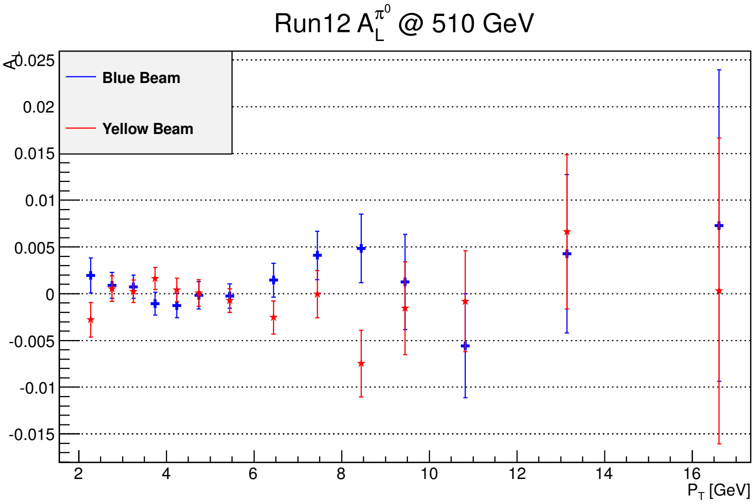

Figure 7.30: Run12 $A_L^{\pi^0}$ Result. Zero asymmetry is observed.

P_T	$A_L^{\pi^0}$(B)	$\Delta A_L^{\pi^0}$(B)	$A_L^{\pi^0}$(Y)	$\Delta A_L^{\pi^0}$(Y)
2.0-2.5	1.9367e-3	1.8773e-3	-2.7902e-3	1.8391e-3
2.5-3.0	8.8879e-4	1.3945e-3	5.3812e-4	1.3655e-3
3.0-3.5	7.4976e-4	1.2373e-3	2.5136e-4	1.2085e-3
3.5-4.0	-1.0650e-3	1.2213e-3	1.6252e-3	1.1907e-3
4.0-4.5	-1.2666e-3	1.2958e-3	4.0882e-4	1.2606e-3
4.5-5.0	-1.7381e-4	1.4595e-3	8.9449e-5	1.4184e-3
5.0-6.0	-2.3829e-4	1.3051e-3	-7.5014e-4	1.2682e-3
6.0-7.0	1.4573e-3	1.8180e-3	-2.5377e-3	1.7663e-3
7.0-8.0	4.0941e-3	2.5922e-3	-4.1343e-5	2.5204e-3
8.0-9.0	4.8433e-3	3.6578e-3	-7.4660e-3	3.5598e-3
9.0-10.	1.2529e-3	5.1036e-3	-1.5370e-3	4.9655e-3
10.-12.	-5.5673e-3	5.5495e-3	-8.0450e-4	5.3972e-3
12.-15.	4.2838e-3	8.4686e-3	6.6191e-3	8.2511e-3
15.-20.	7.2977e-3	1.6658e-2	3.0635e-4	1.6351e-2

Table 7.4: Run12 $A_L^{\pi^0}$ Result. Second and third column are for blue beam and fourth and fifth for yellow beam.

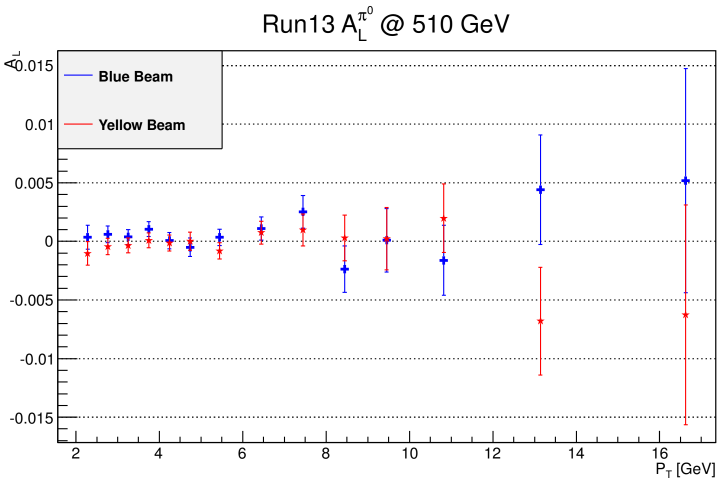

Figure 7.31: Run13 $A_L^{\pi^0}$ Result. Zero asymmetry is observed.

P_T	$A_L^{\pi^0}$(B)	$\Delta A_L^{\pi^0}$(B)	$A_L^{\pi^0}$(Y)	$\Delta A_L^{\pi^0}$(Y)
2.0-2.5	3.6234e-4	1.0134e-3	-1.0228e-3	9.9303e-4
2.5-3.0	6.0726e-4	7.2151e-4	-4.3623e-4	7.0724e-4
3.0-3.5	3.8203e-4	6.3652e-4	-3.4367e-4	6.2395e-4
3.5-4.0	1.0513e-3	6.3810e-4	9.0720e-5	6.2572e-4
4.0-4.5	6.3865e-5	6.9315e-4	-1.2807e-4	6.7966e-4
4.5-5.0	-4.9872e-4	7.8786e-4	2.3101e-5	7.7305e-4
5.0-6.0	3.4342e-4	7.0838e-4	-8.1217e-4	6.9487e-4
6.0-7.0	1.0972e-3	9.9187e-4	7.5300e-4	9.7345e-4
7.0-8.0	2.5197e-3	1.3907e-3	9.7596e-4	1.3651e-3
8.0-9.0	-2.3691e-3	1.9853e-3	2.8121e-4	1.9479e-3
9.0-10.	1.0005e-4	2.7157e-3	2.2874e-4	2.6645e-3
10.-12.	-1.6099e-3	2.9870e-3	1.9774e-3	2.9311e-3
12.-15.	4.4157e-3	4.6797e-3	-6.8046e-3	4.5953e-3
15.-20.	5.1928e-3	9.5604e-3	-6.2682e-3	9.3716e-3

Table 7.5: Run13 $A_L^{\pi^0}$ Result. Second and third column are for blue beam and fourth and fifth for yellow beam.

Chapter 8

Results and Discussions

By weighted averaging of $A_{LL}^{\pi^0}$ of in Fig. 7.17 and Fig. 7.18, the final $A_{LL}^{\pi^0}$ results are obtained. The Run12 and Run13 results are treated independently. The result is summarized in Fig. 8.1, Tab. 8.1 and Tab. 8.2..

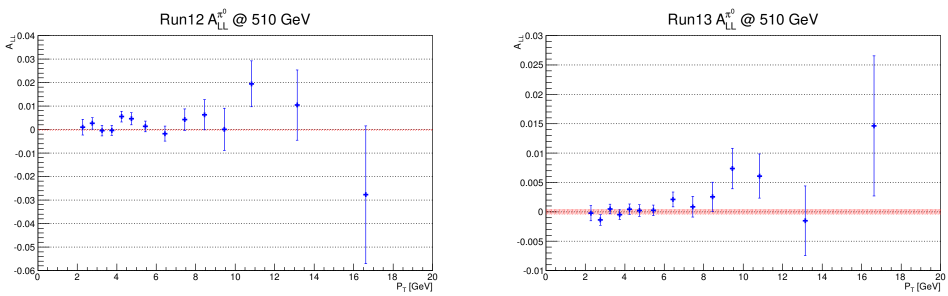

(a) Run12 (b) Run13

Figure 8.1: Final Run12 and Run13 $A_{LL}^{\pi^0}$ at $\sqrt{s} = 510$ GeV. For Run12 result, systematic uncertainty from the relative luminosity 2.003×10^{-4} is shown by red band. For Run13 result the systematic uncertainty 3.853×10^{-4} is shown by same way. See Subsubsec. 6.7.2 for detail. 6.5% global scaling uncertainty is not shown. See. Subsec. 7.2.3 for detail.

8.1 Combining Run12 and Run13 Results

As Fig. 8.2 shows, there is no statistical difference between the results of Run12 and Run13. Thus weighted averaged is enough to combined Run12 and Run13 $A_{LL}^{\pi^0}$ results. Here weights, $w = 1/(\Delta A_{LL}^{\pi^0})^2$ for each P_T bin.

To combine systematic uncertainty from relative luminosity, similar way is used. Combined systematic uncertainty is obtained by weighted average of the uncertainty of Run12 and Run13, where weights, $w = 1/(\Delta A_{LL}^{\pi^0})^2$. 3.629×10^{4} is assigned as systematic

P_T Bin	Mean P_T	$A_{LL}^{\pi^0}$	$\Delta A_{LL}^{\pi^0}$
2.0-2.5	2.2757e+0	1.0158e-3	3.3323e-3
2.5-3.0	2.7618e+0	2.6293e-3	2.4715e-3
3.0-3.5	3.2516e+0	-4.9647e-4	2.1890e-3
3.5-4.0	3.7458e+0	-3.8930e-4	2.1565e-3
4.0-4.5	4.2415e+0	5.4878e-3	2.2848e-3
4.5-5.0	4.7387e+0	4.5958e-3	2.5695e-3
5.0-6.0	5.4475e+0	1.3293e-3	2.2970e-3
6.0-7.0	6.4458e+0	-1.7668e-3	3.1998e-3
7.0-8.0	7.4445e+0	4.2114e-3	4.5589e-3
8.0-9.0	8.4470e+0	6.2972e-3	6.4352e-3
9.0-10.	9.4507e+0	6.7031e-5	8.9778e-3
10.-12.	1.0824e+1	1.9447e-2	9.7648e-3
12.-15.	1.3140e+1	1.0398e-2	1.4916e-2
15.-20.	1.6616e+1	-2.7727e-2	2.9326e-2

Table 8.1: Run12 $A_{LL}^{\pi^0}$ at $\sqrt{s} = 510$ GeV.

P_T Bin	Mean P_T	$A_{LL}^{\pi^0}$	$\Delta A_{LL}^{\pi^0}$
2.0-2.5	2.2801e+0	-2.2138e-4	1.2918e-3
2.5-3.0	2.7627e+0	-1.3901e-3	9.2251e-4
3.0-3.5	3.2507e+0	4.6369e-4	8.1329e-4
3.5-4.0	3.7440e+0	-4.8270e-4	8.1390e-4
4.0-4.5	4.2401e+0	4.4910e-4	8.8162e-4
4.5-5.0	4.7378e+0	2.2152e-4	1.0026e-3
5.0-6.0	5.4460e+0	2.5139e-4	8.9455e-4
6.0-7.0	6.4454e+0	2.0970e-3	1.2523e-3
7.0-8.0	7.4454e+0	8.5907e-4	1.7673e-3
8.0-9.0	8.4471e+0	2.5418e-3	2.4795e-3
9.0-10.	9.4512e+0	7.3621e-3	3.4539e-3
10.-12.	1.0824e+1	6.0844e-3	3.7467e-3
12.-15.	1.3140e+1	-1.5295e-3	5.9230e-3
15.-20.	1.6627e+1	1.4624e-2	1.1918e-2

Table 8.2: Run13 $A_{LL}^{\pi^0}$ at $\sqrt{s} = 510$ GeV.

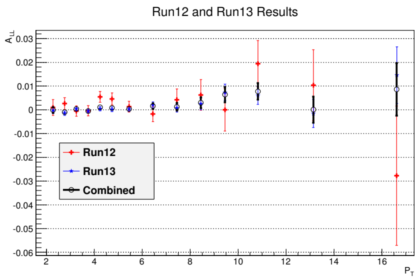

(a) Run12 and Run13 $A_{LL}^{\pi^0}$

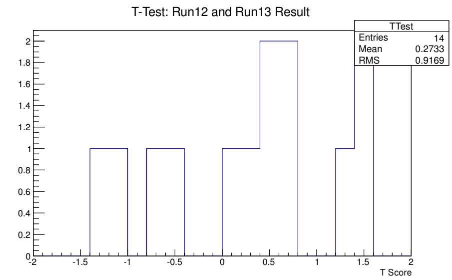

(b) T-test of Run12 and Run13

Figure 8.2: Comparison between Run12 and Run13 Result. There is no statistical difference between Run12 and Run13 $A_{LL}^{\pi^0}$ results.

uncertainty of Run12 and Run13 combined result.

The systematic uncertainty from the estimation of the background fraction is discussed in Subsec. 7.2.4.

8.2 Final Result and Comparison with Theoretical Curve

Fig. 8.3 shows the final $A_{LL}^{\pi^0}$ at $\sqrt{s} = 510$ GeV. The world first positive asymmetry in hadron production is observed. Comparing to the null hypothesis $A_{LL} = 0$, $\chi^2/NDF = 18.2/14$ is obtained. Comparison of measured $A_{LL}^{\pi^0}$ with DSSV14 theoretical curve is shown by Fig. 8.4. The DSSV14 curve excellently agrees with data. Comparing the DSSV14 curve, $\chi^2/NDF = 8.0/14$ is obtained.

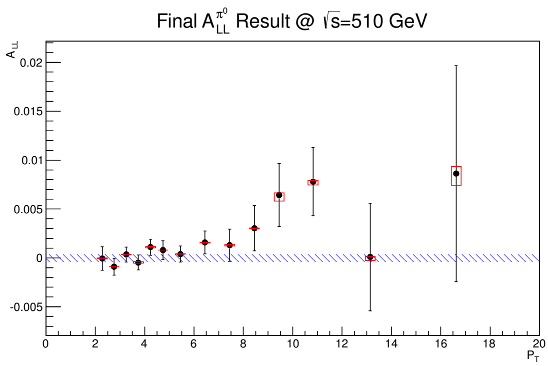

Figure 8.3: Final Result: $A_{LL}^{\pi^0}$ at $\sqrt{s} = 510$ GeV. Run12 510 GeV and Run13 510 GeV data are included. Red boxes mean systematic uncertainty from background fraction estimation. Systematic uncertainty from uncertainty of relative luminosity, 3.629×10^{-4} is shown by blue line. 6.5% global scaling uncertainty is not shown.

P_T Bin	Mean P_T	$A_{LL}^{\pi^0}$	$\Delta A_{LL}^{\pi^0}$ (stat.)	$\Delta A_{LL}^{\pi^0}$ (syst. low)	$\Delta A_{LL}^{\pi^0}$ (syst. up)
2.0-2.5	2.28e+0	-5.9734e-5	1.2045e-3	-3.1372e-5	6.4822e-5
2.5-3.0	2.76e+0	-8.9857e-4	8.6427e-4	-5.5442e-7	4.8258e-6
3.0-3.5	3.25e+0	3.4723e-4	7.6237e-4	-2.5032e-5	4.2650e-5
3.5-4.0	3.74e+0	-4.7105e-4	7.6147e-4	-6.0970e-5	8.2888e-5
4.0-4.5	4.24e+0	1.1021e-3	8.2251e-4	-7.9581e-5	6.4770e-5
4.5-5.0	4.74e+0	7.9952e-4	9.3402e-4	-1.4622e-6	5.0877e-6
5.0-6.0	5.45e+0	3.9334e-4	8.3357e-4	-5.4210e-20	1.4307e-5
6.0-7.0	6.45e+0	1.5839e-3	1.1661e-3	-5.7409e-5	2.7201e-5
7.0-8.0	7.45e+0	1.2970e-3	1.6478e-3	-9.2023e-5	5.4536e-5
8.0-9.0	8.45e+0	3.0273e-3	2.3137e-3	-4.8726e-5	2.0546e-5
9.0-10.	9.45e+0	6.4216e-3	3.2236e-3	-6.2357e-4	2.1401e-4
10.-12.	1.08e+1	7.7991e-3	3.4980e-3	-3.3141e-4	1.2121e-4
12.-15.	1.31e+1	9.5156e-5	5.5048e-3	-3.6747e-4	5.0308e-5
15.-20.	1.66e+1	8.6207e-3	1.1041e-2	-1.2064e-3	7.3194e-4

Table 8.3: Final result: $A_{LL}^{\pi^0}$ at $\sqrt{s} = 510$ GeV. Lower and upper bound of systematic uncertainty from background fraction are listed.

Comparison of the new measurement at $\sqrt{s} = 510$ GeV data with the previous measurement at $\sqrt{s} = 200$ GeV is shown by Fig. 8.5 along with NLO pQCD analyses. The new measurement covers lower $0.01 < x$ region and observes the positive asymmetry while the previous cover $0.02 < x$ region and fails to observe finite asymmetry due to statistical limit. The three NLO pQCD analyses have predicted larger asymmetry for $\sqrt{s} = 510$ GeV due to pQCD evolution. The prediction is consistent with data within large uncertainty.

8.3 Prospect: Impacts on ΔG

Although the final result is presented as $A_{LL}^{\pi^0}$ in the dissertation, the ultimate goal of this research is constraining $\Delta g(x,Q^2)$ and ΔG. To interpret the $A_{LL}^{\pi^0}$ result and to estimate the impact on ΔG, the pQCD global analyses are needed and the analyses are ongoing by theory groups. Preliminary results of DSSV and NNPDF groups are discussed below.

Fig. 8.6 is the result of DSSV group, $\Delta\chi^2$ profile for variations of $\Delta g^{[0.01-0.05]}$[1] with and without the $A_{LL}^{\pi^0}$ result. The $A_{LL}^{\pi^0}$ succeeds in making $\Delta\chi^2$ profile narrow. This implies the uncertainty of $\Delta g(x,Q^2)$ can be constrained successfully by the measurement in the target x region.

Similar global analysis is being done by NNPDF group also with different methodology. Fig 8.7 is the result of $\Delta g(x,Q^2)$ with and without the $A_{LL}^{\pi^0}$ results at both of $\sqrt{s} = 200$ and $\sqrt{s} = 510$ GeV. With the result, $\Delta g^{[0.01-0.05]}$ becomes 0.074 ± 0.16 from 0.098 ± 0.19.

[1] $\Delta g^{[0.01-0.05]} \equiv \int_{0.01}^{0.05} dx \Delta g(x,Q^2)$

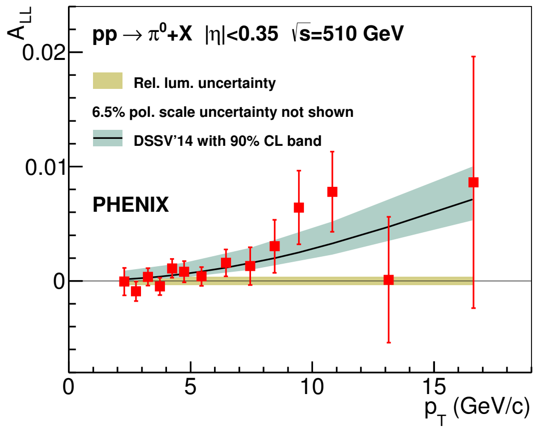

Figure 8.4: Comparison of measured $A_{LL}^{\pi^0}$ with DSSV14 theoretical curve with 90% confident level uncertainty. [12] In the plot, statistical uncertainty and systematic uncertainty from background fraction are combined.

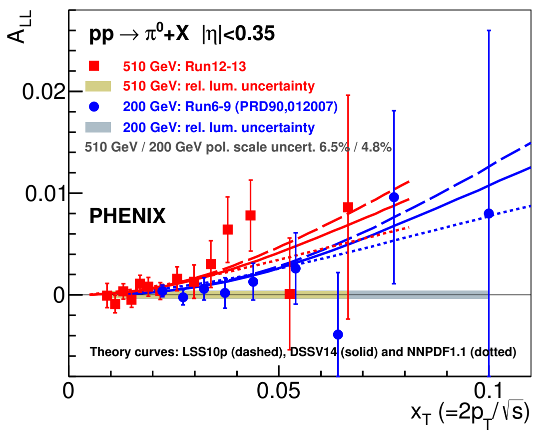

Figure 8.5: $A_{LL}^{\pi^0}$ vs. x_T at $\sqrt{s} = 510$ GeV (Red) and 200 GeV (Blue). Theoretical curves are also shown. LSS10p[48], DSSV14 [12], NNPDF1.1 [49]

We can check $A_{LL}^{\pi^0}$ results constrain $\Delta g(x, Q^2)$ and ΔG as expected.

The final and comprehensive results of global analyses will be published in soon. Then the impact of the $A_{LL}^{\pi^0}$ can be discussed in detail.

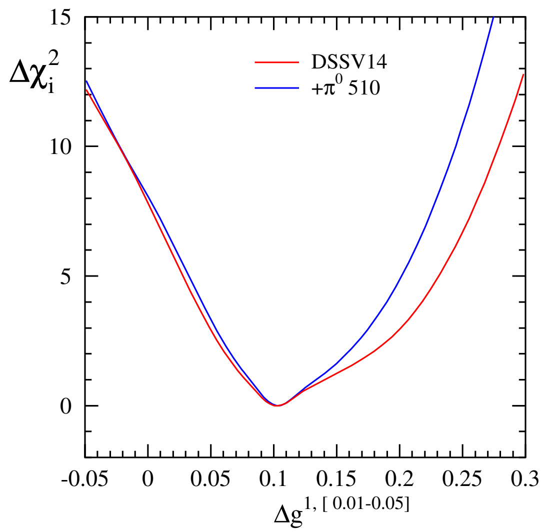

Figure 8.6: $\Delta\chi^2$ profile for variations of $\Delta g^{[0.01-0.05]}$ with and without the $A_{LL}^{\pi^0}$ result. [50]

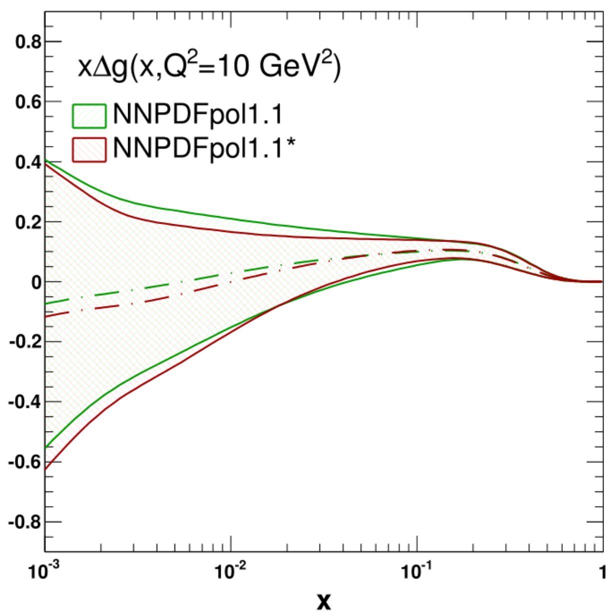

Figure 8.7: $\Delta g(x,Q^2)$ with (red curve) and without (green curve) the $A_{LL}^{\pi^0}$ results at both of $\sqrt{s}=200$ and $\sqrt{s}=510$ GeV. [51] Uncertainty band becomes narrow in the target x region, $0.01<x<0.1$ including x region of $\sqrt{s}=200$ GeV, successfully.

Appendix A

Warn Map Generation

A.1 Determining Hot Towers

Because noisy or hot towers can make combinatorial background large, the tower should be rejected in the analysis. To find hot tower, hits per tower distribution is drawn and right-side outliers are marked as “hot”. ERT “OR” trigger is required when the distribution is drawn. Fig. A.1 is example of hits per tower distribution. The distribution is fit with Gaussian function and any tower which satisfies the following condition is marked as hot.

$$\begin{aligned}\text{number of hit for the tower} > &\text{average of hit number} \\ &+ \text{hot level} \times \text{standard deviation of hit number}\end{aligned} \tag{A.1}$$

Where “hot level” is parameter for determining level of tightness. The procedure has been done for various energy bins and sectors. When we scanned energy bins, ERT turn-on region is not considered because hits per tower distribution is distorted in that region. For this analysis hot level 5 is used.

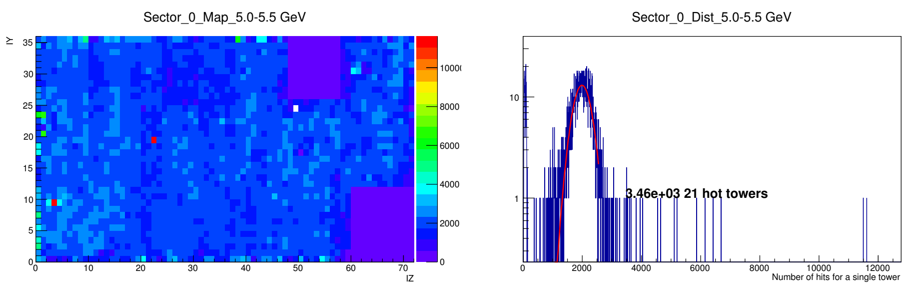

(a) Sector 0 Hit Map 5.0-5.5 GeV

(b) Sector 0 Distribution 5.0-5.5 GeV

Figure A.1: Hits per tower distribution for energy 5.0-5.5 GeV. Fitting with Gaussian function has been done to get average and variance of hit number. Note that there are not only dead towers but also intact tower which ERTs are dead in left peak.

A.2 Determining Dead Towers

Dead tower are rejected in the analysis to prevent mismeasurement of shower which spreads over the dead towers. As Fig. A.1 shows, there are towers which has exactly no hit. The towers are regarded as completely dead and rejected from the analysis.

A.3 Determining Uncalibrated Towers

Uncalibrated towers in [37] and [38] are marked as uncalibrated and rejected.

A.4 Neighbor Towers

Towers which are neighboring the hot, dead or uncalibrated tower are excluded also in order to prevent a cluster centered on a good tower but extending into a bad tower from being analyzed. Because a typical photon shower is not more than three towers in diameter, only direct neighbor towers are excluded.

Appendix B

Parallel CrossCheck

Note) The cross check is done for Run13 data only. To focus cross check itself, run-by-run energy calibration is not considered in the following results.

B.1 Cross Check Result of $A_{LL}^{\pi^0+BG}$ and A_{LL}^{BG}

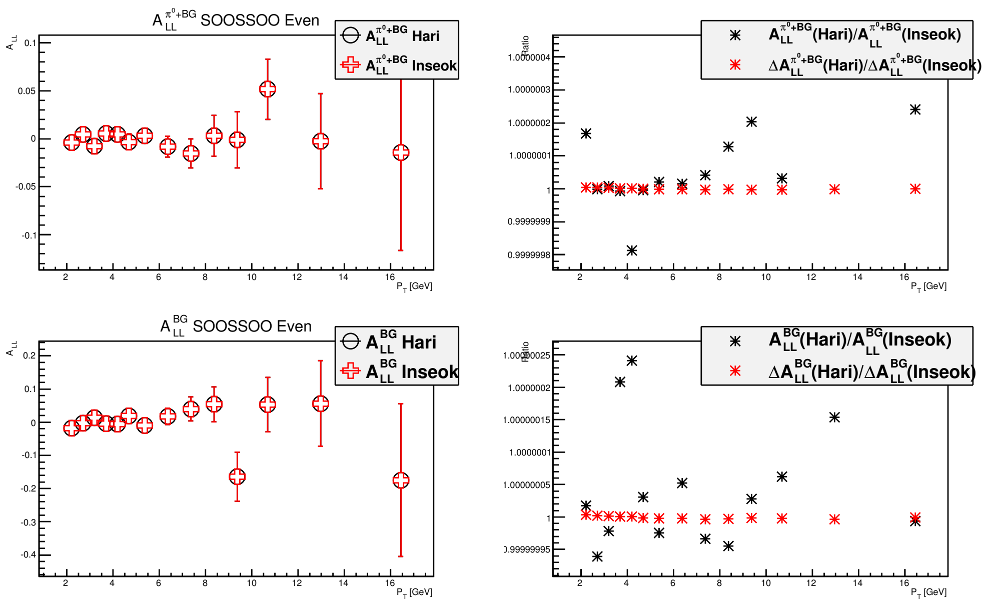

Figure B.1: Cross check result of $A_{LL}^{\pi^0+BG}$ and A_{LL}^{BG} for SOOSSOO pattern and even crossing. Perfect overlaid A_{LL} and the ratio$\sim$1 guarantee perfect match is obtained.

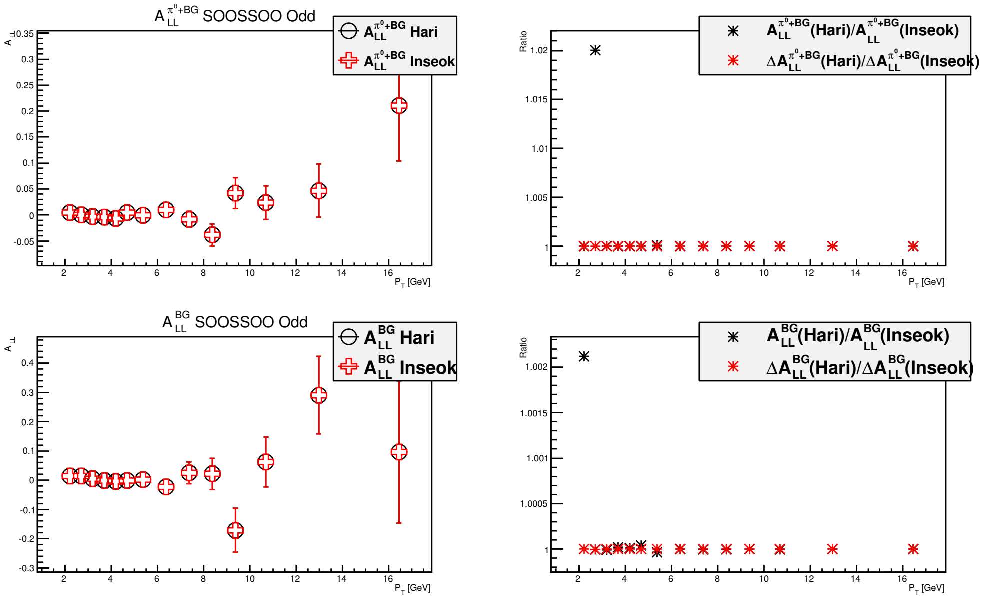

Figure B.2: Cross check result of $A_{LL}^{\pi^0+BG}$ and A_{LL}^{BG} for SOOSSOO pattern and odd crossing. Perfect overlaid A_{LL} and the ratio$\sim$1 guarantee perfect match is obtained.

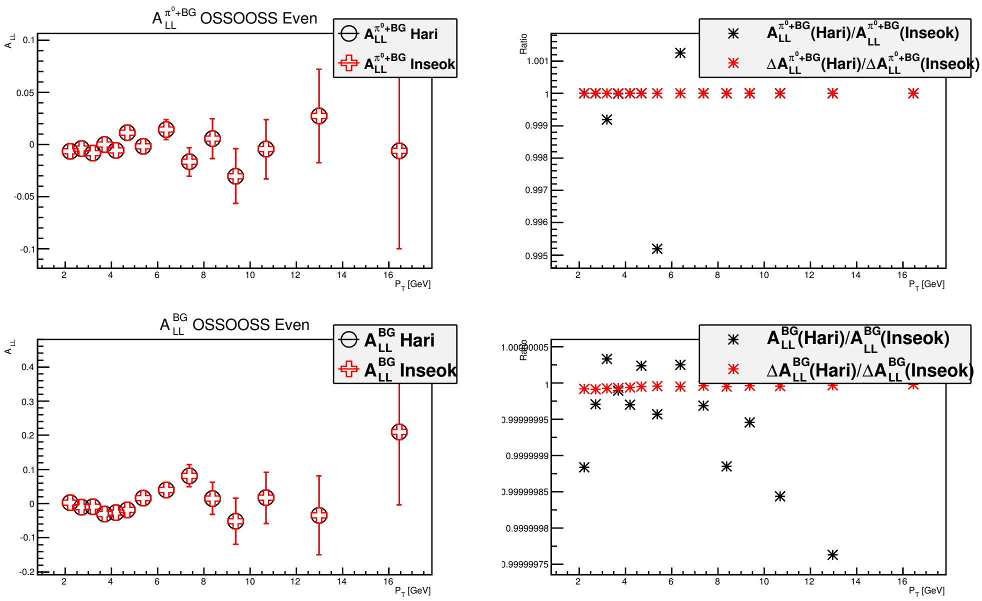

Figure B.3: Cross check result of $A_{LL}^{\pi^0+BG}$ and A_{LL}^{BG} for OSSOOSS pattern and even crossing. Perfect overlaid A_{LL} and the ratio$\sim$1 guarantee perfect match is obtained.

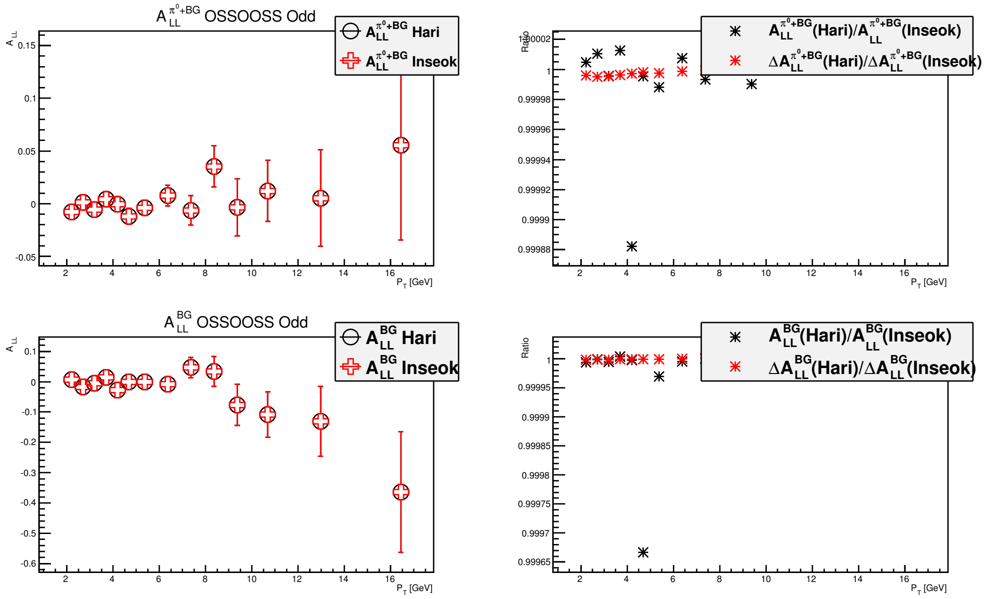

Figure B.4: Cross check result of $A_{LL}^{\pi^0+BG}$ and A_{LL}^{BG} for OSSOOSS pattern and odd crossing. Perfect overlaid A_{LL} and the ratio$\sim$1 guarantee perfect match is obtained.

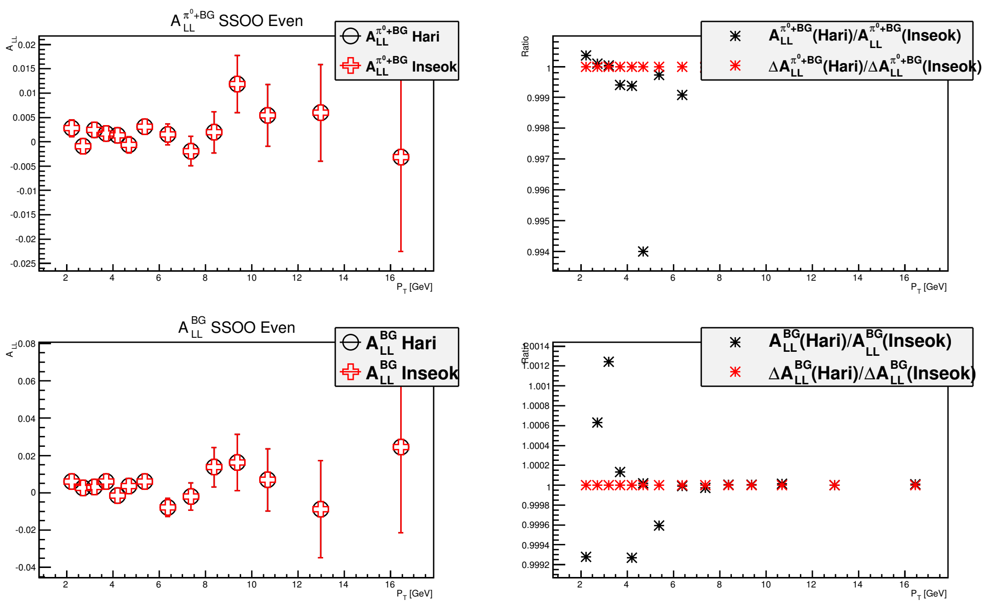

Figure B.5: Cross check result of $A_{LL}^{\pi^0+BG}$ and A_{LL}^{BG} for SSOO pattern and even crossing. Perfect overlaid A_{LL} and the ratio$\sim$1 guarantee perfect match is obtained.

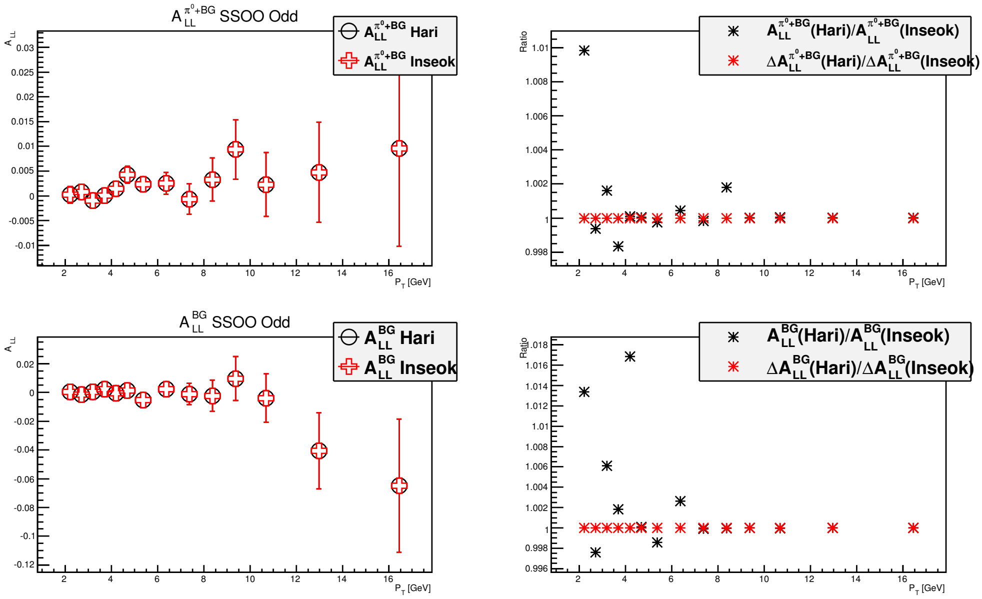

Figure B.6: Cross check result of $A_{LL}^{\pi^0+BG}$ and A_{LL}^{BG} for SSOO pattern and odd crossing. Perfect overlaid A_{LL} and the ratio$\sim$1 guarantee perfect match is obtained.

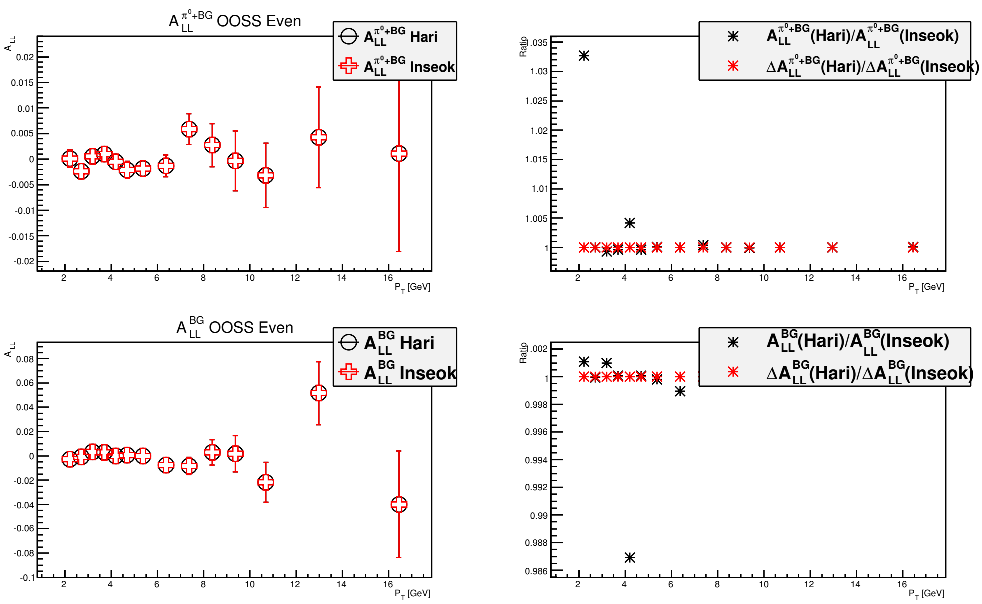

Figure B.7: Cross check result of $A_{LL}^{\pi^0+BG}$ and A_{LL}^{BG} for OOSS pattern and even crossing. Perfect overlaid A_{LL} and the ratio$\sim$1 guarantee perfect match is obtained.

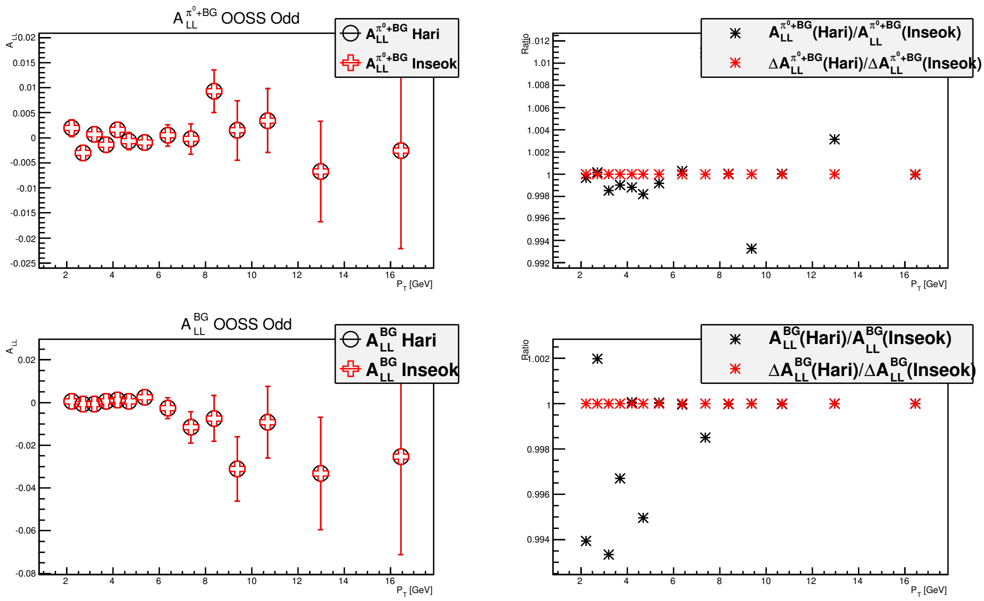

Figure B.8: Cross check result of $A_{LL}^{\pi^0+BG}$ and A_{LL}^{BG} for OOSS pattern and odd crossing. Perfect overlaid A_{LL} and the ratio$\sim$1 guarantee perfect match is obtained.

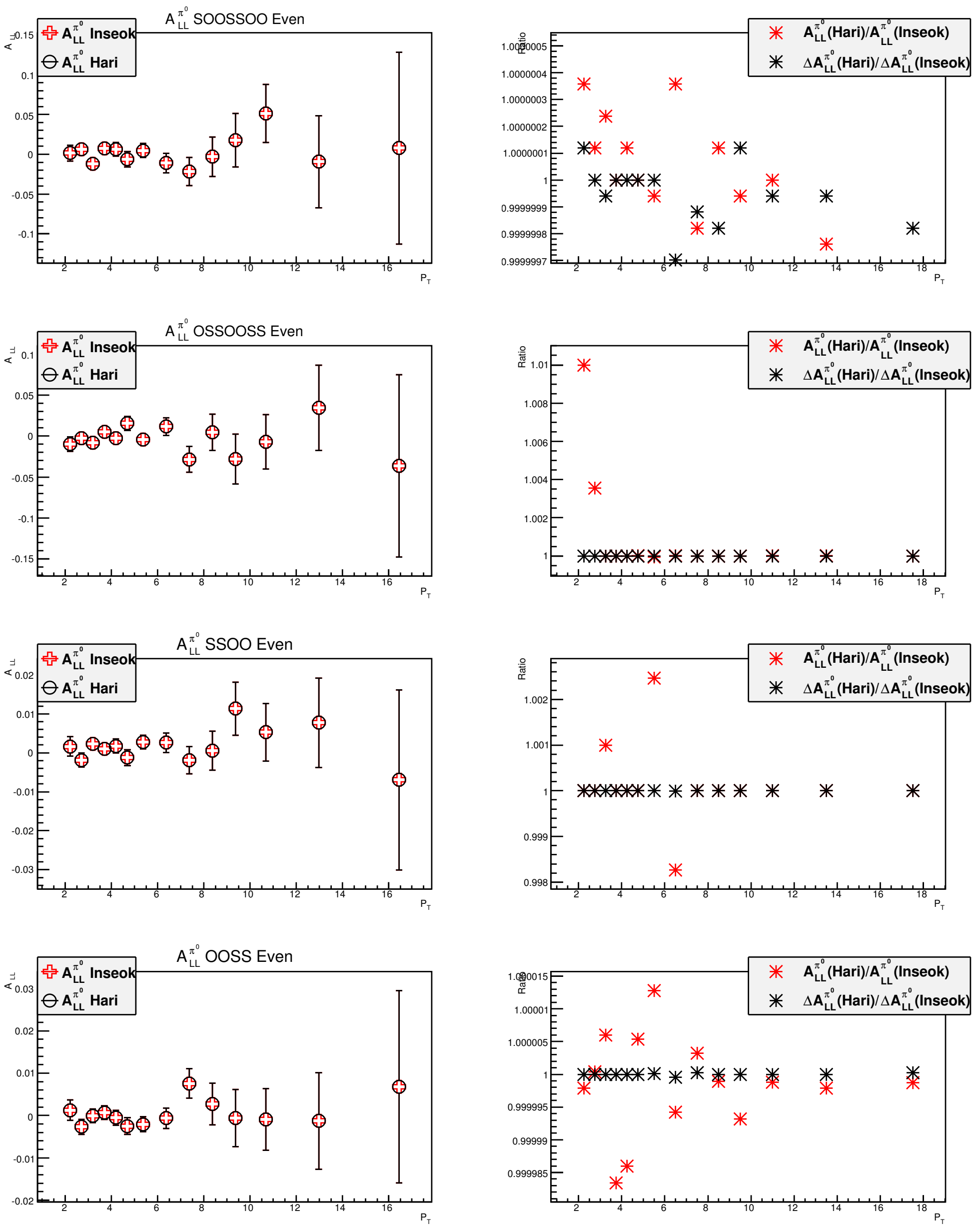

Figure B.9: Cross check result of $A_{LL}^{\pi^0}$ for even crossing. Perfect overlaid A_{LL} and the ratio∼1 guarantee perfect match is obtained.

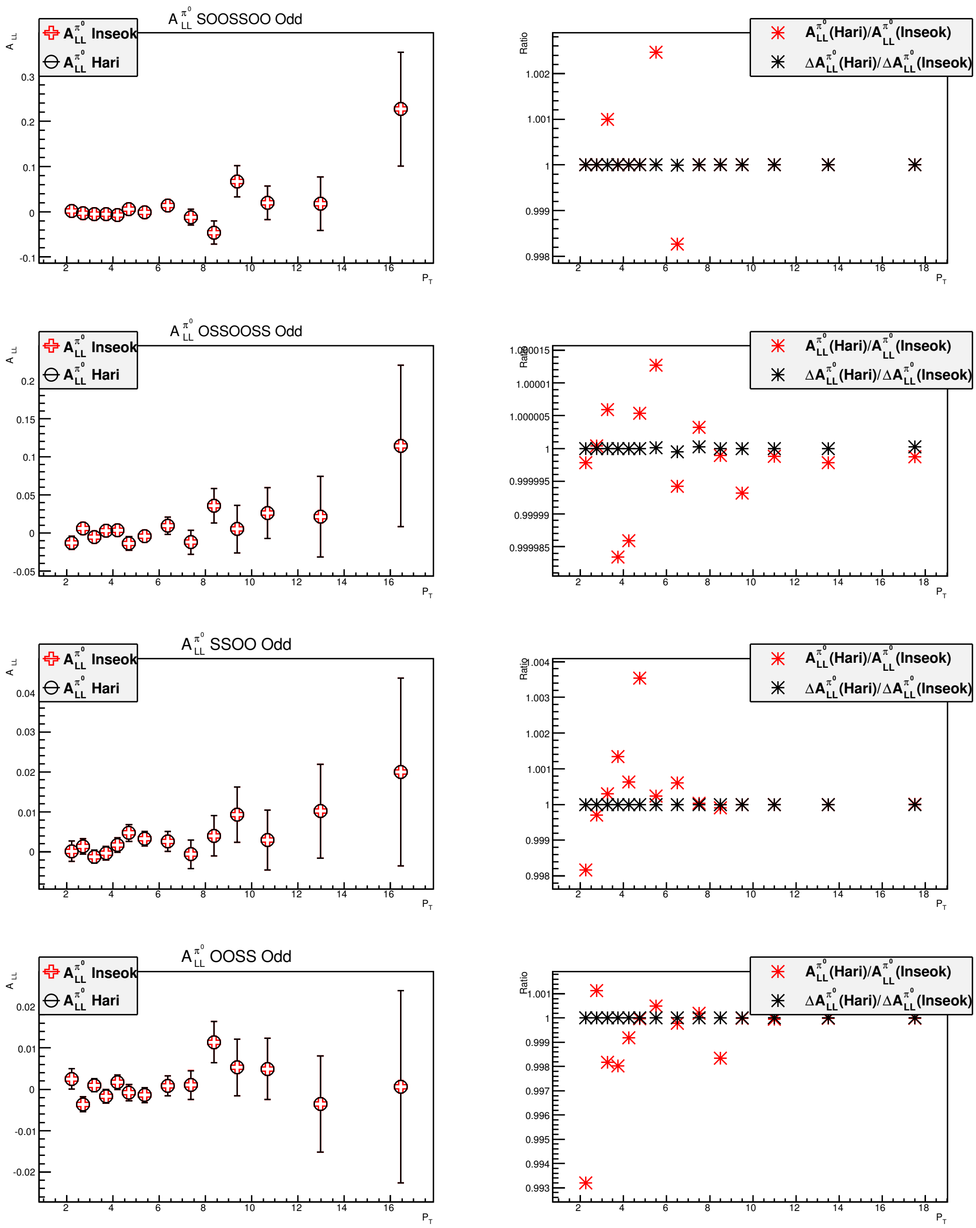

Figure B.10: Cross check result of $A_{LL}^{\pi^0}$ for odd crossing. Perfect overlaid A_{LL} and the ratio$\sim$1 guarantee perfect match is obtained.

B.2 Final Cross Check Result

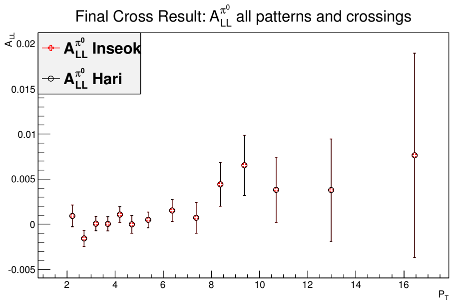

Figure B.11: Cross check result of $A_{LL}^{\pi^0}$ for all spin patterns and crossing. Perfect overlaid of A_{LL}s guarantees perfect match is obtained.

P_T	$A_{LL}^{\pi^0}(H)$	$\Delta A_{LL}^{\pi^0}(H)$	$A_{LL}^{\pi^0}(I)$	$\Delta A_{LL}^{\pi^0}(I)$	Comp.
2.0-2.5	9.293e-4	1.206e-3	9.269e-4	1.206e-3	1.943e-3
2.5-3.0	-1.565e-3	8.899e-4	-1.565e-3	8.899e-4	-3.886e-4
3.0-3.5	6.651e-5	7.920e-4	6.788e-5	7.920e-4	-1.719e-3
3.5-4.0	3.860e-5	7.945e-4	3.872e-5	7.945e-4	-1.504e-4
4.0-4.5	1.077e-3	8.619e-4	1.078e-3	8.619e-4	-1.274e-3
4.5-5.0	-2.017e-5	9.794e-4	-2.190e-5	9.794e-4	1.764e-3
5.0-6.0	4.812e-4	8.705e-4	4.815e-4	8.705e-4	-2.362e-4
6.0-7.0	1.524e-3	1.204e-3	1.524e-3	1.204e-3	-1.546e-4
7.0-8.0	7.147e-4	1.708e-3	7.152e-4	1.708e-3	-2.922e-4
8.0-9.0	4.427e-3	2.432e-3	4.425e-3	2.432e-3	6.568e-4
9.0-10	6.532e-3	3.339e-3	6.535e-3	3.339e-3	-7.712e-4
10.-12.	3.813e-3	3.613e-3	3.813e-3	3.613e-3	2.112e-5
12.-15.	3.779e-3	5.672e-3	3.785e-3	5.672e-3	-9.829e-4
15.-20.	7.641e-3	1.132e-2	7.641e-3	1.132e-2	5.637e-6

Table B.1: Cross Check Result of $A_{LL}^{\pi^0}$ for All Patterns and Crossings. “H” means the corresponding columns are Hari’s values and “I” means the corresponding columns are Inseok’s values. The sixth column for comparison is $(A_{LL}^{\pi^0}(Hari)$-$A_{LL}^{\pi^0}(Inseok))/\Delta A_{LL}^{\pi^0}(Inseok)$. Nice agreement is obtained.

Bibliography

[1] Particle Data Group, K. A. Olive *et al.*, Chin. Phys. **C38**, 090001 (2014).

[2] Martin, A. D., Stirling, W. J., Thorne, R. S., and Watt, G., Eur. Phys. J. C **64**, 653 (2009).

[3] J. Ellis and R. Jaffe, Phys. Rev. D **9**, 1444 (1974).

[4] L. M. Sehgal, Phys. Rev. D **10**, 1663 (1974).

[5] M. J. Alguard *et al.*, Phys. Rev. Lett. **37**, 1261 (1976).

[6] M. J. Alguard *et al.*, Phys. Rev. Lett. **41**, 70 (1978).

[7] G. Baum *et al.*, Phys. Rev. Lett. **51**, 1135 (1983).

[8] European Muon, J. Ashman *et al.*, Nuclear Physics B **328**, 1 (1989).

[9] R. Jaffe and A. Manohar, Nuclear Physics B **337**, 509 (1990).

[10] A. N. Khorramian, S. Atashbar Tehrani, S. Taheri Monfared, F. Arbabifar, and F. I. Olness, Phys. Rev. D **83**, 054017 (2011).

[11] D. de Florian, R. Sassot, M. Stratmann, and W. Vogelsang, Phys. Rev. D **80**, 034030 (2009).

[12] D. de Florian, R. Sassot, M. Stratmann, and W. Vogelsang, Phys. Rev. Lett. **113**, 012001 (2014).

[13] PHENIX Collaboration, A. Adare *et al.*, Phys. Rev. D **79**, 012003 (2009).

[14] PHENIX Collaboration, A. Adare *et al.*, Phys. Rev. D **90**, 012007 (2014).

[15] STAR Collaboration, L. Adamczyk *et al.*, Phys. Rev. Lett. **115**, 092002 (2015).

[16] G. Bunce, N. Saito, J. Soffer, and W. Vogelsan, Annu. Rev. Nucl. Sci. **50**, 525 (2000).

[17] E.-C. Aschenauer *et al.*, (2015), 1501.01220.

[18] D. de Florian, R. Sassot, M. Epele, R. J. Hernández-Pinto, and M. Stratmann, Phys. Rev. D **91**, 014035 (2015).

[19] I. Alekseev *et al.*, Nuclear Instruments and Methods in Physics Research Section A: Accelerators, Spectrometers, Detectors and Associated Equipment **499**, 392 (2003), The Relativistic Heavy Ion Collider Project: RHIC and its Detectors.

[20] K. Adcox *et al.*, Nuclear Instruments and Methods in Physics Research Section A: Accelerators, Spectrometers, Detectors and Associated Equipment **499**, 469 (2003), The Relativistic Heavy Ion Collider Project: RHIC and its Detectors.

[21] A. Zelenski, The RHIC polarized source upgrade, in *Proceedings, 15th International Workshop on Polarized Sources, Targets, and Polarimetry (PSTP 2013)*, p. 048, 2013.

[22] V. Bargmann, L. Michel, and V. L. Telegdi, Phys. Rev. Lett. **2**, 435 (1959).

[23] J. Tojo *et al.*, Phys. Rev. Lett. **89**, 052302 (2002).

[24] B. Z. Kopeliovich and T. L. Trueman, Phys. Rev. D **64**, 034004 (2001).

[25] H. Okada *et al.*, Physics Letters B **638**, 450 (2006).

[26] A. Anders *et al.*, RHIC Polarized Proton Operation in Run 12, in *Proceedings, 3rd International Conference on Particle accelerator (IPAC 2012)*, pp. 184–186, 2012.

[27] V. Ranjbar *et al.*, RHIC Polarized Proton Operation for 2013, in *Proceedings, 4th International Particle Accelerator Conference (IPAC 2013)*, p. TUPFI084, 2013.

[28] RHIC Spin Group, Run 12 Polarization, `https://wiki.bnl.gov/rhicspin/Run_12_polarization`, 2012.

[29] RHIC Spin Group, Run 13 Polarization, `https://wiki.bnl.gov/rhicspin/Run_13_polarization`, 2015.

[30] H. Guragain, Run-by-Run Polarization Values from Run13 510GeV Data Sets, PHENIX Analysis Note 1226, 2015.

[31] M. Allen *et al.*, Nuclear Instruments and Methods in Physics Research Section A: Accelerators, Spectrometers, Detectors and Associated Equipment **499**, 549 (2003), The Relativistic Heavy Ion Collider Project: RHIC and its Detectors.

[32] C. Adler *et al.*, Nuclear Instruments and Methods in Physics Research Section A: Accelerators, Spectrometers, Detectors and Associated Equipment **470**, 488 (2001).

[33] S. Aronson *et al.*, Nuclear Instruments and Methods in Physics Research Section A: Accelerators, Spectrometers, Detectors and Associated Equipment **499**, 480 (2003), The Relativistic Heavy Ion Collider Project: RHIC and its Detectors.

[34] K. Adcox *et al.*, Nuclear Instruments and Methods in Physics Research Section A: Accelerators, Spectrometers, Detectors and Associated Equipment **499**, 489 (2003), The Relativistic Heavy Ion Collider Project: RHIC and its Detectors.

[35] M. Aizawa *et al.*, Nuclear Instruments and Methods in Physics Research Section A: Accelerators, Spectrometers, Detectors and Associated Equipment **499**, 508 (2003), The Relativistic Heavy Ion Collider Project: RHIC and its Detectors.

[36] L. Aphecetche *et al.*, Nuclear Instruments and Methods in Physics Research Section A: Accelerators, Spectrometers, Detectors and Associated Equipment **499**, 521 (2003), The Relativistic Heavy Ion Collider Project: RHIC and its Detectors.

[37] C. Gal and J. Mitchell, Run12 510GeV EMCal calibration, `https://www.phenix.bnl.gov/cdsagenda/askArchive.php?base=agenda&categ=a12304&id=a12304s1t21/moreinfo`, 2012.

[38] J. Mitchell, Run13 EMCal calibration status, `https://www.phenix.bnl.gov/WWW/p/draft/mitchell/20130424-ANA/phxana-20130424.pdf`, 2013.

[39] PHENIX Collaboration, A. Adare *et al.*, Phys. Rev. D **88**, 032006 (2013).

[40] M. Kim, Phenix local polarimetry analysis, Master's thesis, Seoul National University, 2014.

[41] S. Frank, C. Britton, A. Wintenberg, and G. Young, Trigger circuits for the PHENIX electromagnetic calorimeter, in *Nuclear Science Symposium, 1997. IEEE*, pp. 680–684 vol.1, 1997.

[42] S. Adler *et al.*, Nuclear Instruments and Methods in Physics Research Section A: Accelerators, Spectrometers, Detectors and Associated Equipment **499**, 560 (2003), The Relativistic Heavy Ion Collider Project: RHIC and its Detectors.

[43] K. Boyle *et al.*, Run12 spin database quality assurance, PHENIX Analysis Note 1096, 2013.

[44] M. Beaumier *et al.*, Run13 spin database quality assurance, PHENIX Analysis Note 1125, 2013.

[45] A. Bazilevsky *et al.*, Results on double longitudinal spin asymmetry (A_{LL}) in π^0 production in proton-proton collisions at $\sqrt{s}$=200 GeV from Run03, PHENIX Analysis Note 277, 2004.

[46] B. Bannier *et al.*, Regression with Gaussian processes, PHENIX Analysis Note 1145, 2013.

[47] A. Manion *et al.*, Final Results on the Double Helicity Asymmetry A_{LL} in π^0 Production in $\sqrt{s} = 200$ GeV Polarized Proton-Proton Collisions during Run-9, PHENIX Analysis Note 1100, 2013.

[48] E. Leader, A. V. Sidorov, and D. B. Stamenov, Phys. Rev. D **82**, 114018 (2010).

[49] E. R. Nocera, R. D. Ball, S. Forte, G. Ridolfi, and J. Rojo, Nuclear Physics B **887**, 276 (2014).

[50] DSSV Group, R. Sassot, private communication, 2015.

[51] NNPDF Group, E. R. Nocera, private communication, 2015.

국 문 초 록

이 논문은 2012/2013 RHIC 런 $\sqrt{s} = 510$ GeV 편극 양성자 충돌에서 PHENIX 중앙 신속도 검출기를 이용한 중성 파이온 생성의 이중 스핀 비대칭성 측정(A_{LL})을 다룬다. EMC 실험에서 양성자 스핀 중 쿼크의 스핀 기여도가 적은 것이 측정된 후, 양성자의 스핀 구조를 이해하기 위한 많은 실험과 이론적인 노력이 수행되고 있다. 글루온의 스핀 기여도(ΔG)가 양성자 스핀의 부족분을 설명할 수도 있으며, ΔG을 측정하는 것이 이 논문의 궁극적인 목적이다. ΔG을 측정하기 위해, 헬리시티 글루온 분포($\Delta g(x, Q^2)$)의 측정이 필요하다. 종편극 양성자 충돌과 A_{LL} 측정은 이를 위한 최고의 도구이다. $\sqrt{s} = 62.4$ 그리고 200 GeV 충돌에서의 중성 파이온의 $A_{LL}(A_{LL}^{\pi^0})$와 200 GeV 충돌에서의 제트의 A_{LL} 측정이 $\Delta g(x, Q^2)$을 상당히 제한하였다. 그 결과로 측정된 운동량비(x) 영역, $0.05 \leq x \leq 0.2$에서 글루온의 양성 편극이 발견되었다. 그러나 이 영역 밖에서, 특히 낮은 x 영역에 많은 불확정성이 남아있다. 그러므로 실험적인 감도를 낮은 x 영역으로 확장하는 것은 ΔG와 양성자의 스핀 구조를 이해하기 위한 중대한 과정이다. 낮은 x 영역으로 접근하기 위해, 이 논문에서는 더 높은 $\sqrt{s} = 510$ GeV 충돌에서 $A_{LL}^{\pi^0}$의 새로운 측정이 수행되었다. 이 새로운 측정은 x 영역, $0.01 \leq x \leq 0.1$을 담당한다. 이 새로운 측정은 특유의 x 영역 뿐 아니라, 통계적인 정밀도의 면에서 이전 측정 결과보다 우수하다. 한 다발 교차에서 다중 충돌과, 검출기의 충돌점 해상도의 영향을 줄이기 위해, 정교한 휘도 보정 또한 이 논문에서 다룬다. 이 결과로 세계 최초의 강입자 생성의 양성 비대칭성이 측정되었다. 이전 결과를 포함하는 섭동적 양자색역학 이론 예측은 제시된 $A_{LL}^{\pi^0}$ 결과와 훌륭하게 일치한다. 양성 비대칭성과 특유의 담당 x 영역으로, 제시된 $A_{LL}^{\pi^0}$이 $\Delta g(x, Q^2)$의 불확실성을 상당히 제한하는데 공헌할 것이다.

주요어 : 양성자 스핀, 글루온, 중성 파이온의 A_{LL}, PHENIX

학번 : 2011-20412

Acknowledgement

The dissertation would not have been possible without helps of many people. I would like to thank them for their unwaving supports.

Firstly, I would like to thank my advisor, Kiyoshi Tanida, for introducing nice physics topics to me and his guidance. I've learned from him not only physics itself but also how to be a physicist.

I would also like to thank members of RIKEN radiation laboratory, Hideto En'yo, Yuji Goto, Itaru Nakagawa, and Ralf Seidl. Regular discussion with them has made this dissertation wider and fruitful. I also thank Kieko Suzuki for her numerous helps. I'm grateful to financial suport of RIKEN.

I appreciate members of PHENIX collaboration especially Kieran Bolye, Chin-Hao Chen and Alexander Bazilevsky. Kieran spent many hours to teach me the basics of the analysis. I've learned how ERT is operated from Chin-Hao. Alexander Bazilevsky alway answered my questions about not only experiment and analysis but also physics itself.

마지막으로 가족들에게 고맙다는 말씀을 드리고 싶습니다. 항상 저를 먼저 생각하는 부모님과 형의 부재 동안 많은 부담을 진 동생에게 고마움을 전합니다. 그리고 긴 학위 과정 동안 언제나처럼 제 옆을 지켜준 아내에게 사랑을 전합니다.